

## RESEARCH RESOURCE

### Sustaining wakefulness: Brainstem connectivity in human consciousness

Brian L. Edlow,<sup>1,2,\*</sup> Mark Olchanyi,<sup>1</sup> Holly J. Freeman,<sup>1,2</sup> Jian Li,<sup>1,2</sup> Chiara Maffei,<sup>1,2</sup> Samuel B. Snider,<sup>3</sup> Lilla Zöllei,<sup>2</sup> J. Eugenio Iglesias,<sup>2</sup> Jean Augustinack,<sup>2</sup> Yelena G. Bodien,<sup>1,4</sup> Robin L. Haynes,<sup>5</sup> Douglas N. Greve,<sup>2</sup> Bram R. Diamond,<sup>1,2</sup> Allison Stevens,<sup>2</sup> Joseph T. Giacino,<sup>4</sup> Christophe Destrieux,<sup>6,7</sup> Andre van der Kouwe,<sup>2</sup> Emery N. Brown,<sup>8,9</sup> Rebecca D. Folkerth,<sup>10</sup> Bruce Fischl,<sup>2,11</sup> Hannah C. Kinney<sup>5</sup>

<sup>1</sup> Center for Neurotechnology and Neurorecovery, Department of Neurology, Massachusetts General Hospital and Harvard Medical School, Boston, MA 02114, USA

<sup>2</sup> Athinoula A. Martinos Center for Biomedical Imaging, Department of Radiology, Massachusetts General Hospital and Harvard Medical School, Charlestown MA 02129, USA

<sup>3</sup> Department of Neurology, Brigham and Women's Hospital and Harvard Medical School, Boston, MA 02115, USA

<sup>4</sup> Department of Physical Medicine and Rehabilitation, Spaulding Rehabilitation Hospital and Harvard Medical School, Charlestown, MA 02129 USA

<sup>5</sup> Department of Pathology, Boston Children's Hospital and Harvard Medical School, Boston, MA 02115, USA

<sup>6</sup> UMR 1253, iBrain, Université de Tours, Inserm, 10 Boulevard Tonnellé, 37032, Tours, France.

<sup>7</sup> CHRU de Tours, 2 Boulevard Tonnellé, Tours, France.

<sup>8</sup> Department of Anesthesia, Critical Care, and Pain Medicine, Massachusetts General Hospital and Harvard Medical School, Boston, MA, USA

<sup>9</sup> Department of Brain and Cognitive Sciences, Massachusetts Institute of Technology, Cambridge, MA, USA

<sup>10</sup> Office of the Chief Medical Examiner, New York, New York, NY 10016 USA

<sup>11</sup> Computer Science and Artificial Intelligence Laboratory, Massachusetts Institute of Technology, Cambridge, MA, USA

\* Corresponding Author. email: [bedlow@mgh.harvard.edu](mailto:bedlow@mgh.harvard.edu)

## ABSTRACT

Consciousness is comprised of arousal (i.e., wakefulness) and awareness. Substantial progress has been made in mapping the cortical networks that modulate awareness in the human brain, but knowledge about the subcortical networks that sustain arousal is lacking. We integrated data from *ex vivo* diffusion MRI, immunohistochemistry, and *in vivo* 7 Tesla functional MRI to map the connectivity of a subcortical arousal network that we postulate sustains wakefulness in the resting, conscious human brain, analogous to the cortical default mode network (DMN) that is believed to sustain self-awareness. We identified nodes of the proposed default ascending arousal network (dAAN) in the brainstem, hypothalamus, thalamus, and basal forebrain by correlating *ex vivo* diffusion MRI with immunohistochemistry in three human brain specimens from neurologically normal individuals scanned at 600-750  $\mu\text{m}$  resolution. We performed deterministic and probabilistic tractography analyses of the diffusion MRI data to map dAAN intra-network connections and dAAN-DMN internetwork connections. Using a newly developed network-based autopsy of the human brain that integrates *ex vivo* MRI and histopathology, we identified projection, association, and commissural pathways linking dAAN nodes with one another and with cortical DMN nodes, providing a structural architecture for the integration of arousal and awareness in human consciousness. We release the *ex vivo* diffusion MRI data, corresponding immunohistochemistry data, network-based autopsy methods, and a new brainstem dAAN atlas to support efforts to map the connectivity of human consciousness.

**One sentence summary:** We performed *ex vivo* diffusion MRI, immunohistochemistry, and *in vivo* 7 Tesla functional MRI to map brainstem connections that sustain wakefulness in human consciousness.

## INTRODUCTION

To treat disorders of human consciousness, such as coma, vegetative state, and minimally conscious state, it is essential to understand the neuroanatomic determinants and interconnectivity of arousal and awareness, two foundational components of consciousness (1).

The goal of this multimodal brain mapping study is to advance knowledge of the connectivity of human consciousness by crystalizing the concept of a subcortical default arousal network that sustains wakefulness in the resting, conscious human brain, analogous to the cortical default mode network (DMN) that is believed to sustain self-awareness (2). We additionally provide a conceptual framework, imaging methods, and atlas-based reference tools that can be used to elucidate subcortical contributions to human consciousness.

Arousal refers to physiologic activation of the brain to a state of wakefulness (3), whereas awareness refers to the content of consciousness (4). These two components of consciousness – arousal and awareness – can be dissociated, as observed in patients in the vegetative state (5), who demonstrate alternating cycles of wakefulness but absent awareness (5). Such clinical observations, bolstered by experimental data in animals (6-8), support the concept that the anatomic pathways of awareness and arousal are anatomically dissociated from one another in the brain.

Current concepts of consciousness propose that the cerebral cortex is the primary anatomic site of the neural correlates of awareness (4), whereas ascending subcortical pathways from the brainstem, hypothalamus, thalamus, and basal forebrain are the neural correlates of arousal (9, 10). Over the past two decades, there has been substantial progress in mapping the cortical brain networks that mediate human awareness (4, 11, 12). In contrast, connectivity maps of subcortical networks that mediate human arousal are far less complete. This gap in knowledge

is partly attributable to inadequate spatial resolution of standard neuroimaging techniques, which cannot discriminate individual arousal nuclei within the brainstem or delineate complex trajectories of axonal connections that link the brainstem to the diencephalon, basal forebrain, and cerebral cortex. In the absence of adequate imaging techniques for detecting brainstem arousal nuclei and their axonal connections, subcortical arousal network mapping has stalled while cortical awareness network mapping has accelerated.

The few human studies of brainstem arousal nuclei generally support Moruzzi and Magoun's seminal observations in cats regarding the key role of the brainstem reticular formation in activating the cerebral cortex (13). Positron emission tomography (PET) studies have identified an increase in metabolic activity within the brainstem reticular formation when humans wake from sleep (14). Similarly, PET studies have revealed altered metabolism within the reticular formation in patients with disorders of consciousness caused by severe brain injuries (15).

Beyond the reticular formation, animal and human studies have revealed that extrareticular nuclei in the brainstem (6, 16-19), as well as nuclei in the hypothalamus (7, 20, 21), thalamus (22, 23), and basal forebrain (6, 24, 25), also contribute to arousal (6, 26, 27). Collectively, these observations suggest that the human ascending arousal network (AAN) is a synchronized, multi-transmitter brain network comprised of reticular and extrareticular nuclei that generate activated states of alertness in response to multiple external stimuli, including noxious, tactile, vestibular, olfactory, auditory, thermal, and homeostatic stimuli (e.g., hypoxia and hypercarbia). Our goal here is to identify the anatomic substrate of the AAN that modulates the *default state* of resting wakefulness, which we refer to as the default ascending arousal network (dAAN).

Default modes of brain activity involve neuronal ensembles that create distinct oscillatory modes of firing patterns during different brain states (28). In the awake state, the brain toggles between a default mode of wakefulness (i.e., resting wakefulness) and a non-default mode of wakefulness (i.e., active attention or task performance) (2, 29). In this conceptual framework, a default network is one whose nodes demonstrate temporally correlated activity during a default mode of brain activity (30). Maintenance of the resting wakeful state requires input from the dAAN. This view of a default state of arousal is consistent with that expressed by Steriade and Buzsaki, who wrote that “operationally, arousal may be defined as a stand-by mode of the neurons for efficient processing and transformation of afferent information” (31). In the “stand-by mode” of resting wakefulness, the human brain is not performing an externally or internally directed (i.e., introspective) task. Instead, the mind wanders and stimulus-independent thoughts may emerge (32). Behaviorally, the eyes may be open or closed. Electrophysiologically, subcortical arousal neurons fire tonically (33) and the cerebral cortex generates desynchronized, high frequency, low voltage waves on EEG (3). The dAAN thus sustains cortical activation to enable awareness, without requiring sensory input or externally directed cognition.

To advance knowledge about the connectivity of this subcortical default brain network critical to human consciousness, we performed a multimodal brain imaging study, integrating data from *ex vivo* diffusion MRI tractography and *in vivo* 7 Tesla functional MRI. We used histology and immunohistochemistry guidance to identify the anatomic location of dAAN nodes on *ex vivo* MRI scans of three human brain specimens, then mapped the structural connections of the dAAN using diffusion MRI tractography at submillimeter spatial resolution. We then performed resting-state functional MRI (rs-fMRI) analyses of 7 Tesla imaging data from the Human Connectome Project (34) to investigate the functional correlates of these structural

connections. The complementary structural-functional connectivity analyses aimed to identify the neuroanatomic basis for the integration of arousal and awareness in the resting, conscious human brain. We release all network-based autopsy methods and data, and we propose a neuroanatomic taxonomy for projection, association, and commissural pathways of the human dAAN to guide future investigations into the connectivity of human consciousness and its disorders.

## RESULTS

### Candidate dAAN nodes

Based on evidence from previously published electrophysiological, gene expression, lesion, and stimulation studies, we identified 18 candidate dAAN nodes: 10 brainstem, 3 thalamus, 3 hypothalamus, and 2 basal forebrain (**Table 1**). All 18 candidate nodes were located at the level of, or rostral to, the mid-pons. For the 13 nodes with available electrophysiological data (all except periaqueductal grey [PAG], pontis oralis [PnO], parabrachial complex [PBC], paraventricular nucleus [PaV], and supramammillary nucleus [SuM]), the electrophysiological evidence indicated active tonic firing of neurons during wakefulness and state-dependent changes in neuronal firing during wakefulness as compared to slow-wave sleep (**Table 1**).

**Table 1. Candidate default ascending arousal network (dAAN) nodes.**

Candidate dAAN node	Supporting Literature		
	Study author, year	Animal model	Type of Evidence
<b>Brainstem</b>			
<b>Midbrain reticular formation (mRt)</b>	Steriade, 1982 (35)	cat	electrophysiology
<b>Ventral tegmental area (VTA)</b>	Eban-Rothschild, 2016 (19)	mouse	electrophysiology
<b>Periaqueductal grey (PAG)</b>	Lu, 2006 (36)	rat	gene expression
<b>Pedunculotegmental nucleus (PTg)</b>	Steriade, 1990 (33)	cat	electrophysiology
<b>Dorsal raphe (DR)</b>	McGinty, 1976 (37) Trulson, 1979 (27)	cat	electrophysiology
<b>Pontis oralis (PnO)</b>	Xi, 2004 (38)	cat	Agonist/antagonist injection
<b>Parabrachial complex (PBC)</b>	Fuller, 2011 (6) Qiu 2016 (39)	rat	Lesion (Fuller) Stimulation (Qiu)
<b>Median raphe (MnR)</b>	Trulson, 1984 (40)	cat	electrophysiology
<b>Locus coeruleus (LC)</b>	Hobson, 1975 (26) Aston-Jones, 1981 (41)	rat (Aston-Jones), cat (Hobson)	electrophysiology
<b>Laterodorsal tegmental nucleus (LDTg)</b>	Steriade, 1990 (33)	cat	electrophysiology
<b>Hypothalamus</b>			
<b>Tuberomammillary nucleus (TMN)</b>	Takahashi, 2006 (42)	mouse	electrophysiology
<b>Lateral hypothalamic area (LHA)</b>	Alam, 2002 (43)	rat	electrophysiology
<b>Supramammillary nucleus (SUM)</b>	Pedersen, 2017 (7)	mouse	chemogenetics
<b>Thalamus</b>			
<b>Intralaminar nuclei (IL)</b>	Glenn, 1982 (22)	cat	electrophysiology
<b>Reticular nucleus (Ret)</b>	Steriade, 1986 (44)	cat	electrophysiology
<b>Paraventricular nucleus (PaV)</b>	Novak, 1998 (45)	rat	gene expression
<b>Basal Forebrain</b>			
<b>Nucleus basalis of Meynert/substantia innominata (BNM/SI)</b>	Szymusiak, 1986 (46)	cat	electrophysiology
<b>Diagonal band of Broca (DBB)</b>	Szymusiak, 1986 (46)	cat	electrophysiology

We identified 18 nodes that met the *a priori* criteria for inclusion in the human dAAN. The criteria were based on previous animal studies demonstrating nodal involvement in arousal from electrophysiological recording, Fos expression, lesioning, or stimulation. Given that decades of experiments in multiple animal species have tested the functional properties of subcortical arousal nuclei, we do not intend for the references in this table to be exhaustive. Rather, we list studies that are representative of the body of literature pertaining to each subcortical arousal nucleus.



## **dAAN structural connectivity**

### *Human brain specimens*

Once the 18 candidate dAAN nodes were identified, we investigated their structural connectivity using *ex vivo* diffusion MRI tractography in three human brain specimens from neurologically normal individuals. The three brain specimens were from women who died at ages 53, 60, and 61 years (**Fig. S1-S3**). Demographic and clinical data, including cause of death, are provided in **Table S1**. At autopsy, all three brain specimens had a normal fresh brain weight. Time from death until fixation in 10% formaldehyde ranged from 24 hours to 72 hours, a time window that is associated with preservation of directional water diffusion within formaldehyde-fixed brain tissue (47).

For specimen 1, candidate dAAN nodes were traced on the diffusion-weighted images using guidance from serial histologic sections (hematoxylin and eosin counterstained with Luxol fast blue) and selected immunohistochemistry sections (tyrosine hydroxylase for dopaminergic neurons and tryptophan hydroxylase for serotonergic neurons). Each set of diffusion images (diffusion-weighted images [DWI], apparent diffusion coefficient [ADC] map, fractional anisotropy [FA] map, color FA map, and non-diffusion weighted images [ $b=0$ ]) was compared to its corresponding stained sections to ensure that radiologic dAAN nodes shared the same location and morphology as the dAAN nuclei identified by histology and immunohistochemistry (**Figs. 1, S4, S5**). For specimens 2 and 3, the brainstem dAAN nuclei were traced manually on each diffusion MRI dataset with reference to selected histologic and immunohistochemistry sections and canonical atlases (48, 49). All histology and immunostaining data are available at <https://histopath.nmr.mgh.harvard.edu>.

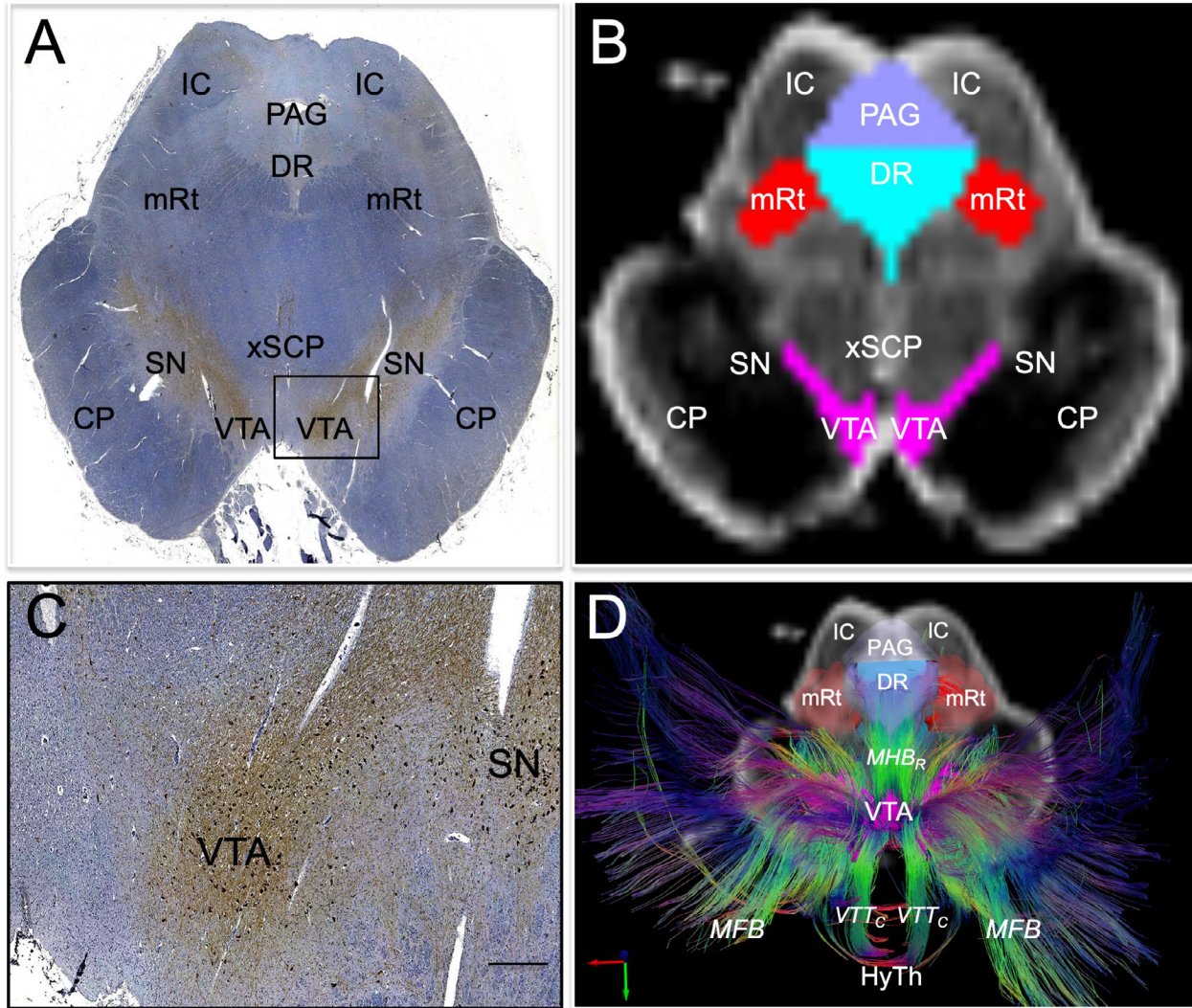


**Fig. 1. Histological guidance of node localization and tract construction.** (A) A transverse section through the caudal midbrain of specimen 1 is shown, stained with tyrosine hydroxylase and counterstained with hematoxylin. The tyrosine hydroxylase stain identifies dopaminergic neurons of the ventral tegmental area (VTA). A zoomed view of VTA neurons located within the rectangle in (A) are shown in (C; scale bar = 100  $\mu$ m). The corresponding non-diffusion-weighted ( $b=0$ ) axial image from the same specimen is shown in (B). VTA neurons are manually traced in pink, based upon the tyrosine hydroxylase staining results, and additional arousal nuclei are traced based on the hematoxylin and eosin/Luxol fast blue stain results: DR = dorsal raphe; mRt = mesencephalic reticular formation; PAG = periaqueductal grey. Deterministic fiber tracts emanating from the VTA node are shown in (D) from the same superior view as panel (B). The tracts are color-coded by direction (inset, bottom left) and the DR and mRt nodes are semi-transparent so that VTA tracts can be seen passing through them via the mesencephalic homeostatic bundle, rostral division (MHB<sub>R</sub>). VTA tracts also connect with the hypothalamus (HyTh), thalamus, basal forebrain, and cerebral cortex via multiple bundles: MFB = medial forebrain bundle; VTT<sub>C</sub> = ventral tegmental tract, caudal division. Additional abbreviations: CP = cerebral peduncle; IC = inferior colliculus; SN = substantia nigra; xSCP = decussation of the superior cerebellar peduncles.

To facilitate reproduction of our methods, we detail the neuroanatomic boundaries of all candidate dAAN nodes in **Tables S2-S6**. In addition, we provide a comprehensive summary of our anatomic approach in the **Supplementary Methods**, including a discussion of how the neuroanatomic borders of our candidate dAAN nodes relate to those defined in canonical atlases (50-52) and how they differ from those of the nodes distributed in version 1.0 of the Harvard Ascending Arousal Network Atlas (9). Based on the updated neuroanatomic nomenclature and nodal anatomic characteristics reported here, we release version 2.0 of the Harvard Ascending Arousal Network Atlas (**Video S1**) as a tool for the academic community (doi:10.5061/dryad.zw3r228d2; download link:

<https://datadryad.org/stash/share/aJ713eXY12ND56bzOBejVG2jmOFCD2CKxdSJsYWEHkw>).

Specimen 1 was scanned at 600  $\mu\text{m}$  resolution as a dissected specimen, consisting of the rostral pons, midbrain, hypothalamus, thalamus, basal forebrain, and part of the basal ganglia (9). Specimens 2 and 3 were scanned at 750  $\mu\text{m}$  resolution as whole brains. Diffusion data from all three specimens were processed for deterministic fiber tracking for qualitative assessment of tract trajectories, and diffusion data from specimens 2 and 3 were processed for probabilistic fiber tracking for quantitative assessment of connectivity. Probabilistic data for Specimen 1 were not analyzed because differences in scanning parameters and specimen composition – (i.e., dissected versus whole brain) precluded quantitative comparison. We performed deterministic tractography to assess qualitative anatomic relationships of dAAN tracts, and probabilistic tractography to measure quantitative dAAN connectivity properties.

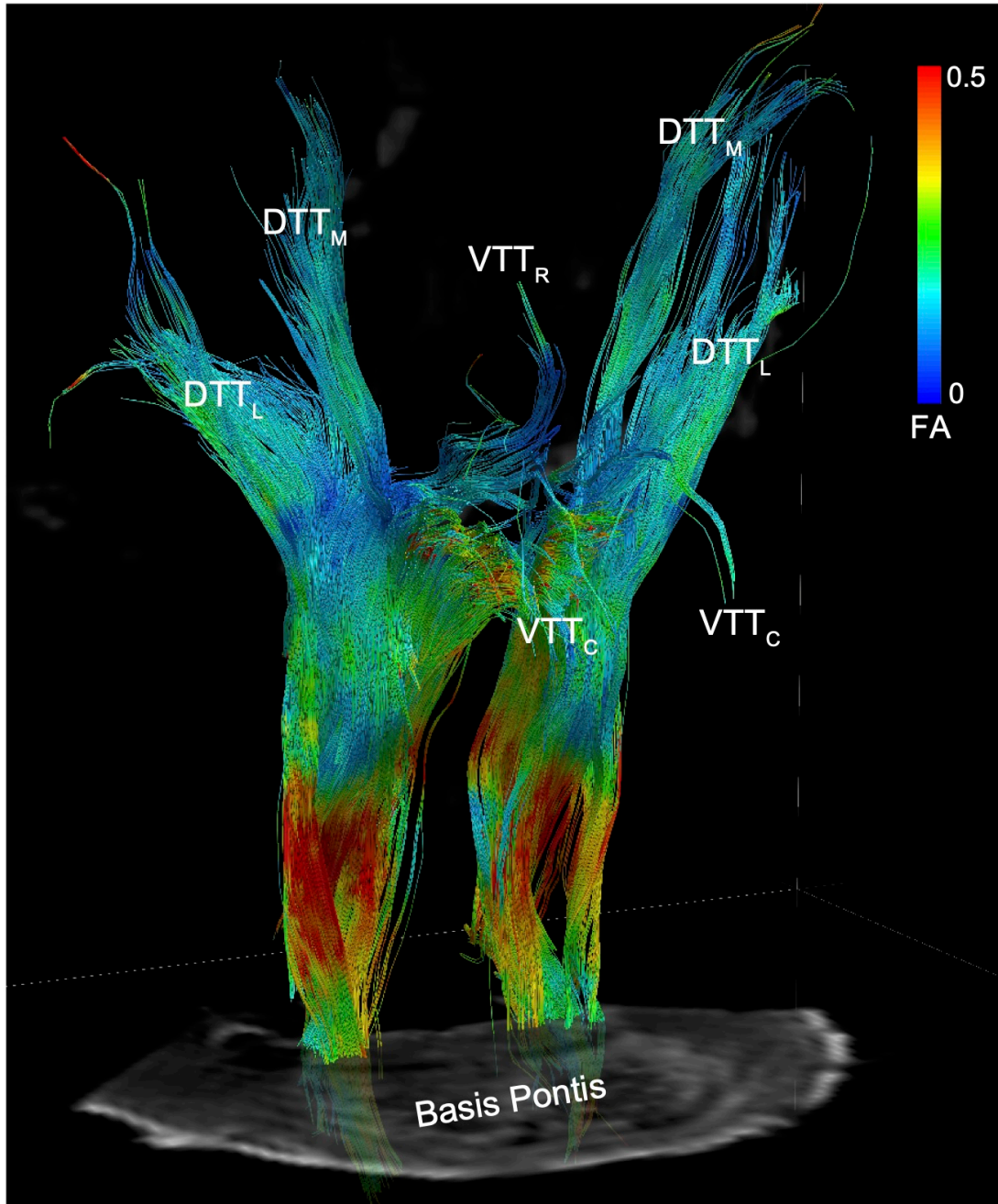


**Fig. 2. Reticular pathways of the human default ascending arousal network.** Deterministic tractography results from a seed region in the mesencephalic reticular formation (mRt), the brainstem region stimulated by Moruzzi and Magoun in their seminal investigations of the reticular activating system (13), are shown from a right ventro-lateral perspective in Specimen 1. Tracts are color-coded by the fractional anisotropy (FA) along each segment (inset color bar). Tracts are superimposed upon a non-diffusion-weighted ( $b=0$ ) axial image at the level of the mid-pons. The fiber tracts emanating from mRt travel in the ponto-mesencephalic tegmentum and connect with the thalamus, hypothalamus, and basal forebrain via the following bundles: DTT<sub>L</sub> = dorsal tegmental tract, lateral division; DTT<sub>M</sub> = dorsal tegmental tract, medial division; VTT<sub>C</sub> = ventral tegmental tract, caudal division; VTT<sub>R</sub> = ventral tegmental tract, rostral division.

### *Criteria for structural connectivity and anatomic classification of dAAN pathways*

Structural connectivity was defined using a two-step process that incorporated the quantitative probabilistic data and qualitative deterministic data. First, we performed a quantitative assessment for the presence of a connection linking each node-node pair using the probabilistic data for specimens 2 and 3 (see statistical analysis section of the Materials and Methods). A significant quantitative connection requires a connectivity probability measure that exceeds the 95% confidence interval of connectivity with two control regions that are unlikely to have connectivity with dAAN nodes based on prior animal labeling studies (e.g., (53)): basis pontis and red nucleus. If this *a priori* criterion was met in the probabilistic analysis, we then qualitatively assessed the deterministic tractography data for all three specimens for visual confirmation of tracts connecting each pair of candidate nodes. Node-node pairs that met both the probabilistic and deterministic criteria were considered to have inferential evidence for a structural connection, while node-node pairs that met one, but not both, criteria were considered to have uncertain connectivity.

We then classified the structural connectivity between all candidate node-node pairs based on the anatomic trajectories and nomenclature of subcortical bundles previously defined in humans and animals (9, 54): DTT<sub>L</sub> = dorsal tegmental tract, lateral division; DTT<sub>M</sub> = dorsal tegmental tract, medial division; LFB = lateral forebrain bundle; MFB = medial forebrain bundle; VTT<sub>C</sub> = ventral tegmental tract, caudal division; VTT<sub>R</sub> = ventral tegmental tract, rostral division (**Fig. 2**). Next, we classified all dAAN pathways as projection, association, or commissural, providing a neuroanatomic taxonomy for the subcortical dAAN, akin to that of cortical networks whose connections are classified in these terms (55). Using the brainstem as the frame of reference for classifying dAAN pathways, we defined projection fibers as those that

project from brainstem nuclei to rostral diencephalic nuclei, basal forebrain nuclei, and/or cortical regions that mediate consciousness (i.e., DMN nodes). Association fibers connect brainstem nuclei to ipsilateral brainstem nuclei, and commissural fibers cross the midline to connect with contralateral brainstem nuclei.

### *Projection pathways of the dAAN*

Deterministic tractography analysis of the three specimens revealed that tracts emanating from all dAAN candidate brainstem nuclei formed well-defined projection pathways that coursed through the rostral brainstem, diencephalon, and forebrain. Each pathway contained intermingled tracts from reticular nuclei (i.e., pontine and mesencephalic reticular formations) and extrareticular nuclei (e.g., monoaminergic, cholinergic, and glutamatergic nuclei), though the distributions of reticular and extrareticular tracts within each pathway differed (**Fig. 3**).

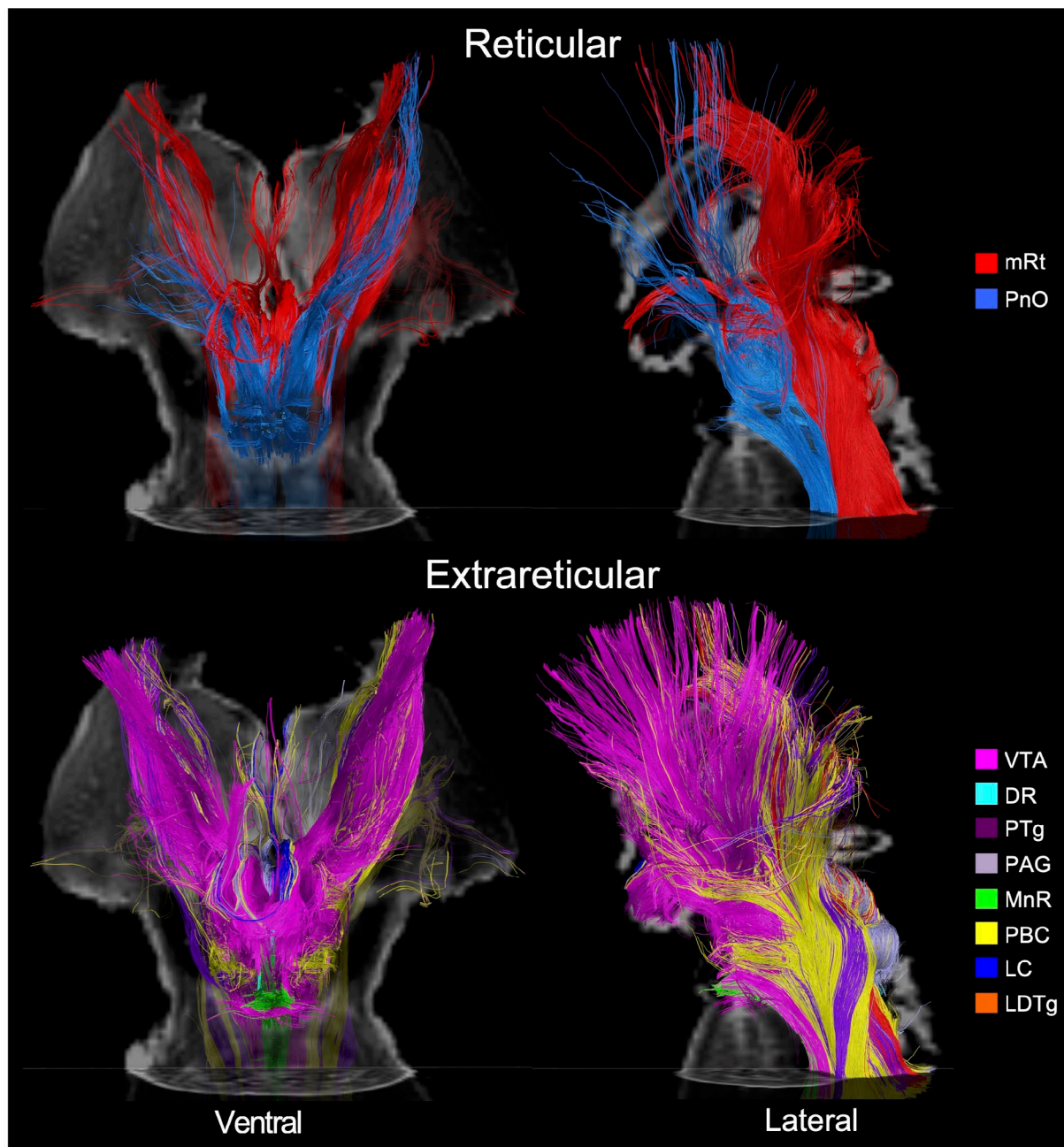


**Fig. 3. Reticular and extrareticular tracts of the default ascending arousal network.**

Deterministic fiber tracts emanating from the reticular arousal nuclei are shown in the top panels. Fiber tracts emanating from extrareticular arousal nuclei are shown in the bottom panels. All tracts are from specimen 1 and superimposed on an axial non-diffusion-weighted ( $b=0$ ) image at the level of the mid-pons. Additionally, the tracts in the ventral perspective (left column) are superimposed on a coronal  $b=0$  image at the level of the mid-thalamus, and the tracts in the left lateral perspective (right column) are superimposed on a sagittal  $b=0$  image located at the midline. All tracts are color-coded according to their nucleus of origin (inset, right). Abbreviations are described in Table 1.

All candidate brainstem nodes connected with at least one candidate hypothalamic, thalamic, or basal forebrain node based on confidence interval testing (**Table 2**). Quantitative connectivity data are provided in **Tables S7-S10** for all projection pathways. The projection pathways that connected candidate brainstem dAAN nodes with thalamic, hypothalamic, and basal forebrain dAAN nodes are shown in **Fig. 3**. The projection pathways connecting candidate brainstem dAAN nodes with cortical DMN nodes are shown in **Fig. 4**. A projection fiber connectogram with averaged CP values for specimens 2 and 3 is shown in **Fig. 5**.

Brainstem Node	Thalamus			Hypothalamus			Basal Forebrain		Default Mode Network				
	IL	Ret*	PaV	TMN	LHA	SUM	BNM/SI	DBB	PMC	MPFC	IPL	LT	MT
mRt	DTT <sub>M</sub>	DTT <sub>L</sub> DTT <sub>M</sub>	VTT <sub>R</sub>	VTT <sub>C</sub>	VTT <sub>C</sub>	VTT <sub>C</sub>	VTT <sub>C</sub>	VTT <sub>C</sub>	LFB	MFB	LFB	UC	LFB
VTA	DTT <sub>M</sub>	UC	VTT <sub>R</sub>	VTT <sub>C</sub>	VTT <sub>C</sub>	VTT <sub>C</sub>	VTT <sub>C</sub>	UC	LFB	MFB	LFB	LFB	LFB
PAG	DTT <sub>M</sub>	DTT <sub>L</sub> DTT <sub>M</sub>	VTT <sub>R</sub>	---	VTT <sub>C</sub>	VTT <sub>C</sub>	VTT <sub>C</sub>	VTT <sub>C</sub>	LFB	UC	LFB	LFB	LFB
PTg	DTT <sub>M</sub>	DTT <sub>L</sub> DTT <sub>M</sub>	VTT <sub>R</sub>	VTT <sub>C</sub>	VTT <sub>C</sub>	VTT <sub>C</sub>	VTT <sub>C</sub>	VTT <sub>C</sub>	LFB	MFB	UC	LFB	LFB
DR	DTT <sub>M</sub>	DTT <sub>L</sub>	VTT <sub>R</sub>	VTT <sub>C</sub>	VTT <sub>C</sub>	VTT <sub>C</sub>	VTT <sub>C</sub>	VTT <sub>C</sub>	LFB	UC	UC	UC	LFB
PnO	DTT <sub>M</sub>	DTT <sub>L</sub> DTT <sub>M</sub>	---	---	VTT <sub>C</sub>	---	VTT <sub>C</sub>	---	LFB	MFB	UC	UC	---
PBC	DTT <sub>M</sub>	DTT <sub>L</sub> DTT <sub>M</sub>	UC	VTT <sub>C</sub>	VTT <sub>C</sub>	---	VTT <sub>C</sub>	UC	LFB	MFB	LFB	UC	UC
MnR	---	---	---	---	VTT <sub>C</sub>	---	VTT <sub>C</sub>	---	LFB	MFB	LFB	UC	---
LC	UC	UC	UC	VTT <sub>C</sub>	VTT <sub>C</sub>	VTT <sub>C</sub>	VTT <sub>C</sub>	UC	LFB	UC	UC	UC	UC
LDTg	UC	UC	---	VTT <sub>C</sub>	VTT <sub>C</sub>	VTT <sub>C</sub>	UC	VTT <sub>C</sub>	UC	UC	UC	UC	UC

**Table 2. Projection pathways connecting brainstem dAAN nodes with thalamic, hypothalamic, and basal forebrain dAAN nodes, as well as cortical DMN nodes.** For connections that met both the probabilistic and deterministic criteria for a structural connection, we assessed the deterministic fiber tracts linking each pair of nodes for their anatomic trajectories and classified them using previously defined nomenclature (9, 54): DTT<sub>L</sub> = dorsal tegmental tract, lateral division; DTT<sub>M</sub> = dorsal tegmental tract, medial division; LFB = lateral



forebrain bundle; MFB = medial forebrain bundle; VTT<sub>C</sub> = ventral tegmental tract, caudal division; VTT<sub>R</sub> = ventral tegmental tract, rostral division. If two nodes did not meet the criteria for a connection using the probabilistic or determinist criteria, the label “---” is given, to indicate the absence of a connection. If two nodes met criteria for a connection in the probabilistic or deterministic analyses, but not both analyses, then the label “UC” (uncertain) is given. \* The DTT<sub>L</sub> pathway connects directly with Ret, whereas the DTT<sub>M</sub> pathway connects with Ret after passing through IL.

The qualitative trajectories of projection pathways connecting these nodes, as assessed by deterministic tractography, were consistent in all three specimens. All midbrain candidate nodes connected with IL via DTT<sub>M</sub> and with PaV via VTT<sub>R</sub>. All midbrain nodes except VTA (which showed uncertain connectivity) connected with Ret via DTT<sub>L</sub>. Connectivity between pontine candidate nodes and the thalamic candidate nodes was more limited, with only PnO and PBC connecting with IL and Ret, and with MnR, LC, and LDTg showing either absent or uncertain connectivity with thalamic nodes (see Discussion for potential explanations of the latter finding).

Structural connectivity with all three candidate hypothalamic nodes (TMN, LHA, and SUM) via VTT<sub>C</sub> was observed for mRt, VTA, PTg, DR, LC, and LDTg, whereas other brainstem nuclei connected with one (PnO, MnR) or two (PAG, PBC) candidate hypothalamic nodes. All midbrain and pontine candidate nodes connected with the LHA node of the hypothalamus via VTT<sub>C</sub>. Structural connectivity with the NBM/SI node of the basal forebrain was observed for all midbrain and pontine candidate nodes except LDTg via VTT<sub>C</sub>. All brainstem nodes except VTA, PnO, PBC, MnR, and LC connected with the DBB node of the basal forebrain via VTT<sub>C</sub>.

All cortical DMN nodes showed structural connectivity with at least 3 of the 10 candidate brainstem dAAN nodes. The PMC (i.e., posterior cingulate and precuneus) was the DMN node with the most extensive connections to brainstem dAAN nodes (all except LDTg), via the LFB.

The MPFC node of the DMN was connected with all brainstem dAAN nodes except PAG, DR, LC and LDTg, via the MFB. The IPL node of the DMN connected with mRt, VTA, PAG, PBC, and MnR via LFB. The MT node of the DMN was connected with all midbrain nodes via a temporal branch of the LFB, and the LT node of the DMN was connected with all midbrain nodes except mRt. There were no connections between LT or MT and the pontine candidate dAAN nodes. We observed a large contribution of extrareticular connections, dominated by VTA tracts, to the MPFC via the MFB (**Fig. 4**). Brainstem connections with IPL and PMC traveled in a parietal branch of the LFB, with similar connectivity contributions from VTA, PAG and mRt (**Fig. 4**).

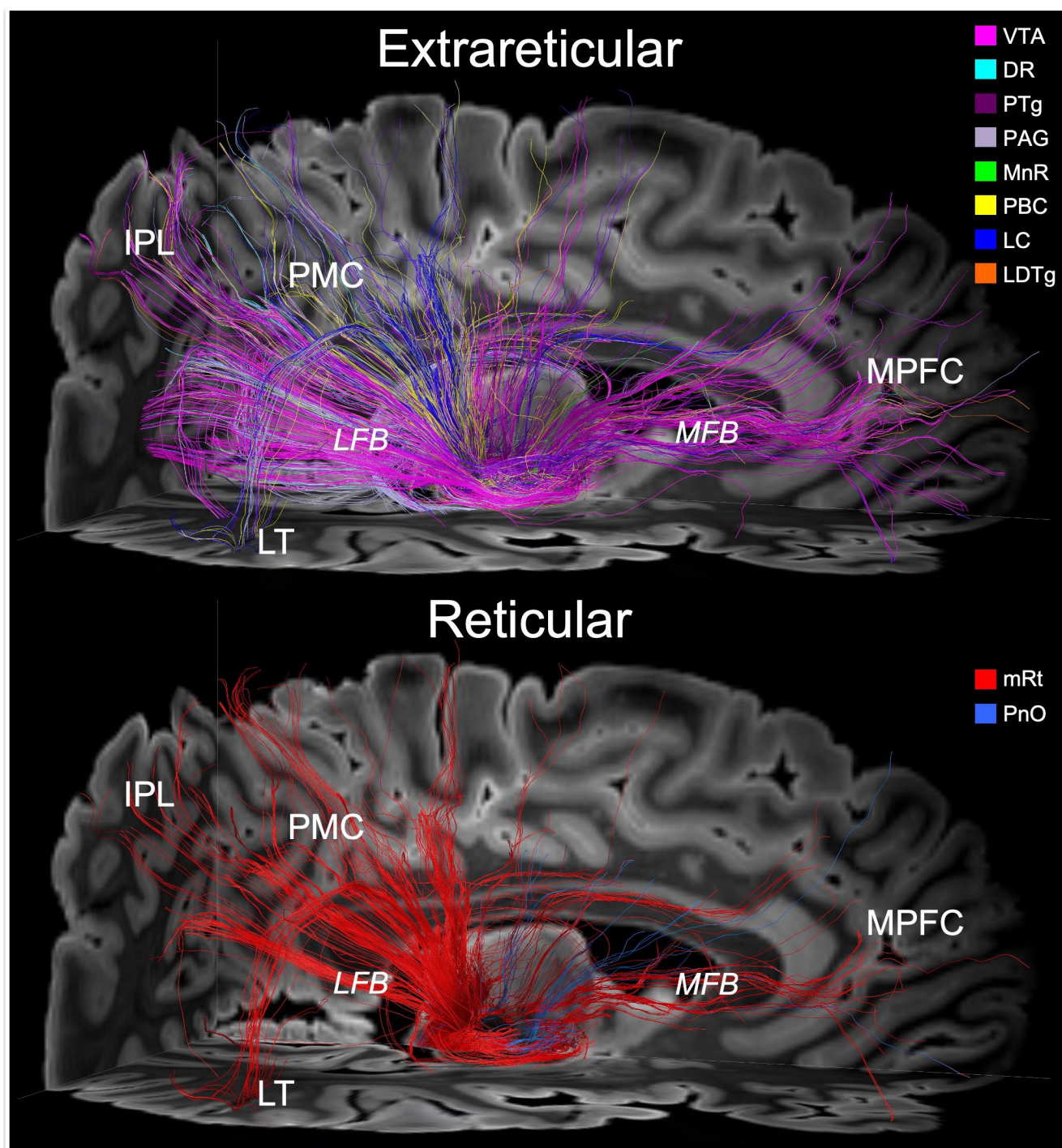


**Fig. 4. Connections linking brainstem nodes of the default ascending arousal network with cortical nodes of the default mode network.** Deterministic fiber tracts emanating from the extrareticular and reticular arousal nuclei are shown in the top and bottom panels, respectively. All tracts are shown from a right lateral perspective and superimposed upon an axial non-diffusion-weighted ( $b=0$ ) image at the level of the rostral midbrain and a sagittal  $b=0$  image to the right of the midline. Tract colors and abbreviations are the same as in Fig. 3. Both the

extrareticular and reticular brainstem arousal nuclei connect extensively with cortical nodes of the default mode network, including the medial prefrontal cortex (MPFC), posteromedial complex (PMC; i.e., posterior cingulate and precuneus), inferior parietal lobule (IPL), and lateral temporal lobe (LT). The primary pathway that connects the brainstem arousal nuclei to MPFC is the medial forebrain bundle (MFB). The primary pathway that connects the brainstem arousal nuclei to the PMC, IPL and LT is the lateral forebrain bundle (LFB).

#### *Association pathways of the dAAN*

Deterministic and probabilistic tractography analyses revealed connections linking all candidate brainstem nodes with at least one ipsilateral or midline brainstem node (**Fig. 5**). As with the projection fiber pathways, the association fiber pathways were similar between specimens. Extensive connectivity between midline, left-sided, and right-sided brainstem candidate dAAN nodes (both reticular and extrareticular) was observed (**Fig. 6** and **Video S2**). Quantitative connectivity data from the probabilistic tractography analyses of association pathways are provided in **Tables S11, S12, and S13**.

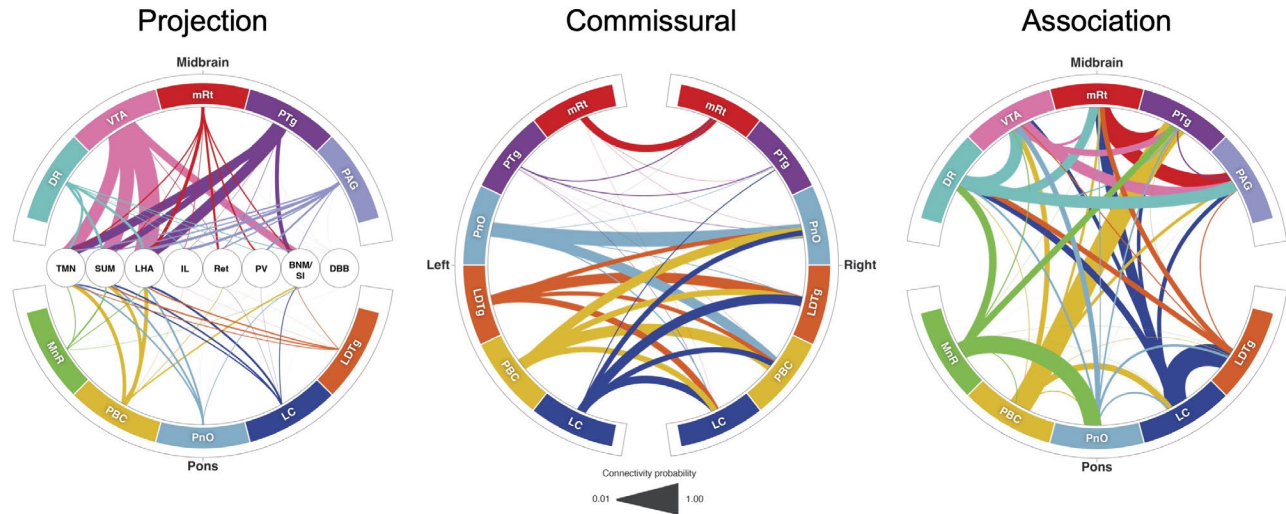


**Fig. 5. Default ascending arousal network connectograms.** Projection pathways (left) connect brainstem nodes to hypothalamic, thalamic, and basal forebrain nodes. Commissural pathways (middle) connect contralateral brainstem nodes. Association pathways (right) connect ipsilateral and/or midline brainstem nodes. Brainstem dAAN nodes are shown in the outer ring of all connectograms. In the projection connectogram, the hypothalamic, thalamic and basal forebrain nodes are shown in the center: TMN = tuberomammillary nucleus; LHA = lateral hypothalamic area; IL = intralaminar nuclei; Ret = reticular nuclei; PaV = paraventricular nuclei; BNM/SI = nucleus basalis of Meynert/substantia innominata; DBB = diagonal band of Broca. Line thicknesses in each connectogram is proportional to the connectivity probability (CP) value derived from probabilistic tractography analysis. For clarity of visualization, interspecimen mean in CP measurements is shown in the connectograms. In the commissural connectogram, we show the connections from left-to-right and omit the right-to-left connections for ease of visualization. In the association connectogram, we take a mean of left- and right-sided connectivity for bilaterally represented nodes. We do not show a connectogram for projection pathways to the DMN nodes because the connectivity probability values are lower than for diencephalic and forebrain projection pathways (Table S10), such that connections would not be visualizable at this scale.

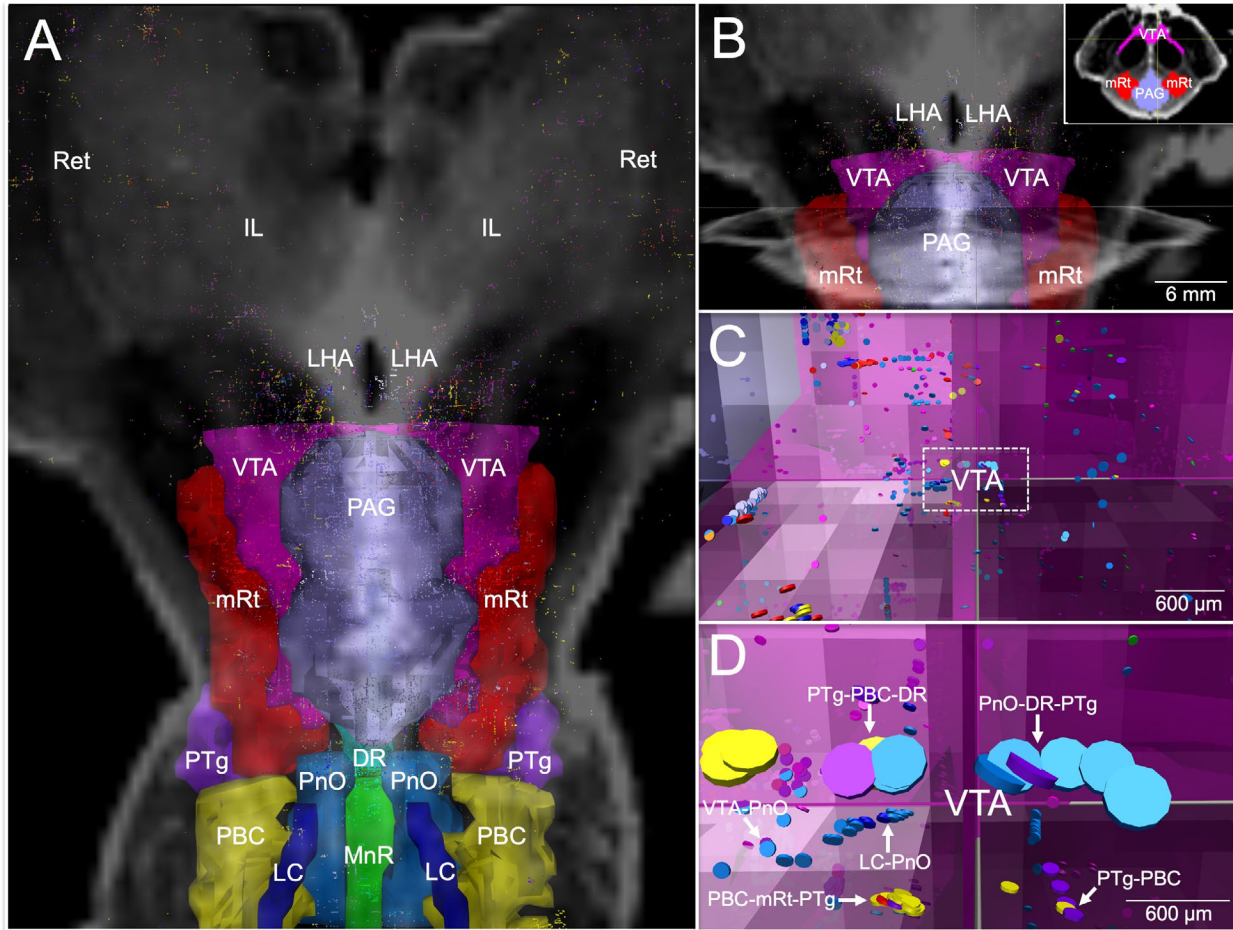


**Fig. 6. Connections linking association pathways of the default arousal network.** All candidate brainstem dAAN nodes and their tract end-points are shown from a dorsal perspective in (A), superimposed upon a coronal non-diffusion-weighted ( $b=0$ ) image at the level of the mid-thalamus. Tract end-points represent the start-points and termination-points of each tract (i.e., there are two end-points per tract). All tract end-points are color-coded by the node from which they originate, and the nodes are rendered semi-transparent so that end-points can be seen within them. In (A), tract end-points are seen within each brainstem candidate node, as well as in the lateral hypothalamic area (LHA), intralaminar nuclei of the thalamus (IL), and reticular nuclei of the thalamus (Ret). A zoomed-in view of the tract end-points within the ventral tegmental area (VTA), periaqueductal grey (PAG), and mesencephalic reticular formation (mRt) is shown in (B), superimposed upon the same coronal  $b=0$  image as in (A), as well as an axial  $b=0$  image at the intercollicular level of the midbrain. Low-zoom and high-zoom views of tract end-points (appearing as discs) within VTA are shown in (C) and (D), respectively; the axes shown in (B, C, and D) are identical and are located at the dorsomedial border of the VTA node, as shown in the Panel B inset. In (C and D), the perspective is now ventral to the PAG, just at the dorsomedial border of the VTA, as indicated by the axes. Tract end-points from multiple candidate brainstem dAAN nodes are seen overlapping within the VTA and along its dorsal border (arrows): pedunculotegmental, parabrachial complex, and dorsal raphe (PTg-PBC-DR); pontis oralis, DR, and PTg (PnO-DR-PTg); VTA-PnO; PBC-mRt-PTg; locus coeruleus and PnO (LC-PnO); and PTg-PBC. Tract end-point overlap implies that that the beginning and/or

endpoints of two tracts are in very close proximity, suggesting extensive connectivity via association pathways between ipsilateral and midline dAAN nodes with the VTA.

### *Commissural pathways of the dAAN*

We observed fewer connections in the commissural analyses as compared to the projection or association analyses. Whereas projection and association tracts were distributed in multiple discrete pathways (e.g., DTT<sub>M</sub>, DTT<sub>L</sub>, VTT<sub>R</sub>, VTT<sub>C</sub>), the commissural tracts were mostly seen within a single pathway traveling across the posterior commissure in the midbrain (**Fig. 7**). Additional commissural tracts outside the posterior commissure, particularly those in the pons, did not coalesce into discrete bundles of tracts. Quantitative connectivity data from the probabilistic tractography analyses of commissural pathways are provided in **Table S14**.

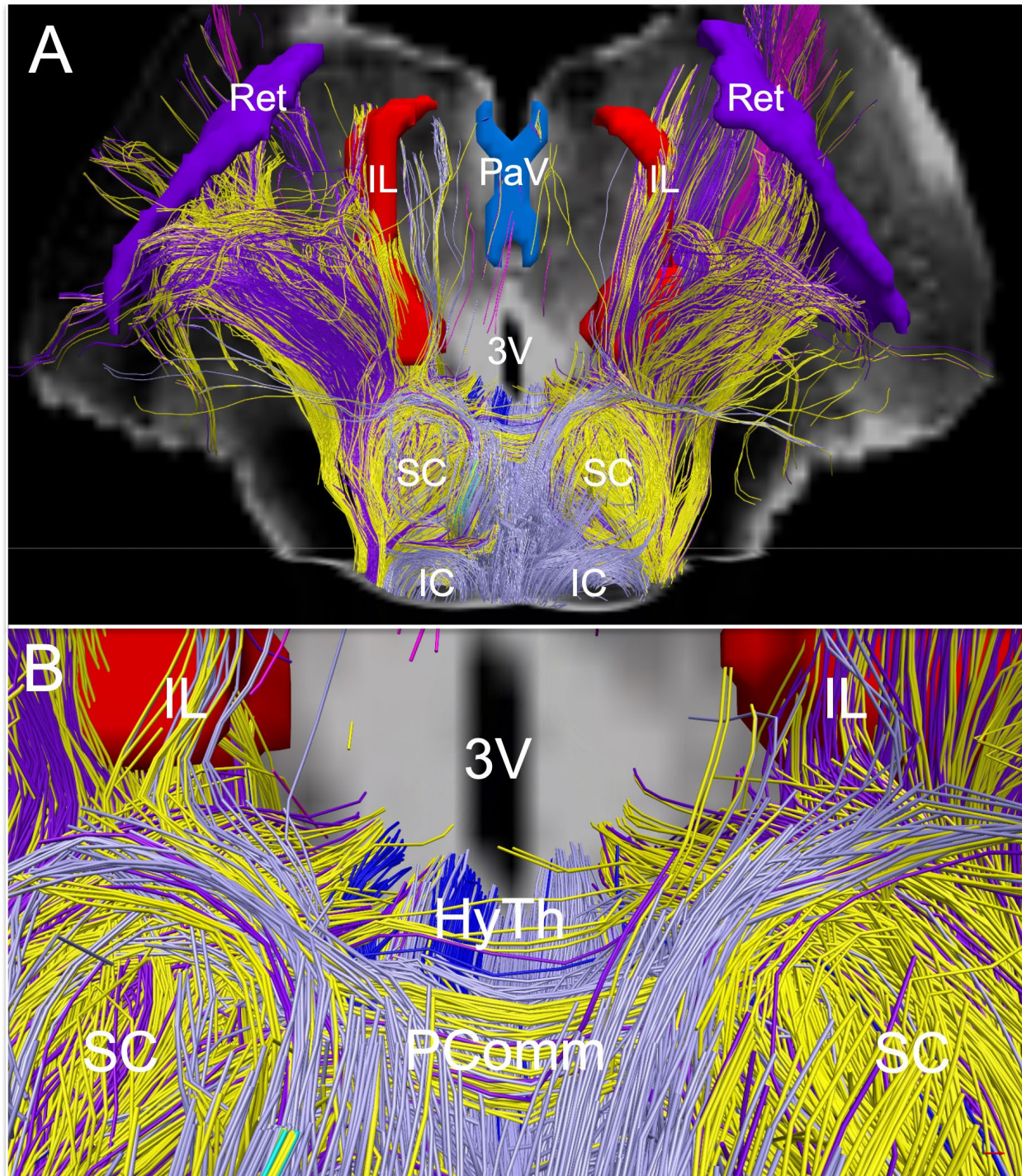


**Fig. 7. Extrareticular commissural and projection pathways of the default ascending arousal network.** Deterministic fiber tracts emanating from extrareticular arousal nuclei are shown from a dorsal perspective in (A) and a zoomed dorsal perspective in (B), superimposed on a coronal non-diffusion-weighted ( $b=0$ ) image at the level of the mid-thalamus. Tract color-coding is identical to that in Fig. 3. Projection fibers are seen connecting with the hypothalamus (HyTh; individual hypothalamic nuclei not shown for clarity), and thalamic arousal nuclei: intralaminar nuclei (IL), paraventricular nuclei (PaV), and reticular nuclei (Ret). Commissural



fibers cross the midline via the posterior commissure, with a high contribution of commissural fibers from the parabrachial complex (yellow), pedunculotegmental nucleus (dark purple), and periaqueductal grey (light purple).

### **Functional connectivity between the dAAN and DMN**

We used 7 Tesla resting-state fMRI (rs-fMRI) data from 84 healthy control subjects scanned in the Human Connectome Project (HCP) (56) to investigate the functional connectivity of the DMN with subcortical dAAN nodes. To map the DMN functional connectivity profile for each dAAN node, we used version 2.0 of the Harvard ascending arousal network (AAN) atlas (9) for brainstem nuclei. We used a previously published probabilistic segmentation atlas (57) for thalamic nodes, and an atlas proposed by Neudorfer et al. (58) for basal forebrain and hypothalamus nodes.

For each candidate brainstem, hypothalamic, thalamic, and basal forebrain node of the dAAN, we plotted the distributions of the DMN connectivity, as shown in Figure 8A. These analyses revealed a broad range of DMN connectivity within each candidate dAAN node. Several dAAN nodes contained voxels with positive correlations and negative correlations (i.e., anti-correlations) with the DMN. Within the brainstem, the VTA demonstrated the highest level of maximal DMN connectivity, while MnR showed the highest median level of DMN connectivity. Within the hypothalamus, thalamus and basal forebrain, the IL nucleus in the central thalamus demonstrated the highest level of maximal DMN connectivity, while the TMN nucleus in the hypothalamus showed the highest median level of DMN connectivity.

Given the complex relationship between structural and functional connectivity in cortical networks (59, 60), and the lack of data regarding structural-functional connectivity associations in subcortical networks, we plotted the relationship between functional connectivity mapped with *in vivo* 7 Tesla fMRI and structural connectivity mapped with *ex vivo* diffusion MRI (Figure 8B,

C) for connections between brainstem dAAN nodes and the cortical DM. In these analyses, the DMN was analyzed as a single target ROI. These structural-functional correlation plots revealed that several dAAN nodes, such as LDTg, MnR, and DR, had a high ratio of functional to structural connectivity, whereas other dAAN nodes, such as PAG, mRt, and PBC, had a high ratio of structural to functional connectivity. When grouping dAAN nodes by neurotransmitter system, serotonin and norepinephrine had high ratios of functional to structural connectivity, whereas glutamate had a high ratio of structural to functional connectivity.

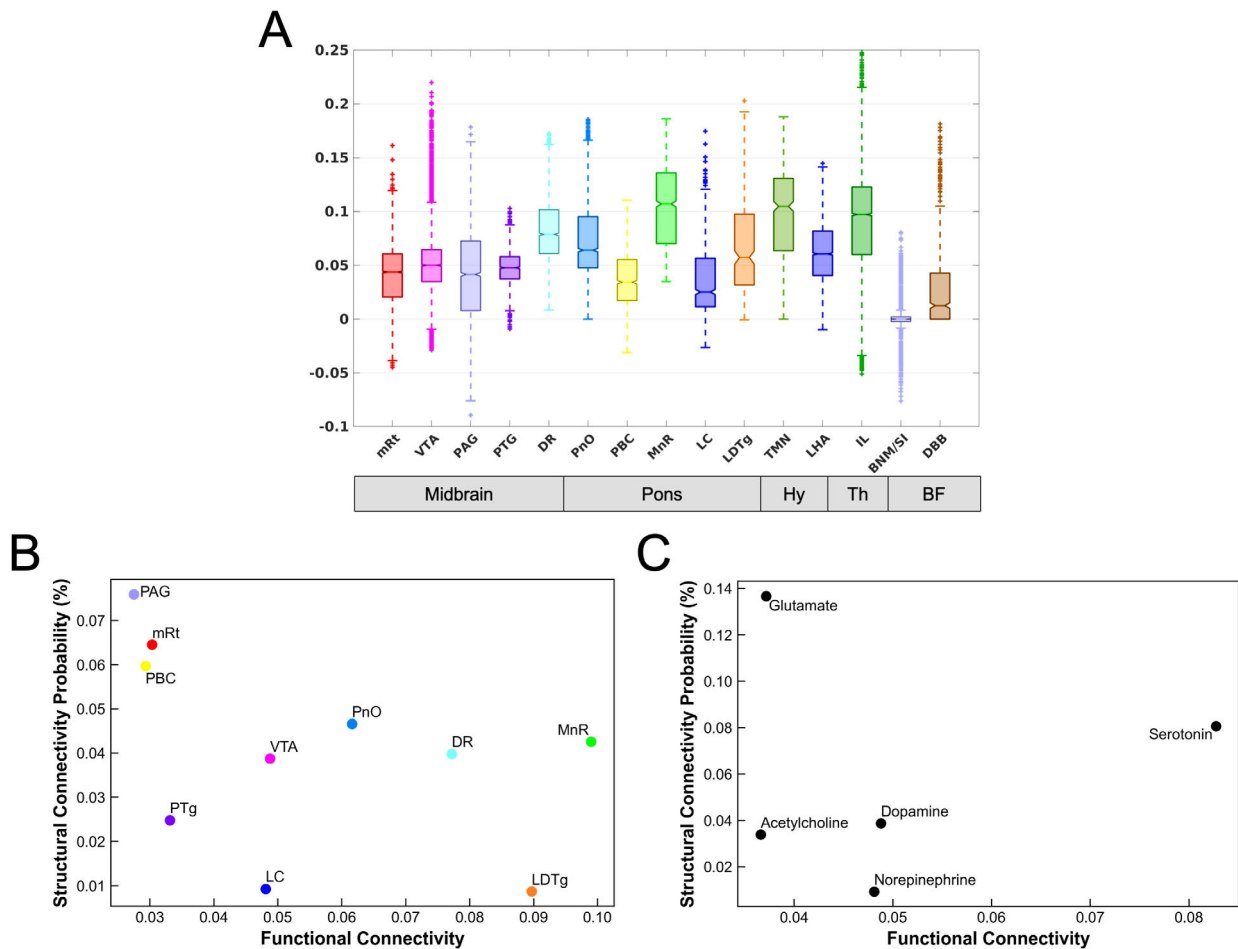


**Fig. 8. Functional connectivity between subcortical nodes of the default ascending arousal network and cortical nodes of the default mode network and their relationship to structural connectivity.** (A) Boxplots of the DMN functional connectivity for each dAAN node. Y-axis represents the strength of functional connectivity (unitless) relative to the cortical DMN connectivity measured by the NASCAR method. VTA voxels showed the highest level of maximal functional connectivity with the DMN, while MnR had the highest level of median

connectivity with the DMN. **(B)** Scatter plot between the mean of functional connectivity (x-axis) and the structural connectivity probability (y-axis) for each brainstem nucleus. **(C)** The counterpart grouped by the predominant type of neurotransmitter for each node: cholinergic = PTg and LDTg; dopaminergic = VTA; glutamatergic = PBC, mRt, and PnO; noradrenergic = LC; serotonergic = MnR and DR.

## DISCUSSION

In this multimodal brain imaging study, we map the connections of a proposed subcortical network that sustains resting wakefulness in human consciousness. We provide evidence for a human default ascending arousal network (dAAN) comprised of interconnected nodes linking brainstem, hypothalamic, thalamic, and basal forebrain nuclei that are known from prior animal and human studies to sustain resting wakefulness. Further, we identified patterns of extensive structural and functional interconnectivity between subcortical dAAN nodes and cortical DMN nodes, providing a putative architecture for the integration of arousal and awareness in human consciousness. Consistent with prior human (61) and animal (16, 18, 19, 62) studies, convergent structural connectivity data from *ex vivo* diffusion MRI tractography and functional connectivity data from *in vivo* 7 Tesla resting-state fMRI revealed that a midbrain dAAN node – the dopaminergic VTA – is a widely connected hub node at the nexus of subcortical arousal and cortical awareness networks. Yet connectivity maps also revealed variable relationships between structural and functional connectivity of dAAN nodes, with serotonergic and noradrenergic nodes showing higher levels of functional connectivity with the DMN than would be expected based on their structural connectivity. These observations provide a basis for further investigation of the structural and functional brainstem properties that modulate the human DMN. We release all imaging data, immunohistochemistry data and network-based autopsy

methods, including an updated atlas of dAAN brainstem nodes, to support efforts to map the connectivity of human consciousness.

### **The VTA is a widely connected dAAN node**

The VTA displayed extensive connectivity with other subcortical dAAN nodes and with cortical DMN nodes via multiple projection, association, and commissural pathways. Historically, the VTA was believed to mainly modulate behavior and cognition (62), but recent evidence from pharmacologic (63, 64), electrophysiologic (16), optogenetic (18, 19), and chemogenetic (65) methods, as well as behavioral experiments in dopamine knock-out mice (66), indicate that the VTA also modulates wakefulness. Functional connectivity studies from humans with disorders of consciousness further support the idea that the VTA modulates states of arousal, specifically via interactions with cortical DMN nodes (17). Our *ex vivo* diffusion MRI findings provide a structural basis for these functional observations in animals and humans, and our *in vivo* rs-fMRI findings provide further evidence for VTA-DMN connectivity, as VTA voxels showed the highest level of maximal functional connectivity of any brainstem dAAN node. These synergistic structural-functional connectivity findings solidify the role of dopaminergic VTA neurons in modulation of wakefulness, and hence consciousness (67).

Our observations supporting the role of the VTA as a potential dAAN hub node also reinforce ongoing efforts to target the dopaminergic VTA in therapeutic trials for patients with disorders of consciousness. Dopamine agonists and reuptake inhibitors are amongst the most commonly used pharmacologic therapies for patients with disorders of consciousness (68), and there is growing interest in using dopaminergic neuroimaging biomarkers to select patients for targeted therapies in clinical trials (69-71). The dAAN connectivity map and neuroimaging tools

released here can thus be used to inform the design of future therapeutic trials and to expand the therapeutic landscape for patients with disorders of consciousness.

### **Interconnectivity of the subcortical dAAN and cortical DMN in human consciousness**

Connections between brainstem arousal nuclei have been demonstrated using a variety of tract-tracing and electrophysiological techniques in multiple animal species (53, 72-76), but prior evidence of such interconnectivity is limited in the human brain (54, 77). Here, we provide structural and functional connectivity evidence for multiple dAAN association pathways (i.e., connections between ipsilateral brainstem nuclei) and commissural pathways (i.e., connections between contralateral brainstem nuclei) that to our knowledge have not been previously visualized in the human brain. Moreover, we expand upon prior observations pertaining to projection pathways of human brainstem arousal nuclei (i.e., connections between brainstem nuclei and the thalamus, hypothalamus, basal forebrain, and cerebral cortex) (9, 78-80).

We identified four projection pathways that connect the human brainstem to the diencephalon and forebrain: the ventral tegmental tract, caudal division (VTT<sub>C</sub>); ventral tegmental tract, rostral division (VTT<sub>R</sub>); dorsal tegmental tract, medial division (DTT<sub>M</sub>); and the dorsal tegmental tract, lateral division (DTT<sub>L</sub>). The anatomic trajectories and connectivity patterns of these dAAN projection pathways are consistent with prior studies of human brainstem connectivity (9, 54, 81, 82) and are similar to their rodent (53, 83), feline (76, 84), and primate (75) homologues.

Our observation of direct connections between brainstem arousal nuclei and the cerebral cortex in the human brain are also consistent with extensive evidence in animal species (74, 75, 85-90). We found that the MFB and LFB are the primary pathways by which the human

brainstem and cerebral cortex are connected, building upon prior observations about the human MFB (54, 78, 91, 92) and LFB (54). The human MFB travels through the hypothalamus and basal forebrain, carrying short-range tracts that connect with hypothalamic and basal forebrain nuclei via the VTT<sub>C</sub>. Long-range MFB fibers continue on to the cerebral cortex, connecting with DMN nodes within the frontal lobes. Although elucidation of the functional subspecialization of MFB and VTT<sub>C</sub> pathways in the human brain awaits future investigation, these structural connectivity results are consistent with wake-promoting brainstem-hypothalamus-basal forebrain circuits in animals (10).

We also observed tracts diverging from the MFB within the hypothalamus and basal forebrain, then entering the anterior limb of the internal capsule and appearing to connect with the frontal cortex. Though these capsular tracts have been observed in prior human tractography studies (78, 93), their anatomic accuracy has been called into question by primate tract-tracing and immunostaining studies that show MFB capsular axons terminating in the basal ganglia, not the frontal cortex (94). Given the possibility that these capsular tracts connecting with the frontal cortex are “false positives” (i.e., anatomically implausible tracts), we do not assign them as being part of the MFB. Rather, all MFB connectivity results (Table 2) and anatomic labels (Figure 4) reported here are based on tracts that pass through the hypothalamus and basal forebrain before connecting with frontal DMN nodes.

We found that the LFB is the primary pathway by which human dAAN nodes connect with the temporo-parietal DMN nodes, including the PMC (i.e., posterior cingulate and precuneus), a hub node within the DMN whose connectivity is believed to be essential for conscious awareness (11). Functional connectivity between the VTA and the PMC was recently shown to modulate consciousness in patients with severe brain injuries and healthy volunteers

receiving propofol sedation (61), observations that are supported by our VTA-PMC connectivity findings. Yet we also identified extensive DMN connectivity between multiple brainstem dAAN nodes beyond the VTA, with particularly strong connectivity in the PMC and MPFC nodes. Interestingly, midbrain dAAN nuclei showed more extensive connectivity with DMN nodes than did pontine dAAN nuclei. While a distance effect may partially account for this observation (i.e., the midbrain nodes are located in closer anatomic proximity to the DMN nodes), it is notable that three pontine nodes – PnO, PBC, and MnR – showed the highest connectivity with the MT node of the DMN in specimen 3. The functional significance of differential DMN connectivity patterns between midbrain and pontine dAAN nodes is unknown and requires future studies to evaluate the relative contributions of brainstem dAAN nuclei to modulating the DMN in the resting, conscious human brain.

### **Anatomic location and neurotransmitter profiles of dAAN nodes**

The 10 candidate brainstem dAAN nuclei that we identified from prior animal and human studies of arousal are all localized to the rostral pons and midbrain. The relationship between consciousness and brainstem nuclei in the rostral to mid-pons was demonstrated in Bremer's classical *cerveau isole* experiments in cats (95) and subsequently confirmed in brainstem transection studies by Moruzzi (96), Steriade (97) and others. Similarly, lesions in the mid-pons, rostral pons, and midbrain have been observed to cause coma in humans (98-102), whereas lesions in the caudal pons and medulla do not. Although there is evidence for medullary modulation of arousal in animals (103, 104) and medullary connectivity with rostral brainstem arousal nuclei in humans (54), we did not find a definitive brainstem arousal nucleus caudal to the mid-pons that satisfied the *a priori* criteria for consideration as a candidate dAAN node. The

analysis of medullary contributions to wakefulness and consciousness is beyond the scope of this paper and the subject of ongoing work.

Multiple candidate dAAN nodes contain GABAergic neurons, which modulate wakefulness via a variety of electrophysiological mechanisms. Amongst the glutamatergic neurons of the mesencephalic and pontine reticular formations (mRt and PnO), GABAergic neurons exert local inhibitory control upon the larger population of ascending stimulatory neurons (105). These GABAergic neurons may be responsible for the wake-promoting behavioral effects of PnO via local inhibition (i.e., “gating”) of REM sleep-promoting cholinergic neurons (38). Moreover, GABAergic neurons of the thalamic reticular nucleus (Ret) transition from intermittent burst-firing to tonic firing during the transition from slow-wave sleep to wakefulness (106). We found extensive connectivity between Ret and other dAAN nodes, consistent with prior electrophysiologic studies showing that Ret neurons synapse widely with ascending brainstem arousal inputs and receive inputs from arousal neurons of the basal forebrain (107, 108). Our connectivity findings thus reinforce the key role of GABAergic modulation of arousal in the human brain.

### **Applications of dAAN connectivity maps for patients with disorders of consciousness**

We expect that the network-based autopsy methods and connectivity data generated here will advance the study of coma pathogenesis and recovery (1). Classification of projection, association, and commissural pathways within the human dAAN will allow categorization of different combinations of preserved pathways in patients who recover from coma. This effort may ultimately enable identification of the minimum ensemble of nodes and connections that are sufficient for sustaining wakefulness in human consciousness. In addition, the dAAN



connectivity measures have the potential to inform prognostication and patient selection for therapeutic trials aimed at stimulating the dAAN and promoting recovery of consciousness (69).

Reemergence of consciousness after severe brain injury does not require the entire set of grey matter nodes and white matter connections that sustain wakefulness in the healthy human brain. Detailed clinico-anatomic studies of patients with focal brainstem lesions and brainstem axonal disconnections who recovered wakefulness after a period of coma convincingly illustrate this point (82, 98, 102, 109, 110), as do a multitude of animal studies showing that recovery of wakefulness is possible after experimental lesioning of brainstem or diencephalic arousal nuclei (111). Even in the classical *cerveau isole* experiments, in which cats are initially comatose due to transverse transection of the brainstem at the intercollicular level of the midbrain (112), some cats ultimately recover behavioral and electrophysiological evidence of wakefulness after several weeks (113). Similarly, prolonged coma (i.e.,  $\geq 4$  weeks) in human survivors of severe brain injury is extremely rare (114). Thus, identification of ensembles of dAAN connections that are compatible with recovery and receptive to therapeutic stimulation has potential to improve outcomes for patients with severe brain injuries (115).

The precise mechanisms by which residual connections enable reemergence of wakefulness after coma are unknown, but observational and therapeutic studies are beginning to identify specific subcortical circuits that mediate recovery of wakefulness after severe brain injury (1, 82, 116). Complementary evidence from neurophysiologic and cell culture studies suggests that neuronal networks can adapt to perturbations and reestablish normal function (117-119). These plasticity mechanisms provide a basis for functional reorganization of subsets of dAAN nodes in response to structural injury, suggesting that consciousness can be reestablished by variable combinations of network components (1).

These potential mechanisms of dAAN plasticity in humans recovering from coma are also consistent with theoretical models of the resilience and adaptability of neural systems. Modeling experiments suggest that neural systems with high complexity have high measures of degeneracy and redundancy, meaning that different elements within the system can perform the same function (*120*). These model-based observations are supported by human therapeutic studies in patients with disorders of consciousness (*115*), which suggest that there are multiple targets for pharmacologic or electrophysiologic reactivation of arousal circuits (*17, 23, 121-125*). Considering animal evidence for electrical coupling of arousal nuclei (*126*), one interpretation of these human therapeutic trials is that stimulation of different network nodes may lead to a final common pathway of increased functional coupling within the entire arousal network.

### **Limitations and methodological considerations**

In deterministic and probabilistic tractography, a fiber tract represents an inferential model of axonal pathways based upon measurements of directional water diffusion along these pathways. The number of axons that corresponds to a tract depends partly on the spatial resolution (i.e., voxel size) of the diffusion data. In the experiments reported here, the voxel size was almost 1,000 times larger in dimension than the diameter of a single axon (~600-750 microns versus ~1 micron). Hence, the tractography results reported here do not represent “ground truth” axonal anatomy. All tractography results should be considered inferential and are subject to the inherent methodological limitations of diffusion MRI tractography, which have been well characterized (*127-131*).

Given these methodological limitations, our tractography-based definition of anatomic connectivity does not prove synaptic connectivity, which will require confirmation in future

studies that move from the mesoscale connectome (i.e., ~600 to 750  $\mu\text{m}$  resolution) to the microscale synaptome (i.e., ~1-10  $\mu\text{m}$ ), a major area of ongoing study in neuroscience (132). However, there are currently no available methods to integrate our mesoscale human connectome map with prior microscale animal synaptome wiring diagrams (73). Innovations such as CLARITY (133) and polarization-sensitive optical coherence tomography (134) provide hope for this endeavor, but an integrated connectome-synaptome map of the dAAN is currently out of reach.

Another limitation is that diffusion tractography cannot determine the direction of electrical signaling within a tract. There is extensive electrophysiological evidence for “top-down” modulation of arousal (135, 136) and cognition (137), and the MFB is known to carry descending fibers alongside its ascending fibers (138). In addition, multiple types of neurons within the arousal network may have bifurcating axons with ascending and descending projections (89). Thus, our use of the term “ascending” is not intended to suggest that arousal is mediated solely by ascending pathways from the brainstem to rostral sites. Rather, homeostatic functions such as arousal are modulated by bi-directional “bottom-up” and “top-down” signaling between the brainstem, diencephalon, basal forebrain, and cerebral cortex.

It is also important to consider that false positive tracts can be generated by a “highway-effect” whereby tracts that run alongside one another can merge into anatomically implausible pathways. Conversely, false negative findings can occur due a variety of factors, including increased distance between nodes and tractography’s low sensitivity for identifying axons with multidirectional branching patterns (139, 140), small diameters (75), and/or lack of myelination (75). These latter anatomic features are known characteristics of the rostral serotonergic, noradrenergic, and cholinergic axonal projections, which may explain the

absent or uncertain connectivity findings for MnR, LC, and LDTg (see Table 2). We attempted to mitigate these problems by performing dMRI with a spatial resolution of 600-750  $\mu\text{m}$  and an angular resolution of 60-90 diffusion-encoding directions. Further, we tested for connectivity between each candidate dAAN node and an anatomically implausible control node to empirically derive a “noise window”, and we only considered connections that exceeded this statistical threshold. Yet even with high-resolution data and strict statistical thresholds, the possibility of false positive and false negative structural connectivity remains.

We also acknowledge that the present study does not address functional subspecialization, or fractionation, of different circuits within the dAAN. Given that dAAN nodes contain neurons utilizing multiple neurotransmitters (7), there is substantial intra-nodal functional complexity that is not accounted for in our structural connectivity methods, which treat each node as a singular entity. For example, the PnO contains neurons involved in activation of REM sleep (141), generation of the hippocampal theta rhythm (142), and active movement during waking (143), but here we considered the PnO solely as an arousal nucleus because of its population of wake-promoting GABAergic neurons (38). Similarly, the PTg contains diverse populations of cholinergic, glutamatergic, and GABAergic neurons with different roles in modulation of wakefulness (144). Nodal parcellation of the PnO, PTg and other multi-function nodes will require future dAAN fractionation studies, just as fractionation of DMN nodes was performed in the years following the DMN’s discovery (145, 146).

## **Conclusions and future directions**

We provide insights into the connectivity of a subcortical arousal network that sustains resting wakefulness in the conscious human brain. We found that subcortical dAAN nodes interconnect

with cortical DMN nodes, providing a neuroanatomic basis for integration of arousal and awareness in human consciousness. The dAAN connectivity map and neuroanatomic taxonomy proposed here aims to facilitate further study into the role of subcortical arousal pathways in human consciousness and its disorders. The small size and neuroanatomic complexity of the human brainstem renders it inherently difficult to study, but as new neuroimaging tools are developed to investigate human brainstem connectivity (147-152), we expect that it will be possible to refine this dAAN connectivity map and definitively identify the networks that sustain human consciousness.

## MATERIALS AND METHODS

### Identification of candidate dAAN nodes

We identified candidate dAAN nodes via four lines of previously published evidence: electrophysiological, gene expression, lesion, and stimulation. Specifically, we identified subcortical nuclei for which prior studies demonstrated any one of the following: 1) tonic activity during resting wakefulness (28, 153); 2) increased Fos staining after periods of arousal (154); 3) lesion-induced loss of resting wakefulness (95); or 4) stimulation-induced arousal (13) (see **Table 1**). Animal electrophysiology, gene expression, lesion, and stimulation studies were identified using reference lists from text books (28, 111, 155-158), review articles (10, 106, 159-162), and from the authors' reference libraries.

These *a priori* criteria do not stipulate that dAAN nodes must release excitatory neurotransmitters. Although the overall influence of the dAAN on the cerebral cortex is activating, multiple lines of theoretical and experimental evidence indicate that inhibitory circuits

are essential for the modulation and stability of activating networks (158, 163-165). At a circuit level, GABAergic neurons exert multiple types of inhibition, including feedback, feed-forward and lateral inhibition. These inhibitory mechanisms enhance the nonlinearity and complexity of neural networks, and hence their resiliency and stability during perturbations (28). Of particular relevance to wakefulness, *in vivo* and *in vitro* animal studies suggest that GABAergic neurons coordinate the synchronous fast activity of subcortical arousal neurons (7, 135, 162). We therefore consider nodes containing GABAergic inhibitory neurons as candidate dAAN nodes.

Of note, the nodes and connections of the dAAN need not be the same as those that facilitate state changes. For example, the hypothalamic and brainstem nodes of the subcortical “flip-flop switch” that mediates transitions between sleep and wake (161) are not necessarily the same nodes that sustain wakefulness once it is established. Rather, the flip-flop switch may activate a distinct or overlapping set of dAAN nodes once the transition from sleep to wakefulness has occurred. Here, we focus exclusively on the nodes and connections of the dAAN that sustains the resting mode of the wakeful state.

### **Brain specimen acquisition and processing**

Written informed consent for brain donation was obtained postmortem from family surrogate decision-makers, in accordance with a research protocol approved by the Institutional Review Board at Mass General Brigham. Criteria for brain specimens being included in the study were: 1) no history of neurological illness; 2) no abnormal *in vivo* brain scan; 3) normal neurological examination documented by a clinician in the medical record prior to death; and 4) normal postmortem gross examination of the brain by a neuropathologist. All specimens were fixed in 10% formaldehyde.

## **Ex vivo MRI data acquisition**

For Specimen 1, we dissected the hemispheres from the diencephalon and basal forebrain, and dissected the cerebellum from the brainstem to fit the specimen into the small bore of a 4.7 Tesla MRI scanner, as previously described (9). The dissected specimen consisted of the rostral pons, midbrain, hypothalamus, thalamus, basal forebrain, and part of the basal ganglia. Specimens 2 and 3 were scanned as whole brains on a large-bore 3 Tesla MRI scanner. Immediately prior to scanning, the specimens were transferred from 10% formaldehyde to Fomblin (perfluoropolyether, Ausimont USA Inc., Thorofare, NJ), which reduces magnetic susceptibility artifacts (166).

### *Diffusion MRI of dissected specimen*

Specimen 1 was scanned in a small horizontal-bore 4.7 Tesla MRI scanner (Bruker Biospec), as previously described (9). We utilized a 3-dimensional diffusion-weighted spin-echo echo-planar imaging (DW-SE-EPI) sequence, with 60 different diffusion-weighted measurements at  $b = 4057$   $\text{s/mm}^2$ . One dataset of 3D DW-SE-EPI data with  $b = 0$   $\text{s/mm}^2$  was also acquired to calculate quantitative diffusion properties in each voxel. Additional sequence parameters were: gradient strength = 12.4 G/cm, duration  $\delta = 13.4$  msec, intertemporal pulse offset  $\Delta = 25$  msec, repetition time (TR) = 1000 msec, echo time (TE) = 72.5 msec, and spatial resolution = 562 x 609 x 641  $\mu\text{m}$ . Total diffusion scan time was 2 hours and 10 minutes.

### *Diffusion MRI of whole brain specimens*

Specimens 2 and 3 were scanned as whole brains on a 3 Tesla Tim Trio MRI scanner (Siemens Medical Solutions, Erlangen, Germany) using a 32-channel head coil. To increase diffusion sensitivity on the large-bore 3 Tesla MRI clinical scanner that was required to scan a whole brain

specimen, diffusion data were acquired using a 3D diffusion-weighted steady-state free-precession (DW-SSFP) sequence (47, 167). DW-SSFP is an SNR efficient approach that can achieve diffusion weighting without requiring long TE, making it well suited for *ex vivo* samples characterized by short T2 (168). We acquired 90 diffusion-weighted volumes and 12 b=0 volumes at 750  $\mu\text{m}$  isotropic spatial resolution. Total diffusion scan time was 30 hours and 31 minutes per specimen. In contrast to the classic DW-SE-EPI sequence utilized for specimen 1, the diffusion-weighting for a DW-SSFP sequence is not defined by a single global  $b$  value, as it depends on other tissue and imaging properties, such as the T1 relaxation time, the T2 relaxation time, the TR, and the flip angle (167). Using the formulation in (168) and previously reported *ex vivo* estimates of T<sub>1</sub>, T<sub>2</sub>, and diffusivity (D) (T<sub>1</sub>= 400 ms, T<sub>2</sub>=45 ms, D=0.08x10<sup>-3</sup> mm<sup>2</sup>/s) we computed an “effective” b-value of 3773 s/mm<sup>2</sup> (169).

### **Cortical surface parcellation of whole brain specimens**

We parcellated the cortical nodes of the DMN in whole brain specimens 2 and 3 for the dAAN-DMN connectivity analysis. DMN nodes were parcellated according to the canonical Yeo 7-network atlas (170), as instantiated in the 1000-node Schaefer version of the atlas (171) available at

[https://github.com/ThomasYeoLab/CBIG/tree/master/stable\\_projects/brain\\_parcellation/Schaefer2018\\_LocalGlobal/Parcellations/project\\_to\\_individual](https://github.com/ThomasYeoLab/CBIG/tree/master/stable_projects/brain_parcellation/Schaefer2018_LocalGlobal/Parcellations/project_to_individual).

First, to generate cortical surfaces for identification of DMN nodes, we acquired multi-echo flash (MEF) data at 1 mm isotropic resolution on the 3 Tesla Tim Trio MRI scanner during the same scanning session during which the diffusion data were acquired. Key MEF sequence



parameters were TR = 23.00 msec, TE = 2.64 msec, and 6 flip angles of 5° to 30° were collected at 5° increments. Synthetic T1 and proton density (PD) maps were estimated directly from the MEF acquisitions using the DESPOT1 algorithm (*172*), available through the FreeSurfer (<http://surfer.nmr.mgh.harvard.edu>) utility “mri\_ms\_fitparms” (*173*).

### **Cortical surface generation and neuroanatomic localization of DMN nodes**

To generate the cortical surface model, the synthesized PD volume was processed to remove extraneous background noise by thresholding the PD volume to create a mask containing hyperintense voxels. The mask was then subtracted from the initial PD volume to achieve a more homogenous image. Using the intensity-corrected PD volume, we then generated white and grey matter segmentations using the modified Sequence Adaptive Multimodal Segmentation (SAMSEG) pipeline (*174*). The SAMSEG white and grey matter segmentations were then used to generate the pial and white matter surfaces.

Once the surfaces were generated, we performed surface-based atlas registrations to create labels corresponding to the DMN nodes in the canonical Yeo atlas: posteromedial complex (PMC; i.e., posterior cingulate cortex and precuneus), medial prefrontal cortex (MPFC), inferior parietal lobule (IPL), lateral temporal lobe (LT), and medial temporal lobe (MT). To translate the surface-based MEF labels into volumetric diffusion space we used the boundary-based registration (*175*) method available through FreeSurfer. Using the transformation matrix obtained through coregistration, we then translated our atlas labels from MEF surface space to volumetric diffusion space for further analysis. We then projected the Yeo atlas labels onto those surfaces using a fixed 2 mm distance into the surface via a nonlinear spherical transform (*176*).

Detailed processing parameters are provided in our code, which we release at [https://github.com/ComaRecoveryLab/Network-based\\_Autopsy](https://github.com/ComaRecoveryLab/Network-based_Autopsy). All data were processed using a standard release of FreeSurfer 7.1.2 available at <https://github.com/freesurfer/freesurfer> and FSL 6.0.3 available at <https://fsl.fmrib.ox.ac.uk/fsl/fslwiki>.

### **Sectioning and staining for histologic-radiologic correlations**

Upon completion of *ex vivo* MRI data acquisition, specimen 1 was divided into seven blocks, which were embedded in paraffin. We then cut serial transverse sections of the rostral pons and midbrain, and coronal sections of the hypothalamus, thalamus, and basal forebrain at 10  $\mu\text{m}$  thickness (LEICA RM2255 microtome, Leica Microsystems, Buffalo Grove, IL, USA). Every 50<sup>th</sup> section was stained with hematoxylin-and-eosin for nuclei and counterstained with Luxol fast blue for myelin, yielding a stained section every 500  $\mu\text{m}$ . The purpose of these stains was to define the neuroanatomic location, borders, and morphology of all candidate dAAN nodes. Additionally, 10  $\mu\text{m}$  sections from the midbrain were prepared using tyrosine hydroxylase (Pel-Freez Biologicals; rabbit polyclonal P40101) counterstained with hematoxylin, and 10  $\mu\text{m}$  sections from the pons were prepared using tryptophan hydroxylase (Sigma-Aldrich; mouse monoclonal AMAB91108) counterstained with hematoxylin. Tyrosine hydroxylase more precisely characterizes the location, borders and morphology of the dopaminergic ventral tegmental area (VTA), as detailed in the **Supplementary Material**. Tryptophan hydroxylase characterized the location, borders and morphology of the serotonergic median raphe (MnR) and dorsal raphe (DR).

### **Histology-guided neuroanatomic localization of brainstem dAAN nodes**

For specimen 1, candidate dAAN nodes (i.e., nodes selected based on the *a priori* criteria) were traced on the diffusion-weighted images using histological guidance. Each diffusion image was compared to its corresponding histological section to ensure that radiologic dAAN nodes shared the same location and morphology as the histological dAAN nuclei (**Figs. S4, S5**). Histological nuclei were delineated by visual inspection of their cytoarchitecture with a light microscope and with digitized slides. We then cross-referenced with the Paxinos atlas of human brainstem neuroanatomy for brainstem dAAN nodes (51) and with the Allen Institute atlas of the human brain for thalamic, hypothalamic, and basal forebrain dAAN nodes (52). Since brainstem nuclei change shape, size and contour along the rostro-caudal axis, histological guidance of dAAN node tracing was performed for every axial diffusion image using its corresponding histological section, yielding a 3-dimensional model of brainstem arousal nuclei.

For specimens 2 and 3 the brainstem dAAN nuclei were also traced manually on each diffusion MRI dataset, but with reference to canonical atlases and selected immunostains, not serial immunostains or comprehensive histological data. Specifically, the neuroanatomic boundaries of brainstem nodes were visually confirmed with respect to two reference templates: 1) the *ex vivo* template of histologically guided nodes generated for specimen 1, which we release here as part of the Harvard Disorders of Consciousness Histopathology Collection (<http://histopath.nmr.mgh.harvard.edu>); and 2) the Paxinos human brainstem atlas (51).

### **Histology-guided neuroanatomic localization of diencephalic and forebrain dAAN nodes**

Similar to the brainstem nucleus segmentation, we used histological guidance via coronal sections through the diencephalon and basal forebrain to identify the borders of thalamic,

hypothalamic, and basal forebrain dAAN nodes on the diffusion MRI dataset for Specimen 1. To segment the thalamic, hypothalamic, and basal forebrain nuclei for specimens 2 and 3, we manually traced each node based on the Allen Institute human brain atlas (52).

### **Overview of *ex vivo* diffusion MRI diffusion data processing for tractography**

We processed the *ex vivo* diffusion datasets for deterministic and probabilistic tractography analyses to generate insights into both qualitative anatomic relationships of dAAN tracts and quantitative dAAN connectivity properties. Deterministic tractography yields more visually informative qualitative data about the neuroanatomic relationships between tracts (e.g., sites of tract branching and crossing) (54, 151), whereas probabilistic tractography provides a more reliable quantitative measure of connectivity between nodes because it accounts for uncertainty in tract trajectories and can detect tracts on and past grey matter boundaries (177).

Diffusion data from all three specimens were processed for deterministic fiber tracking, and diffusion data from specimens 2 and 3 were processed for probabilistic fiber tracking. Specimen 1 was excluded from the probabilistic tractography analysis because it was scanned using different acquisition parameters, which precludes comparison of quantitative probabilistic data with Specimens 2 and 3 without complex modelling that falls outside of the scope of these experiments. To optimize consistency across methods, we standardized the deterministic and probabilistic processing parameters wherever possible. For example, we did not apply an FA threshold to the deterministic or probabilistic analyses because low FA has been observed in the rostral brainstem tegmentum (9, 178), and thalamus (179) in the human brain. We confirmed this observation in an FA analysis of tracts emanating from the mRt in specimen 1, which showed low FA in multiple segments of mRt tracts passing through the brainstem tegmentum

(**Fig. 2.** These low FA measurements may be attributable to the complex meshwork of crossing fibers within the brainstem tegmentum (84), varying degrees of myelination within brainstem axons (75), and/or nuclei that are interspersed amongst the axons (51). Additional details regarding deterministic and probabilistic processing parameters, such as the selection of angle thresholds and the rationale for not applying a distance correction, are provided in the **Supplementary Material.**

### **Deterministic tractography analysis of dAAN connectivity**

For deterministic tractography, diffusion data for all three specimens were processed in Diffusion Toolkit 6.3 (180). Orientation distribution functions (ODFs) for each voxel were obtained utilizing a spherical harmonic q-ball reconstruction approach (181) and whole brain tractograms were generated using the FACT algorithm and the ODF's principle diffusion directions (182). Q-ball reconstruction accounts for the possibility of multiple diffusion directions within each voxel, thus enhancing detection of crossing, splaying, and/or "kissing" fibers within complex neuronal networks (183, 184). DAAN tracts were isolated manually in TrackVis, version 6.1 (180), using each candidate dAAN nucleus as an inclusion region of interest. Tracts were visually analyzed to determine the trajectories, branching patterns, and anatomic relationships between bundles connecting the candidate dAAN nodes as well as dAAN-DMN connections.

### **Probabilistic tractography analysis of dAAN connectivity**

For probabilistic tractography, diffusion data for the two whole-brain specimens (specimens 2 and 3) were processed using FMRIB's Diffusion Toolbox, version 6.0.6. Estimates of principle

diffusion orientation in each voxel were obtained using the ball-and-stick model (177, 185) in bedpostx with two stick compartments. Tractography was performed using probtrackx with default parameters. Connectivity was analyzed between all candidate dAAN nodes using the “network” flag. For each pair of nodes, 5,000 tracts (i.e., streamlines) were propagated from each voxel within the seed node, and the target node was treated as both a “termination mask” and a “waypoint mask” (54, 151).

### Statistical Analysis of Connectivity

We computed an undirected connectivity probability ( $CP$ ) for each pair of nodes (i.e., node A and node B) by performing two analyses: 1) node A was treated as a seed and node B as a target; and 2) node B was treated as a seed and node A as a target. Using this symmetric connectivity model (186), we computed  $CP_{A \rightarrow B}$ ,  $CP_{B \rightarrow A}$ , and  $CP_{A \leftrightarrow B}$ :

$$CP_{A \rightarrow B} = \frac{k_A}{n_A}$$

$$CP_{B \rightarrow A} = \frac{k_B}{n_B}$$

$$CP_{A \leftrightarrow B} = \frac{k_A + k_B}{n_A + n_B}$$

$k_A$  = # tracts from Node A reaching Node B

$k_B$  = # tracts from Node B reaching Node A

$n_A$  = 5000 x # seed voxels in Node A

$n_B$  = 5000 x # target voxels in Node B

$CP_{A \leftrightarrow B}$  hence represents the probability of a tract connecting node A and node B, weighted by the number of voxels within each node and invariant to direction (81, 82). Importantly, the symmetric model reduces a potential statistical bias in probabilistic tractography: the probability of a connection between node A and node B being underestimated if node A has widely

distributed connectivity. The probability of a tract connecting with node B would therefore decrease as the probability of that tract connecting with other nodes increases. The symmetric model mitigates, though does not eliminate, this potential bias.

Although complete elimination of false-positive tracts (i.e., anatomically implausible connections) is not possible with either probabilistic or deterministic tractography, we attempted to account for the possibility of false-positive tracts by comparing  $CP$  values for each candidate brainstem dAAN node with two control nodes: the basis pontis (BP) and the red nucleus (RN). Based on prior anatomic labeling studies in animal models, BP and RN are not expected to have significant connectivity with the candidate brainstem dAAN nodes (e.g., (53)), as they mainly contain cortico-ponto-cerebellar fibers that connect the cerebellum to the primary motor cortex (and vice versa), the primary function of which is motor activity (187). We established two *a priori* criteria, both of which must be met, for operationally defining a structural connection between a pair of candidate dAAN nodes (nodes A and B): 1)  $CP_{A \leftrightarrow B} > 0$ ; and 2) the 95% confidence interval (CI) for  $CP_{A \leftrightarrow B}$  must not overlap with the 95% CI for any of the following-  $CP_{A \leftrightarrow BP}$ ,  $CP_{A \leftrightarrow RN}$ ,  $CP_{B \leftrightarrow BP}$ , and  $CP_{B \leftrightarrow RN}$ .

The 95% CI for each  $CP$  measurement was calculated by modeling  $CP$  as a binomial distribution:

$$variance = \frac{CP(1 - CP)}{N}$$
$$95\% CI = CP \pm 1.96 \times \sqrt{\frac{CP(1 - CP)}{N}}$$

where  $N = n_A + n_B$ .

The binomial statistical model depends upon the assumption that the success of each trial (i.e., the likelihood that a tract from the seed will connect with the target) is independent from prior trials. This assumption may not always be valid, because there is a possibility of intra-voxel dependence (i.e., the success of tract 1 launched from voxel 1 may be dependent on the success of tract 2 launched from voxel 1) and inter-voxel dependence (i.e., the success of tract 1 launched from voxel 1 may be dependent on the success of tract 1 launched from voxel 2). Nevertheless, deriving a quantitative model of these dependencies would require accounting for multiple anatomic factors that likely vary from node to node, or even from voxel to voxel, and is therefore beyond the scope of the present study. Crucially, the binomial model likely overestimates variance because it does not account for the aforementioned dependencies. Hence, we believe that the binomial model implemented here is a conservative approach for estimating *CP* variance and the 95% CI.

### **Proposed neuroanatomic taxonomy for the human dAAN**

We classified dAAN connections as projection, association, or commissural. This classification system is intended for use as a neuroanatomic taxonomy for the subcortical dAAN, akin to that of cortical networks whose connections are classified in these terms (55). In the cortical classification system, the cortex is the frame of reference for defining fiber pathways. Projection fibers project from the cortex to subcortical regions. Association fibers connect ipsilateral cortical regions, and commissural fibers cross the midline to connect contralateral cortical regions.

Here, we propose that the brainstem is the frame of reference for classifying fiber pathways of the dAAN. As such, projection fibers are defined as those that project from



brainstem nuclei to rostral diencephalic nuclei, basal forebrain nuclei, and/or cortical regions that mediate consciousness (i.e., DMN nodes). Association fibers connect brainstem nuclei to ipsilateral brainstem nuclei, and commissural fibers cross the midline to connect with contralateral brainstem nuclei.

### **7 Tesla resting-state functional MRI of dAAN-DMN connectivity**

7 Tesla resting-state fMRI (rs-fMRI) scans from 84 healthy controls in the Human Connectome Project (HCP) (56) were used in this study. The rs-fMRI data were minimally preprocessed, resampled, and co-registered to the MNI template by the HCP pipeline (188). Grayordinate representations of the data were used for joint analysis of cortical and subcortical connectivity, where cortical data were sampled onto the subject surface, and subcortical data were represented in volumetric space (188). We did not apply any further spatial smoothing to the minimally preprocessed data because typical Gaussian smoothing would mix signals across different functional regions (189), which may cause a significant issue when resolving relationships between nuclei in dAAN (190). Instead, the improved SNR was obtained using a tensor-based group analysis, as described below.

Using our previously developed pipeline (191), we estimated the functional connectivity from dAAN to the canonical DMN. Specifically, we first temporally synchronized the rs-fMRI data of each subject to a group average using the group BrainSync algorithm (192, 193). We further arrange the synchronized data from all subjects along the third dimension (the first dimension is space, and the second dimension is time), forming a 3D data tensor. We then applied the NASCAR tensor decomposition method (194, 195) to discover the whole-brain

DMN. The subcortical section was separated from the grayordinate structure and converted to a volumetric NIFTI file.

To extract the connectivity profile for each nucleus in dAAN, we used version 2.0 of the Harvard Ascending Arousal Network (AAN) Atlas (9) for brainstem nuclei, the probabilistic segmentation atlas (57) for thalamic nuclei, and an atlas proposed by Neudorfer et al. (58) for basal forebrain and hypothalamus nuclei to define the regions of interest (ROI). We then, for each ROI, plot the distributions of the DMN connectivity values using box plots. Of note, three candidate diencephalic dAAN nodes – the supramammillary nucleus of the hypothalamus (SUM), the paraventricular nucleus of the thalamus (PaV), and the reticular nucleus of the thalamus (Ret), were not included in the MRI atlases.

## SUPPLEMENTARY MATERIALS

**Abbreviations:** AAN = ascending arousal network; ARAS = ascending reticular activating system; CEM/Pf = centromedian/parafascicular nucleus of the thalamus; CHN = central homeostatic network; CL = central lateral nucleus of the thalamus; CnF = cuneiform nucleus; CTT = central tegmental tract; dAAN = default ascending arousal network; DBB = diagonal band of Broca; DMN = default mode network; DR = dorsal raphe; DTT = dorsal tegmental tract; DTT<sub>L</sub> = dorsal tegmental tract, lateral division; DTT<sub>M</sub> = dorsal tegmental tract, medial division; DWI = diffusion-weighted imaging; EEG = electroencephalography; FA = fractional anisotropy; fMRI = functional magnetic resonance imaging; IC = inferior colliculus; LC = locus coeruleus; LDTg = laterodorsal tegmental nucleus; LFB = lateral forebrain bundle; LHA = lateral hypothalamic area; MFB = medial forebrain bundle; ML = medial lemniscus; MLF = medial longitudinal fasciculus; MnR = median raphe; MPFC = medial prefrontal cortex; MRI = magnetic resonance imaging; mRt = mesencephalic reticular formation; NBM = nucleus basalis of Meynert; PAG; periaqueductal grey; PBC = parabrachial complex; PBP = parabrachial pigmented nucleus of the ventral tegmental area; PComm = posterior commissure; PIF = parainterfascicular nucleus; PMC = postero-medial complex (i.e. posterior cingulate and precuneus); PN = paranigral nucleus of ventral tegmental area; PnO = pontine reticular nucleus = oral part (pontis oralis); PTg = pedunculotegmental nucleus; PV = paraventricular nucleus of the thalamus; Ret = reticular nucleus of the thalamus; RIs = retroisthmus nucleus; RLi = rostral linear nucleus; RMg = raphe magnus; SC = superior colliculus; SCP = superior cerebellar peduncle; SI = substantia innominata; SN = substantia nigra; TM = tuberomammillary nucleus; VLPO = ventrolateral pre-optic area; VTA = ventral tegmental area; VTAR = ventral tegmental area, rostral part; VTT = ventral tegmental tract; VTT<sub>C</sub> = ventral tegmental tract, caudal division; VTT<sub>R</sub> = ventral tegmental tract, rostral division.

## **SUPPLEMENTARY METHODS**

### **A representative animal electrophysiological study of arousal**

In 1982, Steriade and colleagues tested the hypothesis generated by Moruzzi and Magoun in 1949 that the brainstem reticular formation drives tonic activation of thalamocortical circuits, and therefore cortical EEG desynchronization, by increasing firing rates during wakefulness versus slow-wave sleep (35). Rather than using electrical stimulation or lesion-based techniques, Steriade and colleagues recorded extracellularly the spontaneous firing of mRt neurons while seven cats were awake, sleeping, or transitioning between these states, as determined by cortical EEG patterns. MRt neuron firing rates were significantly higher during wakefulness than sleep. This finding was most prominent in mRt neurons projecting rostrally versus caudally (i.e., to the paramedian pons). Moreover, the increase in firing rate corresponded to EEG and behavioral evidence of wakefulness and was tonic in nature, suggesting a direct link between mRt activity, activation of the cortical EEG, and behavioral evidence of wakefulness. These results suggest that the mRt plays an important role in sustaining wakefulness as part of the dAAN.

### **Overview of neuroanatomic localization of candidate dAAN nodes**

To facilitate reproduction of our methods, we describe the neuroanatomic boundaries of the candidate brainstem dAAN nodes in **Tables S1-S5**. In addition, we detail our approach to defining the neuroanatomic borders of each nucleus. We use the Paxinos atlas as our primary reference (48), but we also consider differences between the Paxinos atlas and the Olszewski and Baxter brainstem atlas (50), another canonical brainstem atlas of human neuroanatomy. Where applicable, we explain our rationale for mediating discrepancies in anatomic borders and/or nomenclature between these atlases, as well as between these atlases and other neuroanatomic

studies. Finally, we explain for each brainstem dAAN node how the nomenclature and borders proposed here differ from those that our laboratory has used previously (9, 54, 99, 109, 151), including in our prior analyses of Specimen 1 (9, 99). At the completion of this process, we updated the Harvard Ascending Arousal Network Atlas and now release version 2.0 of the atlas (doi:10.5061/dryad.zw3r228d2; download link:

<https://datadryad.org/stash/share/aJ713eXY12ND56bzOBejVG2jmOFCD2CKxdSJsYWEHkw>).

### **Neuroanatomic localization of midbrain dAAN nodes**

#### Mesencephalic Reticular Formation (mRt):

The mRt is a region of the midbrain tegmentum that has been described using multiple names and as containing multiple subnuclei by different neuroanatomists. In Olszewski and Baxter's atlas, the most caudal aspect of the midbrain tegmentum, at the level of the isthmus, contains the cuneiform nucleus (CNF). The remainder of the caudal midbrain tegmentum, at the level of the decussation of the SCP, contains the mesencephalic reticular formation (MRF) and the mesencephalic reticular formation, ventral part (MRFv). Olszewski's MRF nucleus continues rostrally and traverses the entire rostro-caudal extent of the midbrain, up to the mesencephalic-diencephalic junction. The MRFv's rostral border ends at the mid-level of the red nuclei. In the rostral midbrain, at the level of the red nuclei, a small intracuneiform nucleus (ICUN) is shown within the MRF.

In Paxinos' atlas, the most caudal aspect of the midbrain tegmentum, at the level of the isthmus, similarly contains CnF. However, another subnucleus named the isthmus reticular formation (isRt) is located in this region dorsal to the pedunculotegmental nucleus (PTg) and ventral to the CnF. In Paxinos' atlas, the remainder of the caudal midbrain tegmentum, at the

level of the decussation of the SCP, contains the CnF and isRt. At the transition from the decussation of the SCP to the red nuclei, the CnF and isRt nomenclature changes to the precuneiform area (PrCnF) and mesencephalic reticular formation (mRt), respectively. In the rostral midbrain, at the level of the red nuclei, the entire tegmentum is comprised of the mRt, which extends from the PAG on its dorso-medial border to the medial lemniscus on its ventro-lateral border. Within the rostral portion of the mRt, Paxinos defines a small subnucleus called the central mesencephalic nucleus (CeMe) in the same region that Olszewski defines the ICUN. Finally, at the mesencephalic-diencephalic junction, Paxinos' mRt becomes the p1 reticular formation (p1Rt) (plates 8.62 to 8.64).

In summary, Olszewski and Paxinos describe a similar region of the midbrain tegmentum as containing a cluster of arousal nuclei, albeit with different nomenclature and different subnuclei. The region of the midbrain tegmentum that is described by Olszewski as containing CNF, MRF, MRFv, and ICUN is described by Paxinos as containing CnF, isRt, PrCnF, mRt, CeMe, and p1Rt. In our prior work (9), we used the term cuneiform/subcuneiform nucleus (CSC) to describe this region. We traced it in the rostral midbrain, in deference to Moruzzi and Magoun's seminal study in which stimulation of the rostral midbrain tegmentum led to arousal and cortical activation in lightly anesthetized cats (13). We now update our nomenclature from CSC to mRt to ensure consistency with the Paxinos atlas' nomenclature. Furthermore, we have extended our mRt region of interest (ROI) to include all of the aforementioned subnuclei described by Olszewski and Paxinos, such that our mRt ROI now extends throughout the entire rostro-caudal axis of the midbrain tegmentum. Specifically, our mRt ROI contains all of the following subnuclei described by Paxinos: CnF, isRt, PrCnF, mRt, CeMe, and p1Rt.

### Periaqueductal Grey (PAG):

The anatomic borders and contours of our PAG ROI are consistent with those of the PAG described in Paxinos. We trace the PAG as a single ROI, which encompasses multiple subnuclei described in Paxinos. Specifically, our PAG ROI includes the following subnuclei described by Paxinos: lateral PAG (LPAG); dorsolateral PAG (DLPAG); dorsomedial PAG (DMPAG); pleioglial PAG (PIGl); and p1 PAG (p1PAG).

### Pedunculotegmental Nucleus (PTg):

The PTg ROI contains both the pars compactus (called PTg by Paxinos) and the pars dissipatus (called the retroisthmus nucleus [RIs] by Paxinos). The pars dissipatus is called nucleus tegmenti pedunculopontinus, subnucleus dissipatus by Olszewski and the diffuse medial component of Ch5 by Mesulam (196). We have not changed our operational definition of neuroanatomic localization of the PTg, but we have updated our nomenclature from pedunculopontine nucleus (PPN) to PTg to ensure consistency with nomenclature of the Paxinos atlas. Our PTg ROI thus contains the PTg and RIs, as described by Paxinos. In addition, we made one edit to the boundaries of PTg in the Harvard AAN Atlas version 2.0, as compared to version 1.0: in version 2.0, we deleted one voxel in the PTg at MNI axial level z53 and reassigned this voxel to the VTA, based on tyrosine hydroxylase staining data and based on the anatomic boundaries in the Paxinos atlas.

### Dorsal Raphe (DR):

The DR nucleus extends from the rostral pons to the caudal midbrain. We classify DR as a midbrain nucleus, because that is where most DR neurons are located. Paxinos shows DR

continuing rostrally past the caudal border of the red nuclei. However, in our experience studying human brainstem specimens, serotonergic DR neurons do not extend past the rostral border of the trochlear nucleus, which is at the caudal border of the red nucleus. Our DR ROI includes the following subnuclei described by Paxinos: DR, caudal part (DRC); DR, dorsal part (DRD); DR, interfascicular part (DRI); DR, lateral part (DRL); DR, ventral part (DRV); posterodorsal raphe nucleus (PDR).

#### Ventral Tegmental Area (VTA):

The VTA ROI used in this study has two major differences compared to the prior VTA ROI used by our group and with version 1.0 of the Harvard Ascending Arousal Network Atlas: 1) its lateral extent and 2) its rostral extent. In our prior work, we did not include the lateral wing-like extensions of the PBP, as shown in Paxinos and in Pearson (197), because this subregion is difficult to differentiate from the nearby substantia nigra. However, with our new tyrosine hydroxylase immunostaining (Figure 1) and with reference to the Paxinos atlas, we were able to make this distinction between PBP and SN for the present studies.

The VTA node proposed here also has a more rostral extent than the VTA ROI that we used in prior studies (9, 99). Previously, we based the neuroanatomic borders of the VTA on hematoxylin-and-eosin-stained sections from human brainstem specimens, which revealed the highest density of catecholamine neurons, as demonstrated by the presence of neuromelanin, in the caudal midbrain. However, we recognize that VTA neurons have been identified in the rostral mesencephalon by other laboratories using a variety of staining techniques, such as tyrosine hydroxylase (86, 198). Thus, we performed new tyrosine hydroxylase stains on four midbrain sections from Specimen 1 (<https://histopath.nmr.mgh.harvard.edu>). These stains



revealed a distribution of VTA neurons that was consistent with that described in the studies by Oades, Halliday, Pearson, and colleagues (**Figure 2**). Therefore, we use a VTA ROI in the present work that extends throughout the entire rostro-caudal axis of the midbrain. Finally, we do not include the rostral linear nucleus as part of the VTA, although some dopaminergic cells may reside in this region (86), because this nucleus is primarily serotonergic.

Finally, we edited the midline portion of the VTA node, based on the observation that VTA neurons in the midline of the midbrain were only seen at the level of the red nucleus, not at the level of the superior cerebellar peduncle. This immunostaining observation is consistent with the VTA anatomic borders in the Paxinos atlas along the rostro-caudal axis of the midbrain. Thus, we removed the midline VTA voxels at the level of the superior cerebellar peduncle in version 2.0 of the Harvard AAN atlas.

In summary, the VTA ROI used in this study contains the following nuclear subregions described by Paxinos: parainterfascicular nucleus (PIF); paranigral nucleus of ventral tegmental area (PN); ventral tegmental area (VTA); ventral tegmental area, rostral part (VTAR); and parabrachial pigmented nucleus of the VTA (PBP). This VTA ROI contains the A10 nuclei, as described by Oades and Halliday (86). The neuroanatomic borders of the VTA ROI contain the following subregions described by Olszewski: the paranigral nucleus (PNg), interfascicular nucleus (INF), parabrachial pigmented nucleus (PBP), and ventral tegmental area of Tsai (VTA).

### **Neuroanatomic localization of pontine dAAN nodes**

#### Pontine Reticular Nucleus, Oral Part (i.e., Pontis Oralis; PnO):

We have not changed the neuroanatomic localization of this nucleus since our prior studies (9), but we have updated our nomenclature from PO to PnO to reflect the Paxinos atlas's

nomenclature. Our PnO nucleus includes the following subnuclei described by Olszewski: nucleus reticularis pontis oralis (NRPO) and nucleus reticularis tegmenti pontis (NRTP). Paxinos does not subdivide PnO into these two subnuclei.

#### Parabrachial Complex (PBC):

The PBC is divided in the Paxinos atlas into medial and lateral components: medial parabrachial nucleus (MPB) and lateral parabrachial nucleus (LPB). MPB and LPB are further subdivided into subregions: MPB, external part (MPBE); LPB, central part (LPBC); LPB, dorsal part (LPBD); LPB, external part (LPBE); LPB, superior part (LPBS). Given the difficulty of delineating these subregions on MRI scans of the human brain, even at the ultra-high spatial resolution (~600  $\mu\text{m}$ ) at which Specimen 1 was imaged, we grouped all of these medial and lateral subregions into a single PBC node. This is the same approach that we used to delineate the PBC in our previous analyses of Specimen 1.

Of note, the caudal boundary of PBC in Paxinos (MPB) is located at plate 8.35, but we operationally define the caudal boundary to be located at the level of plate 8.37, which is the caudal border of the pontine arousal nuclei. Similarly, the rostral boundary of PBC in Paxinos' atlas is located at plate 8.49 but we operationally define the PBC as extending to plate 8.50, which is the transition point between PBC and PTg at the ponto-mesencephalic junction.

#### Median Raphe Nucleus (MnR):

In accordance with the terminology used by Paxinos, we define the MnR as comprising both the MnR proper and the slightly more lateral subnucleus, the paramedian raphe nucleus (PMnR). The PMnR begins in the midpons on plate 8.38, ventral to the dorsal raphe and medial to the

nucleus pontis oralis. It is joined medially by the MnR on plate 8.44 and disappears prior to the isthmus, on plate 8.48. The MnR continues rostrally into the caudal midbrain, ending at the level of the decussation of the superior cerebellar peduncle. As with the PBC (above), we operationally define the caudal and rostral boundaries of our MnR ROI as plates 8.37 and 8.50, respectively, since these are the anatomic levels of the mid-pons and the ponto-mesencephalic junction. Our MnR ROI encompasses the MnR and paramedian raphe nucleus.

#### Locus Coeruleus (LC):

This small, tubular nucleus begins in the dorsolateral midpons, on Paxinos plate 8.37, lateral to the fourth ventricle and medial to the superior cerebellar peduncle. It extends rostrally to the isthmus on plate 8.49. As with PBC and MnR above, we operationally consider the LC as extending to 8.50, which is the ponto-mesencephalic junction. The neuroanatomic location, borders and nomenclature for LC are similar in the Olszewski and Paxinos atlases.

#### Laterodorsal Tegmental Nucleus (LDTg):

Using Paxinos' terminology, we do not include the ventral nucleus, which is labeled the laterodorsal tegmental nucleus, ventral part (LDTgV), as part of our annotation of the LDTg. The LDTg is immediately adjacent to the medial edge of the LC. It lies dorsal to the medial longitudinal fasciculus (mLF), while the LDTgV is the subarea ventral to the mLF. It begins several levels rostral to the mid-pons (plate 8.41) and terminates at the level of the trochlear nucleus (8.51). As with PBC, MnR, and LC above, we operationally consider the LDTg as extending to 8.50, which is the ponto-mesencephalic junction.

## **Neuroanatomic localization of thalamic dAAN nodes**

### Intralaminar Nuclei (ILN):

Using the terminology of the Ding Brain Atlas (49), this collection of thalamic subnuclei includes the central lateral (CL), central medial (CeM), paracentral (PC), central dorsal (CD), centromedian (CM), parafascicular (Pf), subparafascicular (SPf) and the fasciculosus (Fa) nuclei. These subnuclei form an arc with a ventro-posterior bulge and are bordered medially by the dorsomedial nucleus and laterally by ventral anterior nucleus, ventral posterior nucleus and pulvinar.

### Reticular Nucleus (Ret):

The reticular thalamic nucleus includes the magnocellular (Rmc) and parvocellular (Rpc) divisions (49) and forms the anterior and lateral border of the thalamus. Posteriorly, at the level of the lateral geniculate nucleus, it is laterally separated from the pulvinar by a thin layer of white matter.

### Paraventricular Thalamic Nucleus (PaV):

The paraventricular thalamic nucleus (PaV) lines the medial border of the thalamus. On its medial side is the third ventricle. On its lateral side are several different thalamic nuclei along its antero-posterior extent: anteriorly, the lateral border of PaV is formed by ILN and the anterior nuclear complex; posteriorly, the lateral border of PaV is formed by the mediodorsal nucleus of the thalamus. The superior border of PaV is formed by the stria medullaris of the thalamus, and the inferior border of PaV is formed by the midline nuclear complex.

## **Neuroanatomic localization of hypothalamic dAAN nodes**

### Lateral Hypothalamic Area (LHA):

This region is subdivided into anterior (LHAa), posterior (LHAp) and tuberal regions (LHA<sub>tub</sub>) and forms the lateral border of the hypothalamus with the substantia innominata of the basal forebrain (49). The anterior-most region is not depicted in the Allen atlas. The tuberal region begins posterior to the ventrolateral pre-optic area (VLPO) and is subdivided into a magnocellular nucleus (LHmc), accessory secretory cells (LHsc) and a pallidohypothalamic area (PalHy). The posterior region extends to the posterior border of the hypothalamus, dorsal to the mammillary bodies and includes the perifornical nucleus (PeF).

### Tuberomammillary Nucleus (TM):

This nucleus has an anterior component within the LHA<sub>tub</sub>, just medial to the optic tract. Posteriorly, it sits laterally to the mammillary bodies and inferior to the LHAp.

### Supramammillary Nucleus (SUM):

This nucleus is located superior to the mammillary body and mammillothalamic tract. It is bordered medially by the posterior hypothalamic nucleus and laterally by the LHA and the TMN.

## **Neuroanatomic localization of basal forebrain dAAN nodes**

### Basal Nucleus of Meynert/Substantia Innominata (BNM/SI):

The BNM and SI are identified as a single region in our studies, as they cannot be anatomically distinguished using MRI. They occupy the area lateral to the hypothalamus and ventral to the

pallidum, extending anteriorly to the level of the anterior commissure and posteriorly to the posterior boundary of the amygdala (49).

#### Nucleus of the Diagonal Band (NDB):

The NDB includes vertical and horizontal subdivisions. It exists in its vertical orientation anterior to the anterior commissure, in the midline, medial to the septal nucleus and nucleus accumbens. At the level of the anterior commissure, it condenses ventrally into its horizontal subdivision, forming the border between the hypothalamus and the SI (49).

#### **Methodologic Considerations for Deterministic and Probabilistic Tractography**

To ensure consistency across methods, we standardized the deterministic and probabilistic processing parameters wherever possible, as detailed in the main text.

Some processing parameters, however, were not standardized due to differences in the deterministic and probabilistic techniques. For example, in all deterministic experiments, fiber tracts were terminated when the angle between water diffusion vectors in adjacent voxels exceeded a threshold of 60°. This angle threshold was previously identified by our group as providing a balance between tract sensitivity (i.e. identification of the brainstem's widely branching pathways) and tract specificity (i.e. reduction of false positive tracts) (9, 54, 99). In contrast, we and other groups typically use a more liberal angle threshold of 80° (curvature threshold = 0.2), for probabilistic experiments, consistent with the default setting in FSL's Diffusion Toolbox. Notably, a recent *ex vivo* probabilistic tractography study that compared the accuracy of fiber tract data in the macaque brain to "gold standard" tract-tracer data found that probabilistic tract accuracy was minimally affected when angle thresholds were in the range of

70-90° (186). Similarly, the accuracy of the probabilistic tractography data was not affected by varying the FA thresholds between 0.0-0.3.

We did not include a distance correction (e.g., the “-pd” function in FSL’s *probtrackx*) in our *CP* calculations. Although the probability of a connection between two anatomic regions, as detected by tractography, may be associated with the distance between the regions (199), it is unknown whether this association is linear or exponential. Moreover, the type of distance correction that is appropriate for a given bundle of tracts likely depends upon multiple variables, including the number of voxels in the seed/target nodes, the number of other bundles that intersect the bundle of interest along its course, and the geometry of the bundle (e.g. its curvature and branching). From a statistical perspective, it is unclear if a single distance correction method can account for the effect of distance on connectivity measures for different bundles.

Furthermore, empiric data from a recent *ex vivo* MRI study of the macaque brain, which tested linear and exponential distance correction methods, found that the accuracy of probabilistic tractography data against gold-standard tract-tracing data was not improved by either distance correction method (186). Thus, we did not correct for inter-nodal distance in our *CP* measurements.

## Supplementary Videos

**Video S1. The Harvard Ascending Arousal Network (AAN) Atlas – Version 2.0.** AAN brainstem nodes are rendered in three dimensions and superimposed upon the MNI152 atlas in 1 mm isotropic space. For anatomic reference, the nodes are shown on an axial image at the level of the mid-pons, a sagittal image at the midline, and a coronal image at the splenium of the corpus callosum. Blue = locus coeruleus; yellow = parabrachial complex; green = median raphe; orange = laterodorsal tegmental nucleus; light blue = pontis oralis; turquoise = dorsal raphe; red = mesencephalic reticular formation; purple = pedunculotegmental nucleus; light purple = periaqueductal grey; pink = ventral tegmental area.

**Video S2. Visualizing default ascending arousal network connectivity within the ventral tegmental area hub node.** All candidate brainstem dAAN nodes and their tract end-points are shown from a dorsal perspective, as in Fig. 6, superimposed upon a coronal non-diffusion-weighted ( $b=0$ ) image at the level of the mid-thalamus and an axial  $b=0$  image at the intercollicular level of the midbrain. Tract end-points appear as disks and represent the start-points and termination-points of each tract (i.e., there are two end-points per tract). All tract end-points are color-coded by the node from which they originate, and the nodes are rendered semi-transparent so that end-points can be seen within them.

As the video begins, tract end-points are seen within the semi-transparent brainstem candidate nodes: ventral tegmental area (VTA), periaqueductal grey (PAG), and mesencephalic reticular formation (mRt), pedunculotegmental nucleus (PTg), and parabrachial complex (PBC). As the video proceeds, the viewer's eye moves ventrally through the PAG. Once the viewer's eye emerges from the ventral surface of the PAG, the dorsomedial border of the VTA is seen, where tract end-points from multiple candidate brainstem dAAN nodes overlap within the VTA and along its dorsal border: pedunculotegmental, parabrachial complex, and dorsal raphe (PTg-PBC-DR); pontis oralis, DR, and PTg (PnO-DR-PTg); and PBC-mRt-PTg. Tract end-point overlap does not prove synaptic connectivity but indicates extensive connectivity via association pathways between ipsilateral and midline dAAN nodes with the VTA.



## Supplementary Figures

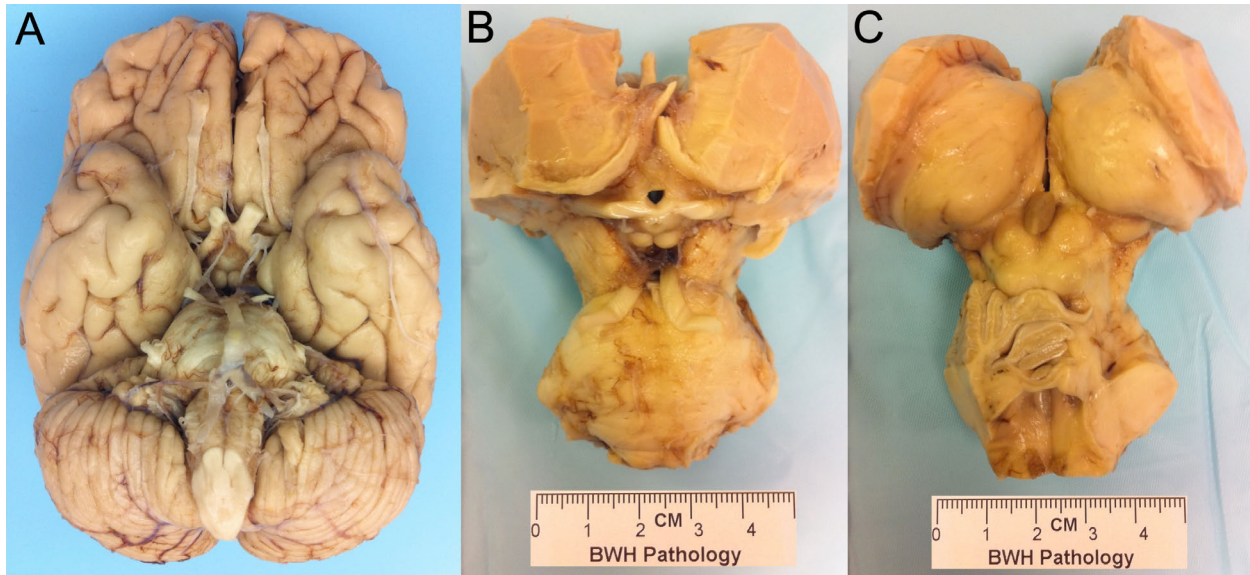


**Fig. S1. Gross pathology photos of Specimen 1.** (A) Inferior view of brain Specimen 1. The whole brain was dissected to a brainstem/diencephalon/forebrain specimen consisting of the pons, midbrain, hypothalamus, thalamus, basal forebrain, and portions of the basal ganglia, as shown from an (B) anterior and (C) posterior perspective. CM = centimeters. Figure adapted from Edlow et al. JNEN 2012 (9).

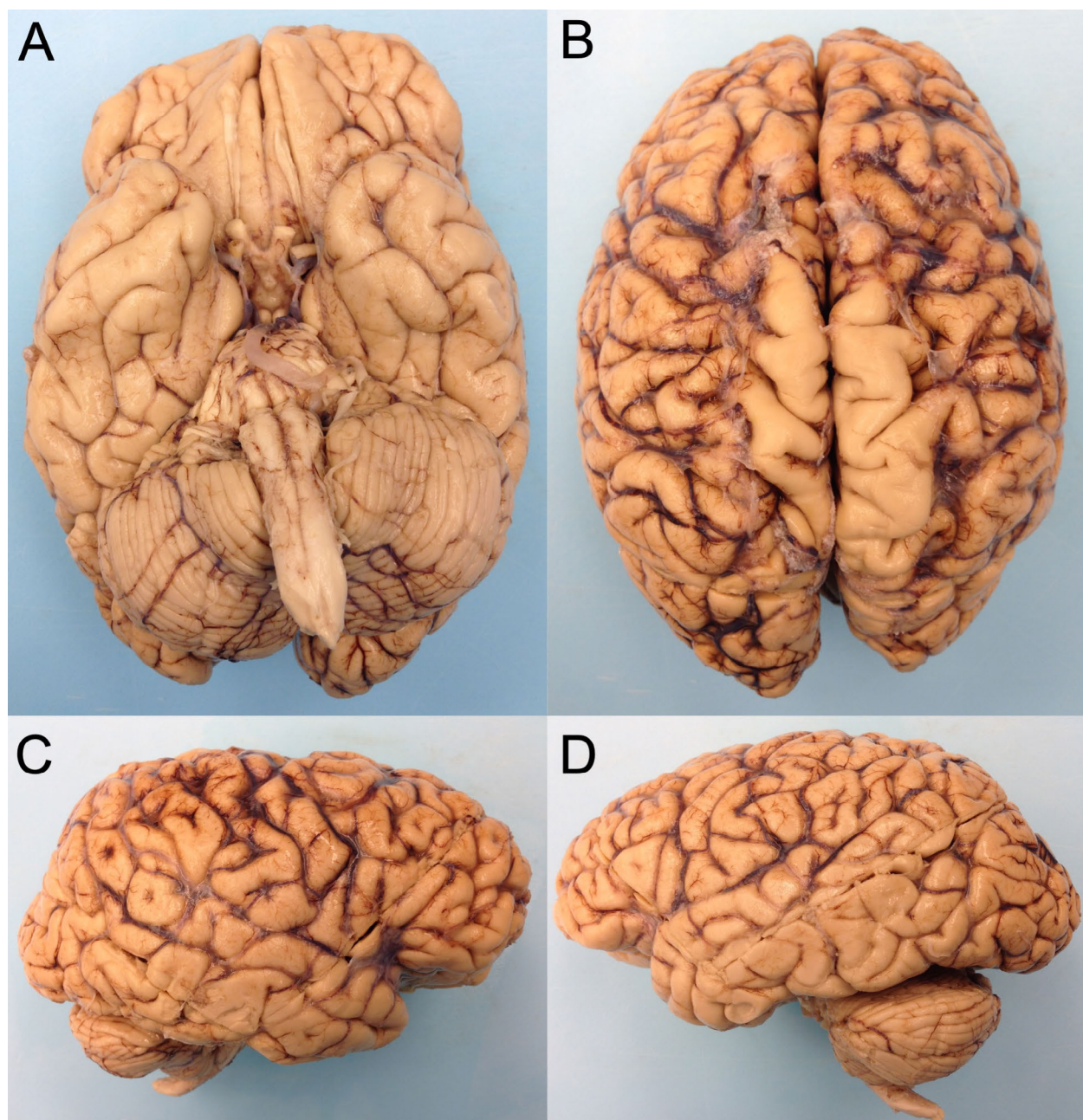


**Fig. S2. Gross pathology photos of Specimen 2.** Brain Specimen 2 is shown from an (A) inferior, (B) superior, (C) right lateral, and (D) left lateral perspective.

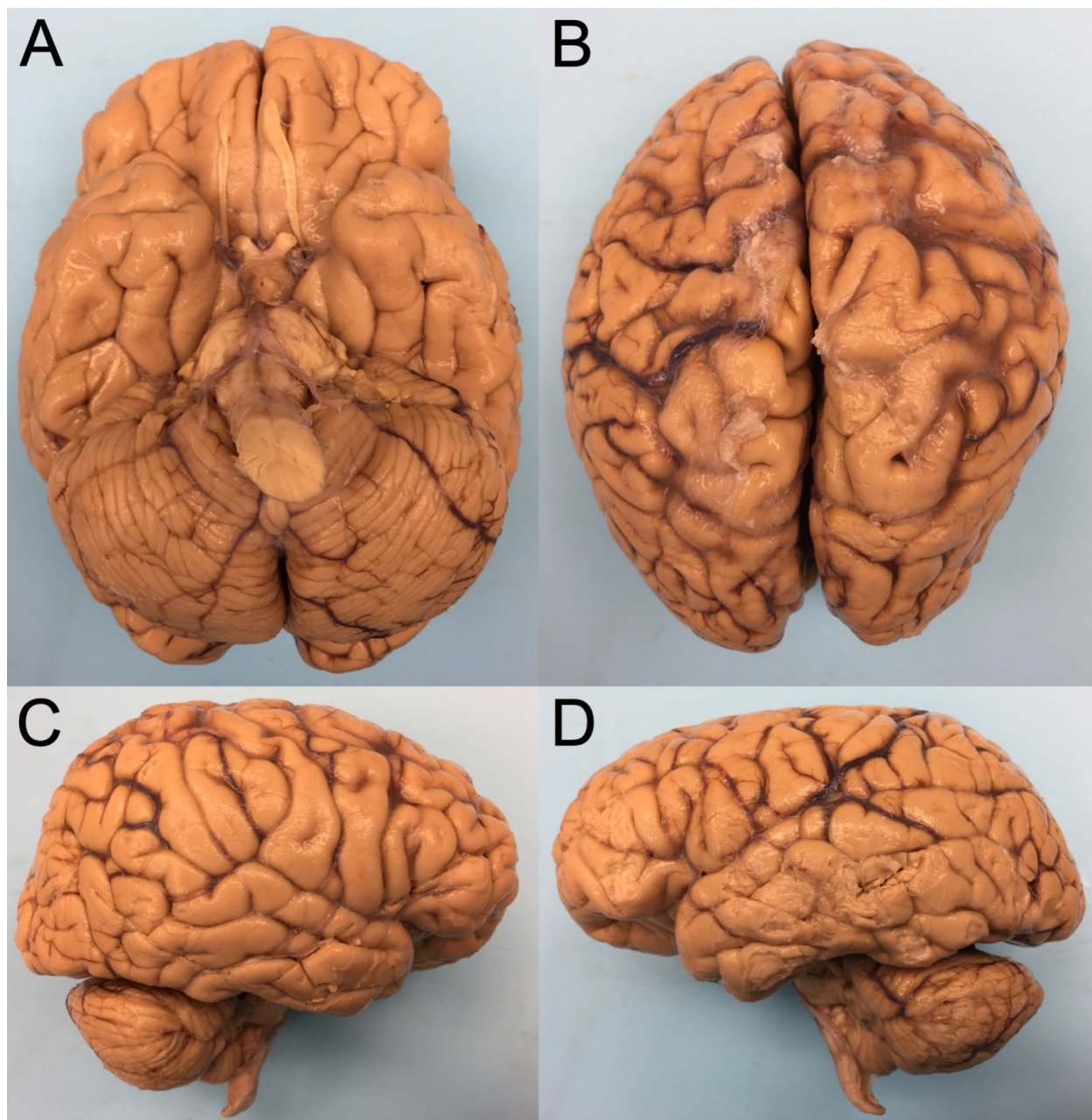


**Fig. S3. Gross pathology photos of Specimen 3.** Brain Specimen 3 is shown from an (A) inferior, (B) superior, (C) right lateral, and (D) left lateral perspective.

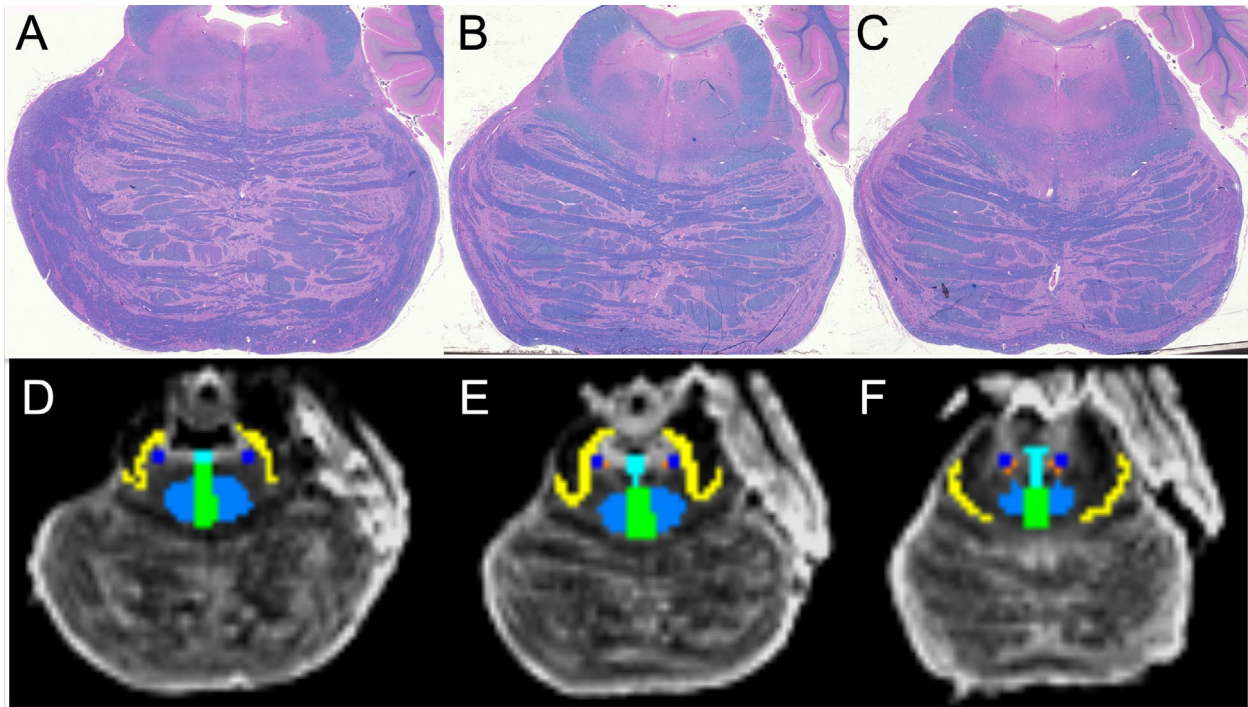


**Fig S4. Neuroanatomic Localization of Pontine Arousal Nuclei.** Axial histologic sections through the mid pons (**A**), upper pons (**B**) and rostral pons (**C**) for Specimen 1. Each section is stained with hematoxylin and eosin/Luxol fast blue. Corresponding axial non-diffusion-weighted ( $b=0$ ) images (**D**, **E**, **F**). Regions of interest for tractography are traced on the  $b=0$  images with neuroanatomic borders determined by the histological stains: light blue = pontis oralis; turquoise = dorsal raphe; dark blue = locus coeruleus; yellow = parabrachial complex; green = median raphe; orange = laterodorsal tegmental nucleus. Figure adapted from Edlow et al. JNEN 2012 (9).

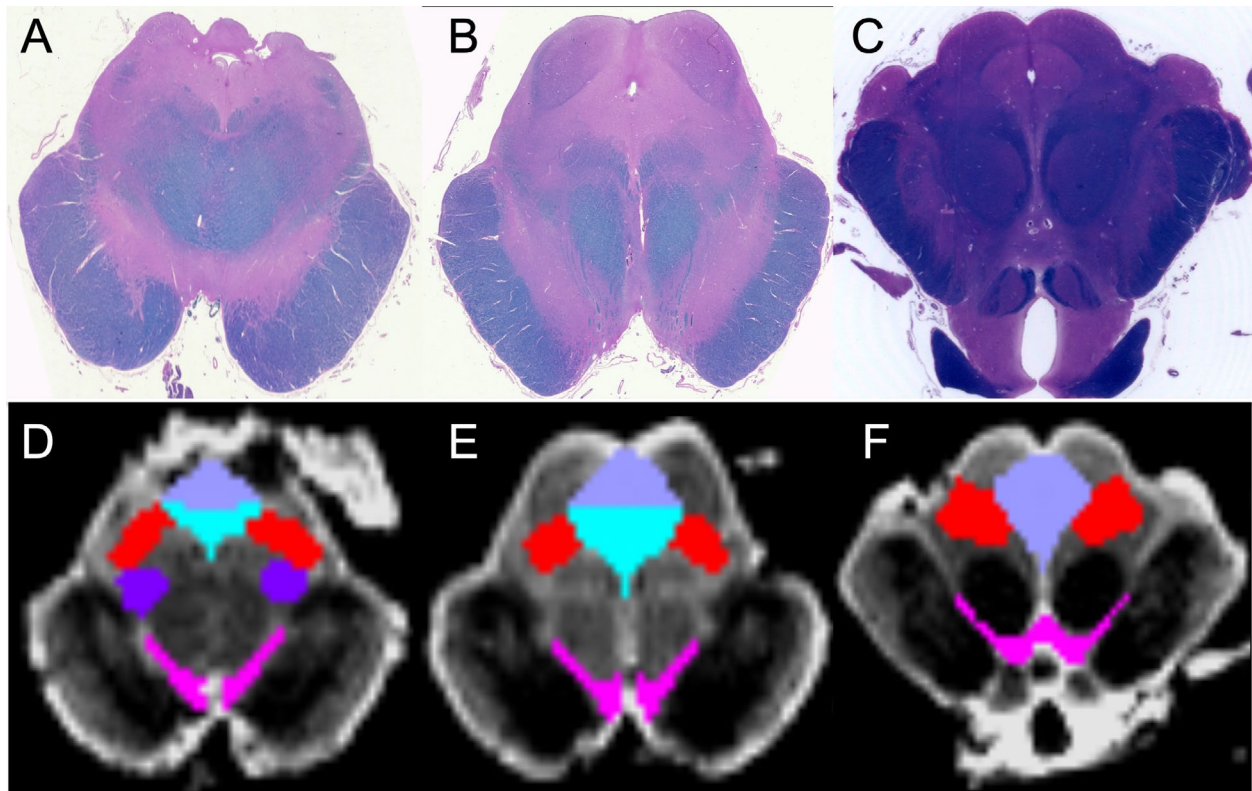


**Fig. S5. Neuroanatomic Localization of Midbrain Arousal Nuclei.** Axial histologic sections through the midbrain at the level of the decussation of the superior cerebellar peduncles (**A**), at the level of the inferior colliculi (**B**) and at the level of the superior colliculi and red nuclei (**C**) in Specimen 1. All sections are stained with hematoxylin and eosin/Luxol fast blue. Corresponding axial non-diffusion-weighted ( $b=0$ ) images (**D**, **E**, **F**). Regions of interest for tractography are traced on the  $b=0$  images with neuroanatomic borders determined by the histological stains: red = mesencephalic reticular formation; pink = ventral tegmental area; dark purple = pedunculotegmental nucleus; turquoise = dorsal raphe; light purple = periaqueductal grey. Figure adapted from Edlow et al. JNEN 2012 (9).

## Supplementary Tables

Table S1. Demographic and clinical characteristics for individuals who donated brain specimens

Specimen ID	Age	Sex	Medical History	Cause of Death	Fresh brain weight*	Post-mortem fixation interval	Post-mortem MRI interval	Type of MRI
Specimen 1	53	F	Pelvic sarcoma (high grade), breast carcinoma (stage 1), deep vein thrombosis, hypertension	Systemic complications of cancer	1250 grams	24 hours	103 days	4.7 Tesla Dissected Specimen
Specimen 2	60	F	Cecal adenocarcinoma (metastatic), deep vein thrombosis, depression	Septic shock	1440 grams	24 hours	719 days	3 Tesla Whole Brain Specimen
Specimen 3	61	F	Ovarian carcinoma (metastatic), hypertension	Septic shock	1305 grams	72 hours	609 days	

\* Normal fresh brain weight = 1200-1500 grams.

**Table S2. Neuroanatomic Localization of Midbrain Arousal Nuclei**

Node	Component Nuclei	Atlas Plates	Rostral Boundary	Caudal Boundary	Ventral Boundary	Dorsal Boundary	Medial Boundary	Lateral Boundary
<b>mRt</b>	CnF, isRt, PrCnF, mRt, CeMe, and p1Rt	8.51 to 8.64	Mesencephalic-diencephalic junction	Ponto-mesencephalic junction	Caudal: CTg and PTg Rostral: CTg and ML	Caudal: IC Rostral: SC	Caudal: DR and PAG Rostral: PAG	Caudal: ML and IC Rostral: ML
<b>VTA</b>	PIF, PN, PBP, VTA, VTAR	8.51 to 8.64	Mesencephalic-diencephalic junction	Ponto-mesencephalic junction	Caudal: Interpeduncular nucleus Rostral: interpeduncular nucleus, fasciculus retroflexus, and interpeduncular fossa	Caudal: Decussation of the superior cerebellar peduncles Rostral: RLi (medially) and red nuclei (laterally)	Caudal: interpeduncular nucleus and caudal linear nucleus of the raphe Rostral: N/A	Caudal: trigeminothalamic tract, medial lemniscus and SN Rostral: SN
<b>PAG</b>	LPAG, DLPAG, DMPAG, PIGI, P1PAG	8.51 to 8.64	mesencephalic-diencephalic junction	Ponto-mesencephalic junction	Caudal: DR Rostral: Rli	Caudal: IC Rostral: SC and Pcomm	N/A	mRt
<b>PTg</b>	PTg, Rls	8.48 to 8.53	mRt (isRt)	PBC (LPBC)	Trigeminothalamic tract and retrorubral field	mRt and spinothalamic tract	Caudal: Decussation of superior cerebellar peduncles Rostral: CTg	Ventral: Trigeminothalamic tract and ML Dorsal: spinothalamic tract
<b>DR</b>	DRC, DRD, DRI, DRL, DRV, PDR	8.37 to 8.56	PAG	Raphe pontis nucleus	Caudal: MnR Rostral: caudal linear nucleus of the raphe	4 <sup>th</sup> ventricle caudally; cerebral aqueduct and PAG rostrally	N/A	Caudal: medial longitudinal fasciculus and LDTg Rostral: mRt and CTg

All anatomic nomenclature, abbreviations, and atlas plates are from Paxinos, G., Huang, X., Sengul, G., & Watson, C. (2012). Organization of Brainstem Nuclei. In J. K. Mai & G. Paxinos (Eds.), *The Human Nervous System* (3rd ed., pp. 260-327). Amsterdam: Elsevier Academic Press. N/A = not applicable. Anatomic abbreviations are provided in the Supplementary Material.

**Table S3. Neuroanatomic Localization of Pontine Arousal Nuclei**

Node	Component Nuclei	Atlas Plates	Rostral Boundary	Caudal Boundary	Ventral Boundary	Dorsal Boundary	Medial Boundary	Lateral Boundary
<b>PnO</b>	PnO	8.37 to 8.50	Ponto-mesencephalic junction	Mid-pons at the pontine reticular nucleus, caudal part	Caudal: B9 serotonin cells, trigeminothalamic tract and ML Rostral: decussation of SCP	Caudal: Dorsomedial tegmental area Rostral: MLF and LDTg	MnR	Caudal: CTg Rostral: CTg and SCP
<b>PBC</b>	MPB, MPBE, LPB, LPBC, LPBD, LPBE, LPBS	8.37 to 8.50	Ponto-mesencephalic junction	Mid-pons at the superior vestibular nucleus	CTg and ventrolateral tegmental area	SCP	* Caudal: LC and subcoeruleus nucleus Rostral: LC, LDTg, and CTg	** Lateral boundary of pons
<b>MnR</b>	MnR, PMnR	8.37 to 8.50	Ponto-mesencephalic junction	Mid-pons at the raphe pontis nucleus	Caudal: reticulotegmental nucleus Rostral: pontine nuclei, B9 serotonin cells, and decussation of the SCP	DR	N/A	PnO
<b>LC</b>	LC	8.37 to 8.50	Ponto-mesencephalic junction	Mid-pons at the superior vestibular nucleus	Caudal: subcoeruleus nucleus, dorsal part Rostral: LDTg	Caudal: central grey of the rhombencephalon Rostral: epicoeruleus nucleus	Caudal: central grey of the rhombencephalon Rostral: LDTg	PBC
<b>LDTg</b>	LDTg, LDTgV	8.41 to 8.50	Ponto-mesencephalic junction	Mid-pons at the central grey of the rhombencephalon	MLF, CTg, and PnO	Central grey of the rhombencephalon and LC	Central grey of the rhombencephalon, MLF, and DR	Caudal: LC and PBC Rostral: LC, PBC, and SCP

All anatomic nomenclature, abbreviations, and atlas plates are from Paxinos, G., Huang, X., Sengul, G., & Watson, C. (2012). Organization of Brainstem Nuclei. In J. K. Mai & G. Paxinos (Eds.), *The Human Nervous System* (3rd ed., pp. 260-327). Amsterdam: Elsevier Academic Press. N/A = not applicable. Anatomic abbreviations are provided in the Supplementary Material. \* For the medial boundary of PBC, we refer to structures on the medial aspect of the medial component of PBC. The medial boundary of the lateral component of PBC is the SCP along its entire rostro-caudal extent. \*\* For the lateral boundary of PBC, we refer to structures on the lateral aspect of the lateral component of PBC. The lateral boundary of the medial component of PBC is the SCP along its entire rostro-caudal extent.



**Table S4. Neuroanatomic Localization of Thalamic Arousal Nuclei**

Node	Component Nuclei	Atlas Plates	Inferior Boundary	Superior Boundary	Anterior Boundary	Posterior Boundary	Medial Boundary	Lateral Boundary
<b>IL</b>	CL, CeM, PC, CD, CM, Pf, SPf, Fa	27 to 57	Centromedian nucleus of the thalamus	Anterior: anteroventral nucleus of the thalamus Posterior: dorsal superficial nucleus (laterodorsal nucleus) of the thalamus	Anterior border of thalamus Fasciculosus nucleus	Pulvinar	Medial dorsal thalamic nucleus	Pulvinar ventral lateral thalamic nucleus posteriorly and ventral anterior thalamic nucleus anteriorly
<b>Ret</b>	Rmc , Rpc	25 to 65	Zona incerta and subthalamic nucleus	Stria terminalis and white matter of the forebrain	Bed nucleus of stria terminalis	Crus of the fornix	Anterior: Ventral anterior nucleus of thalamus Posterior: Ventral lateral nucleus, lateral posterior nucleus, and pulvinar	White matter of the forebrain (internal capsule)
<b>PaV</b>	PaVr, PaVc	27 to 47	Anterior: rhomboid nucleus of thalamus Posterior: periventricular area of thalamus, intermediodorsal nucleus of thalamus, and intralaminar nuclei	Stria medullaris and velum interpositum	Supraoptic region of hypothalamus and fornix	Periventricular area of thalamus	Third ventricle	Anterior: fasciculosus nucleus of thalamus and anteromedial nucleus of thalamus Posterior: mediodorsal nucleus and intralaminar nuclei

All anatomic nomenclature, abbreviations, and atlas plates are from Ding, S.L. et al. (2016). Comprehensive cellular-resolution atlas of the adult human brain. *J Comp Neurol* **524** (16): 3127-3481. Anatomic abbreviations are provided in the Supplementary Material.

**Table S5. Neuroanatomic Localization of Hypothalamic Arousal Nuclei**

Node	Component Nuclei	Atlas Plates	Inferior Boundary	Superior Boundary	Anterior Boundary	Posterior Boundary	Medial Boundary	Lateral Boundary
<b>TMN</b>	TMN	34* to 40	Lateral tuberal nuclei and medial mammillary nucleus	Lateral hypothalamic area and substantia nigra, reticular part	Lateral hypothalamic area	Lateral hypothalamic area and retromammillary area	Anterior: lateral hypothalamic area and fornix Posterior: medial mammillary nucleus	Anterior: optic tract Posterior: substantia nigra, reticular part
<b>LHA</b>	LHAa**, LHAp, LHAtub	27 to 42	Anterior: optic tracts, supraoptic nucleus, retrochiasmatic nucleus, and interpeduncular cistern Posterior: TM and mammillary bodies	Anterior: dorsomedial hypothalamic nucleus, tuberal region of hypothalamus, and fornix Posterior: ventral anterior nucleus of thalamus, mammillo-tegmental tract and zona incerta	Preoptic region of hypothalamus	Midbrain	Anterior: tuberal region of hypothalamus Posterior: mammillary region of hypothalamus, mammillothalamic tract	Anterior: BNM/SI, forebrain white matter Posterior: Subthalamic nucleus and substantia nigra reticular part
<b>SUM</b>	SUM	35 to 40	Mammillary body and mammillothalamic tract	Posterior hypothalamic nucleus	Posterior hypothalamic nucleus and mammillary peduncle	Posterior hypothalamic nucleus	Posterior hypothalamic nucleus	Anterior: LHA Posterior: TMN and mammillary body

All anatomic nomenclature, abbreviations, and atlas plates are from Ding, S.L. et al. (2016). Comprehensive cellular-resolution atlas of the adult human brain. *J Comp Neurol* **524** (16): 3127-3481. N/A = not applicable. Anatomic abbreviations are provided in the Supplementary Material.

\* From plates 29 to 33, TM is fully enveloped within LHA and cannot be reliably distinguished from LHA. Therefore, we operationally define the anterior boundary of the TM node at plate 34. \*\* LHAa is not depicted in the Ding atlas.

**Table S6. Neuroanatomic Localization of Basal Forebrain Arousal Nuclei**

Node	Component Nuclei	Atlas Plates	Inferior Boundary	Superior Boundary	Anterior Boundary	Posterior Boundary	Medial Boundary	Lateral Boundary
<b>DBB</b>	NDBv, NDBh, dib	19 to 23	Anterior: subgenual division of anterior cingulate cortex Posterior: basal cisterns	Anterior: medial septal nucleus Posterior: preoptic region of hypothalamus	subgenual division of anterior cingulate cortex	Preoptic region of hypothalamus	Anterior: basal cisterns Posterior: preoptic region of hypothalamus	Anterior: septal nuclei Posterior: NBM/SI
<b>BNM/SI</b>	BNMI, BNMm, SI-pc, SI-nc	19 to 45	Anterior: forebrain white matter, subgenual division of anterior cingulate cortex Middle: basal cisterns Posterior: amygdaloid complex	Anterior: ventral pallidus, olfactory tubercle Middle: sublenticular extended amygdala, anterior commissure Posterior: globus pallidus	Olfactory tubercle, forebrain white matter	Optic tract, amygdaloid complex, forebrain white matter,	Anterior: diagonal band Middle: LHA Posterior: optic tract	Anterior: lateral olfactory area Middle: putamen, anterior commissure Posterior: amygdalostratial transition area

All anatomic nomenclature, abbreviations, and atlas plates are from Ding, S.L. et al. (2016). Comprehensive cellular-resolution atlas of the adult human brain. *J Comp Neurol* **524** (16): 3127-3481. Anatomic abbreviations are provided in the Supplementary Material.

**Table S7. Interspecimen Variance in Brainstem-Thalamic Projection Connectivity Probabilities**

Nodes	IL			PaV			Ret		
	S2	S3	Mean	S2	S3	Mean	S2	S3	Mean
<b>mRt</b>	0.60	3.05	1.82	0.4	3.07	1.72	1.94	3.96	2.95
<b>VTA</b>	0.03	0.70	0.36	0	0.75	0.39	<b>0.09</b>	0.80	<b>0.44</b>
<b>PAG</b>	0.25	3.26	1.75	1.7	6.33	4.02	2.14	0.67	1.40
<b>PTg</b>	0.02	0.72	0.37	0	0.80	0.40	0.04	0.47	0.26
<b>DR</b>	0.001	0.16	0.08	0	0.08	0.04	0.002	0.20	0.10
<b>PnO</b>	0	0.10	0.05	<b>0</b>	0.003	<b>0.001</b>	0	0.34	0.17
<b>PBC</b>	0	0.25	0.13	<b>0</b>	<b>0.01</b>	<b>0.003</b>	0	0.49	0.25
<b>MnR</b>	<b>0</b>	0.11	<b>0.05</b>	<b>0</b>	<b>0.003</b>	<b>0.001</b>	<b>0</b>	0.3	<b>0.15</b>
<b>LC</b>	<b>0</b>	0.10	<b>0.05</b>	<b>0</b>	0.003	<b>0.002</b>	<b>0</b>	0.1	<b>0.05</b>
<b>LDTg</b>	<b>0</b>	0.07	<b>0.04</b>	<b>0</b>	0.002	<b>0.001</b>	<b>0</b>	0.10	<b>0.05</b>

All connectivity probability measurements are multiplied by 100 and reported as percentages. Anatomic abbreviations are provided in the Supplementary Material. Highlighted in **RED** are connections that failed that confidence interval test. S2 = Specimen 2; S3 = Specimen 3.

**Table S8. Interspecimen Variance in Brainstem-Hypothalamic Projection Connectivity Probabilities**

Nodes	TM			LHA			SUM		
	S2	S3	Mean	S2	S3	Mean	S2	S3	Mean
<b>mRt</b>	1.15	1.47	1.31	3.79	3.48	3.64	0.76	0.93	0.85
<b>VTA</b>	10.20	18.71	14.45	22.57	24.29	23.43	7.85	23.48	15.66
<b>PAG</b>	0.55	2.82	1.69	3.02	2.74	2.88	0.43	2.39	1.41
<b>PTg</b>	9.96	9.57	9.77	9.98	13.48	11.73	5.89	8.88	7.36
<b>DR</b>	1.49	3.76	2.62	2.80	2.79	2.79	1.43	4.47	2.95
<b>PnO</b>	1.84	1.70	1.77	2.57	1.61	2.09	1.37	2.85	2.11
<b>PBC</b>	3.99	4.05	4.02	4.20	4.73	4.46	3.17	3.77	3.47
<b>MnR</b>	0.94	1.01	0.98	1.07	0.71	0.89	1.10	2.01	1.55
<b>LC</b>	0.88	1.91	1.39	1.45	2.81	2.13	1.05	2.44	1.74
<b>LDTg</b>	0.36	1.36	0.86	0.75	1.96	1.36	0.56	2.26	1.41

All connectivity probability measurements are multiplied by 100 and reported as percentages. Anatomic abbreviations are provided in the Supplementary Material. Highlighted in **RED** are connections that failed that confidence interval test. S2 = Specimen 2; S3 = Specimen 3.

**Table S9. Interspecimen Variance in Brainstem-Basal Forebrain Projection Connectivity Probabilities**

Nodes	DBB			BNM/SI		
	S2	S3	Mean	S2	S3	Mean
<b>mRt</b>	0.03	0.07	0.05	1.23	1.52	1.37
<b>VTA</b>	0.08	0.006	0.04	6.61	10.93	8.77
<b>PAG</b>	0.07	0.06	0.07	1.01	0.92	0.96
<b>PTg</b>	0.01	0.01	0.01	1.91	6.78	4.35
<b>DR</b>	0.04	0.04	0.04	0.80	1.12	0.96
<b>PnO</b>	0.003	0.001	0.002	0.71	0.72	0.71
<b>PBC</b>	0.009	0.006	0.007	0.95	2.22	1.58
<b>MnR</b>	0.002	0.001	0.001	0.29	0.35	0.32
<b>LC</b>	0.01	0.02	0.01	0.42	1.32	0.87
<b>LDTg</b>	0.005	0.006	0.006	0.22	0.97	0.59

All connectivity probability measurements are multiplied by 100 and reported as percentages. Anatomic abbreviations are provided in the Supplementary Material. Highlighted in **RED** are connections that failed that confidence interval test. S2 = Specimen 2; S3 = Specimen 3.

**Table S10. Interspecimen Variance in Brainstem-DMN Projection Connectivity Probabilities**

Nodes	PMC			MPFC			IPL			LT			MT		
	S2	S3	Mean	S2	S3	Mean	S2	S3	Mean	S2	S3	Mean	S2	S3	Mean
<b>mRt</b>	0.59	0.14	0.37	0.1	0.007	0.04	0.01	0.03	0.02	0	0.01	0.004	0.24	1.34	0.79
<b>VTA</b>	0.24	0.22	0.23	0.1	0.004	0.04	0.002	0.02	0.01	0	0.01	0.002	0.01	0.47	0.24
<b>PAG</b>	0.93	0.29	0.61	0.1	0.006	0.05	0.01	0.03	0.02	0	0.004	0.002	0.21	0.03	0.12
<b>PTg</b>	0.22	0.07	0.15	0	0.002	0.006	0	0.007	0.004	0	0.01	0.003	0	0.83	0.42
<b>DR</b>	0.16	0.18	0.17	0.1	0.003	0.04	0	0.02	0.008	0	0.01	0.005	0	2.03	1.02
<b>PnO</b>	0.001	0.06	0.03	0	0.005	0.003	0	0.03	0.01	0	0.01	0.006	0	6.21	3.11
<b>PBC</b>	0	0.01	0.006	0	0.001	0.001	0	0.03	0.01	0	0.02	0.01	0	8.66	4.33
<b>MnR</b>	0	0.01	0.007	0	0.004	0.002	0	0.01	0.01	0	0.01	0.005	0	6.15	3.08
<b>LC</b>	0	0.002	0.001	0	0	0.0	0	0.003	0.002	0	0.005	0.002	0	1.36	0.68
<b>LDTg</b>	0	0.001	0.001	0	0	0.0	0	0.003	0.002	0	0.004	0.002	0	1.30	0.65

All connectivity probability measurements are multiplied by 100 and reported as percentages. Anatomic abbreviations are provided in the Supplementary Material. Highlighted in RED are connections that failed that confidence interval test. S2 = Specimen 2; S3 = Specimen 3.

**Table S11. Interspecimen Variance in Left-Sided Association Connectivity Probabilities**

Nodes	mRt_L			PTg_L			PnO_L			PBC_L			LC_L			LDTg_L		
	S2	S3	Mean	S2	S3	Mean	S2	S3	Mean	S2	S3	Mean	S2	S3	Mean	S2	S3	Mean
mRt_L				23.00	19.36	21.01	0.42	0.01	0.21	0.35	0.03	0.19	0.10	0.72	0.41	0.06	0.11	0.08
PTg_L	22.67	19.36	21.01				1.57	0.05	0.81	1.53	3.47	2.50	0.93	0.04	0.49	0.46	0.02	0.24
PnO_L	0.42	0.01	0.21	1.60	0.05	0.81				27.60	40.93	34.26	18.47	3.34	10.90	14.40	1.93	8.16
PBC_L	0.35	0.03	0.19	1.50	3.47	2.50	27.60	40.93	34.26				17.57	30.81	24.19	6.21	28.30	17.26
LC_L	0.10	0.72	0.41	0.90	0.04	0.49	18.47	3.34	10.90	17.57	30.81	24.19				52.00	58.09	55.05
LDTg_L	0.06	0.11	0.08	0.50	0.02	0.24	14.40	1.93	8.16	6.21	28.30	17.26	52.00	58.09	55.05			

All connectivity probability measurements are multiplied by 100 and reported as percentages. Anatomic abbreviations are provided in the Supplementary Material. Highlighted in **RED** are connections that failed that confidence interval test. S2 = Specimen 2; S3 = Specimen 3.



**Table S12. Interspecimen Variance in Right-Sided Association Connectivity Probabilities**

Nodes	mRt_R			PTg_R			PnO_R			PBC_R			LC_R			LDTg_R		
	S2	S3	Mean	S2	S3	Mean	S2	S3	Mean	S2	S3	Mean	S2	S3	Mean	S2	S3	Mean
mRt_R				7.52	21.34	14.43	3.35	0.17	1.76	24.88	17.93	21.41	28.29	27.89	28.09	11.23	5.28	8.25
PTg_R	7.52	21.34	14.43				2.81	0.75	1.78	45.81	58.66	52.23	2.12	3.41	2.76	0.65	0.17	0.41
PnO_R	3.35	0.17	1.76	2.81	0.75	1.78				2.94	2.44	2.69	1.43	3.43	2.43	2.21	1.65	1.93
PBC_R	24.88	17.93	21.41	45.81	58.66	52.23	2.94	2.44	2.69				17.86	6.80	12.33	0.68	0.26	0.47
LC_R	28.29	27.89	28.09	2.12	3.41	2.76	1.431	3.43	2.43	17.86	6.80	12.33				50.79	31.60	41.19
LDTg_R	11.23	5.28	8.25	0.65	0.17	0.41	2.21	1.65	1.93	0.68	0.26	0.47	50.79	31.60	41.19			

All connectivity probability measurements are multiplied by 100 and reported as percentages. Anatomic abbreviations are provided in the Supplementary Material. Highlighted in RED are connections that failed that confidence interval test. S2 = Specimen 2; S3 = Specimen 3.

**Table S13. Interspecimen Variance in Midline Association Connectivity Probabilities**

Nodes	VTA			PAG			DR			MnR		
	S2	S3	Mean	S2	S3	Mean	S2	S3	Mean	S2	S3	Mean
mRt_L	16.29	13.77	15.03	50.00	9.37	29.83	10.20	3.99	7.09	0.66	0.01	0.33
PTg_L	3.72	1.95	2.84	4.60	0.62	2.63	2.19	0.07	1.13	2.55	0.02	1.29
PnO_L	4.49	0.02	2.25	0.10	0.01	0.07	8.66	6.51	7.58	62.61	68.11	65.36
PBC_L	0.10	0.03	0.07	0	0.01	0.01	3.38	20.34	11.86	22.09	36.38	29.23
LC_L	0.25	0.02	0.13	0	0.03	0.02	8.85	18.12	13.49	25.24	5.98	15.61
LDTg_L	0.26	0.01	0.13	0	0.01	0.01	6.56	12.25	9.41	21.65	4.60	13.13
mRt_R	9.42	13.86	11.64	50.00	20.35	35.29	10.00	5.79	7.90	0.14	0.01	0.07
PTg_R	7.89	8.06	7.98	1.10	8.75	4.91	1.25	2.80	2.02	0.25	0.02	0.14
PnO_R	6.06	0.01	3.04	0.50	0.01	0.27	19.05	7.48	13.26	64.63	64.02	64.32
PBC_R	2.58	0.21	1.40	0.50	0.45	0.47	8.42	15.38	11.90	7.33	49.39	28.36
LC_R	1.30	0.12	0.71	0.30	0.02	0.14	14.03	18.80	16.42	8.81	0.91	4.86
LDTg_R	0.58	0.01	0.30	0.10	0.01	0.04	8.42	15.82	12.12	4.64	1.31	2.98
VTA				14.06	34.95	24.51	27.28	17.34	22.31	6.69	0.01	3.35
PAG	14.06	34.95	24.51				26.83	26.44	26.63	0.27	0.01	0.14
DR	27.28	17.34	22.31	26.83	26.44	26.63				19.63	13.34	16.49
MnR	6.69	0.01	3.35	0.27	0.01	0.14	19.63	13.34	16.49			

All connectivity probability measurements are multiplied by 100 and reported as percentages. Anatomic abbreviations are provided in the Supplementary Material. Highlighted in RED are connections that failed that confidence interval test. S2 = Specimen 2; S3 = Specimen 3.

**Table S14. Interspecimen Variance in Commissural Connectivity Probabilities**

Nodes	mRt_R			PTg_R			PnO_R			PBC_R			LC_R			LDTg_R		
	S2	S3	Mean	S2	S3	Mean	S2	S3	Mean	S2	S3	Mean	S2	S3	Mean	S2	S3	Mean
mRt_L	35.25	0.21	17.73	0.70	0.11	0.41	0.78	0.01	0.40	0.17	0.01	0.09	0.32	0.004	0.16	0.05	0.003	0.02
PTg_L	4.28	0.13	2.20	3.90	0.14	2.03	2.29	0.02	1.16	0.62	0.03	0.33	1.46	0.01	0.74	0.20	0.02	0.11
PnO_L	0.04	0.02	0.03	0.10	0.04	0.06	33.46	59.52	46.49	3.23	49.19	26.21	4.45	1.02	2.73	2.33	1.25	1.79
PBC_L	0.01	0.01	0.01	0	0.06	0.03	9.45	31.87	20.66	0.10	48.70	24.40	0.55	25.48	13.01	0.13	27.30	13.72
LC_L	0.01	0.01	0.01	0	0.03	0.02	20.60	2.56	11.58	0.38	23.72	12.05	3.35	30.35	16.85	1.02	38.11	19.56
LDTg_L	0.01	0.002	0.004	0	0.01	0.01	18.68	2.03	10.35	0.49	17.32	8.91	3.47	25.04	14.26	2.25	43.88	23.07

All connectivity probability measurements are multiplied by 100 and reported as percentages. Anatomic abbreviations are provided in the Supplementary Material. Highlighted in RED are connections that failed that confidence interval test. S2 = Specimen 2; S3 = Specimen 3.

## REFERENCES

1. B. L. Edlow, J. Claassen, N. D. Schiff, D. M. Greer, Recovery from disorders of consciousness: mechanisms, prognosis and emerging therapies. *Nat Rev Neurol* **17**, 135–156 (2021).
2. R. L. Buckner, L. M. DiNicola, The brains default network: updated anatomy, physiology and evolving insights. *Nat Rev Neurosci* **20**, 593–608 (2019).
3. E. N. Brown, R. Lydic, N. D. Schiff, General anesthesia, sleep, and coma. *N Engl J Med* **363**, 2638–2650 (2010).
4. C. Koch, M. Massimini, M. Boly, G. Tononi, Neural correlates of consciousness: progress and problems. *Nat Rev Neurosci* **17**, 307–321 (2016).
5. H. C. Kinney, J. Korein, A. Panigrahy, P. Dikkes, R. Goode, Neuropathological findings in the brain of Karen Ann Quinlan. The role of the thalamus in the persistent vegetative state. *N Engl J Med* **330**, 1469–1475 (1994).
6. P. Fuller, D. Sherman, N. P. Pedersen, C. B. Saper, J. Lu, Reassessment of the structural basis of the ascending arousal system. *J Comp Neurol* **519**, 933–956 (2011).
7. N. P. Pedersen, L. Ferrari, A. Venner, J. L. Wang, S. B. G. Abbott, N. Vujovic, E. Arrigoni, C. B. Saper, P. M. Fuller, Supramammillary glutamate neurons are a key node of the arousal system. *Nat Commun* **8**, 1405 (2017).
8. P. Pais-Roldan, B. L. Edlow, Y. Jiang, J. Stelzer, M. Zou, X. Yu, Multimodal assessment of recovery from coma in a rat model of diffuse brainstem tegmentum injury. *NeuroImage* **189**, 615–630 (2019).
9. B. L. Edlow, E. Takahashi, O. Wu, T. Benner, G. Dai, L. Bu, P. E. Grant, D. M. Greer, S. M. Greenberg, H. C. Kinney, R. D. Folkerth, Neuroanatomic connectivity of the human ascending arousal system critical to consciousness and its disorders. *J Neuropathol Exp Neurol* **71**, 531–546 (2012).
10. T. E. Scammell, E. Arrigoni, J. O. Lipton, Neural Circuitry of Wakefulness and Sleep. *Neuron* **93**, 747–765 (2017).
11. M. Boly, M. Massimini, N. Tsuchiya, B. R. Postle, C. Koch, G. Tononi, Are the Neural Correlates of Consciousness in the Front or in the Back of the Cerebral Cortex? Clinical and Neuroimaging Evidence. *J Neurosci* **37**, 9603–9613 (2017).
12. A. Demertzi, E. Tagliazucchi, S. Dehaene, G. Deco, P. Barttfeld, F. Raimondo, C. Martial, D. Fernandez-Espejo, B. Rohaut, H. U. Voss, N. D. Schiff, A. M. Owen, S. Laureys, L. Naccache, J. D. Sitt, Human consciousness is supported by dynamic complex patterns of brain signal coordination. *Sci Adv* **5**, eaat7603 (2019).

13. G. Moruzzi, H. W. Magoun, Brain stem reticular formation and activation of the EEG. *Electroencephalogr Clin Neurophysiol* **1**, 455–473 (1949).
14. P. G. Samann, R. Wehrle, D. Hoehn, V. I. Spoormaker, H. Peters, C. Tully, F. Holsboer, M. Czisch, Development of the brains default mode network from wakefulness to slow wave sleep. *Cereb Cortex* **21**, 2082–2093 (2011).
15. S. Silva, X. Alacoque, O. Fourcade, K. Samii, P. Marque, R. Woods, J. Mazziotta, F. Chollet, I. Loubinoux, Wakefulness and loss of awareness: brain and brainstem interaction in the vegetative state. *Neurology* **74**, 313–320 (2010).
16. K. Solt, C. J. Van Dort, J. J. Chemali, N. E. Taylor, J. D. Kenny, E. N. Brown, Electrical stimulation of the ventral tegmental area induces reanimation from general anesthesia. *Anesthesiology* **121**, 311–319 (2014).
17. L. R. B. Spindler, A. I. Luppi, R. M. Adapa, M. M. Craig, P. Coppola, A. R. D. Peattie, A. E. Manktelow, P. Finoia, B. J. Sahakian, G. B. Williams, J. Allanson, J. D. Pickard, D. K. Menon, E. A. Stamatakis, Dopaminergic brainstem disconnection is common to pharmacological and pathological consciousness perturbation. *Proc Natl Acad Sci U S A* **118**, (2021).
18. N. E. Taylor, C. J. Van Dort, J. D. Kenny, J. Pei, J. A. Guidera, K. Y. Vlasov, J. T. Lee, E. S. Boyden, E. N. Brown, K. Solt, Optogenetic activation of dopamine neurons in the ventral tegmental area induces reanimation from general anesthesia. *Proc Natl Acad Sci USA*, (2016).
19. A. Eban–Rothschild, G. Rothschild, W. J. Giardino, J. R. Jones, L. de Lecea, VTA dopaminergic neurons regulate ethologically relevant sleep–wake behaviors. *Nat Neurosci* **19**, 1356–1366 (2016).
20. L. de Lecea, T. S. Kilduff, C. Peyron, X. Gao, P. E. Foye, P. E. Danielson, C. Fukuhara, E. L. Battenberg, V. T. Gautvik, F. S. Bartlett, 2nd, W. N. Frankel, A. N. van den Pol, F. E. Bloom, K. M. Gautvik, J. G. Sutcliffe, The hypocretins: hypothalamus–specific peptides with neuroexcitatory activity. *Proc Natl Acad Sci U S A* **95**, 322–327 (1998).
21. G. Aston–Jones, S. Chen, Y. Zhu, M. L. Oshinsky, A neural circuit for circadian regulation of arousal. *Nat Neurosci* **4**, 732–738 (2001).
22. L. L. Glenn, M. Steriade, Discharge rate and excitability of cortically projecting intralaminar thalamic neurons during waking and sleep states. *J Neurosci* **2**, 1387–1404 (1982).
23. N. D. Schiff, J. T. Giacino, K. Kalmar, J. D. Victor, K. Baker, M. Gerber, B. Fritz, B. Eisenberg, T. Biondi, J. OConnor, E. J. Kobylarz, S. Farris, A. Machado, C. McCagg, F. Plum, J. J. Fins, A. R. Rezai, Behavioural improvements with thalamic stimulation after severe traumatic brain injury. *Nature* **448**, 600–603 (2007).

24. G. Buzsaki, R. G. Bickford, G. Ponomareff, L. J. Thal, R. Mandel, F. H. Gage, Nucleus basalis and thalamic control of neocortical activity in the freely moving rat. *J Neurosci* **8**, 4007–4026 (1988).
25. M. Xu, S. Chung, S. Zhang, P. Zhong, C. Ma, W. C. Chang, B. Weissbourd, N. Sakai, L. Luo, S. Nishino, Y. Dan, Basal forebrain circuit for sleep–wake control. *Nat Neurosci* **18**, 1641–1647 (2015).
26. J. A. Hobson, R. W. McCarley, P. W. Wyzinski, Sleep cycle oscillation: reciprocal discharge by two brainstem neuronal groups. *Science* **189**, 55–58 (1975).
27. M. E. Trulson, B. L. Jacobs, Raphe unit activity in freely moving cats: correlation with level of behavioral arousal. *Brain research* **163**, 135–150 (1979).
28. G. Buzsaki, *Rhythms of the Brain*. (Oxford University Press, New York, 2006).
29. J. Smallwood, A. Turnbull, H. T. Wang, N. S. P. Ho, G. L. Poerio, T. Karapanagiotidis, D. Konu, B. McKeown, M. Zhang, C. Murphy, D. Vatansever, D. Bzdok, M. Konishi, R. Leech, P. Seli, J. W. Schooler, B. Bernhardt, D. S. Margulies, E. Jefferies, The neural correlates of ongoing conscious thought. *iScience* **24**, 102132 (2021).
30. Y. G. Bodien, C. Chatelle, B. L. Edlow, Functional Networks in Disorders of Consciousness. *Semin Neurol* **37**, 485–502 (2017).
31. M. Steriade, G. Buzsaki, in *Brain Cholinergic Systems*, M. Steriade, D. Biesold, Eds. (Oxford University Press, New York, NY, 1990), pp. 3–64.
32. M. F. Mason, M. I. Norton, J. D. Van Horn, D. M. Wegner, S. T. Grafton, C. N. Macrae, Wandering minds: the default network and stimulus–independent thought. *Science* **315**, 393–395 (2007).
33. M. Steriade, S. Datta, D. Pare, G. Oakson, R. C. Curro Dossi, Neuronal activities in brain–stem cholinergic nuclei related to tonic activation processes in thalamocortical systems. *J Neurosci* **10**, 2541–2559 (1990).
34. S. M. Smith, C. F. Beckmann, J. Andersson, E. J. Auerbach, J. Bijsterbosch, G. Douaud, E. Duff, D. A. Feinberg, L. Griffanti, M. P. Harms, M. Kelly, T. Laumann, K. L. Miller, S. Moeller, S. Petersen, J. Power, G. Salimi–Khorshidi, A. Z. Snyder, A. T. Vu, M. W. Woolrich, J. Xu, E. Yacoub, K. Ugurbil, D. C. Van Essen, M. F. Glasser, W. U.–M. H. Consortium, Resting–state fMRI in the Human Connectome Project. *NeuroImage* **80**, 144–168 (2013).
35. M. Steriade, G. Oakson, N. Ropert, Firing rates and patterns of midbrain reticular neurons during steady and transitional states of the sleep–waking cycle. *Experimental brain research. Experimentelle Hirnforschung. Experimentation cerebrale* **46**, 37–51 (1982).

36. J. Lu, T. C. Jhou, C. B. Saper, Identification of wake-active dopaminergic neurons in the ventral periaqueductal gray matter. *J Neurosci* **26**, 193–202 (2006).
37. D. J. McGinty, R. M. Harper, Dorsal raphe neurons: depression of firing during sleep in cats. *Brain research* **101**, 569–575 (1976).
38. M. C. Xi, F. R. Morales, M. H. Chase, Interactions between GABAergic and cholinergic processes in the nucleus pontis oralis: neuronal mechanisms controlling active (rapid eye movement) sleep and wakefulness. *J Neurosci* **24**, 10670–10678 (2004).
39. M. H. Qiu, M. C. Chen, P. M. Fuller, J. Lu, Stimulation of the Pontine Parabrachial Nucleus Promotes Wakefulness via Extra-thalamic Forebrain Circuit Nodes. *Curr Biol* **26**, 2301–2312 (2016).
40. M. E. Trulson, T. Crisp, V. M. Trulson, Activity of serotonin-containing nucleus centralis superior (Raphe medianus) neurons in freely moving cats. *Experimental brain research. Experimentelle Hirnforschung. Experimentation cerebrale* **54**, 33–44 (1984).
41. G. Aston-Jones, F. E. Bloom, Activity of norepinephrine-containing locus coeruleus neurons in behaving rats anticipates fluctuations in the sleep-waking cycle. *J Neurosci* **1**, 876–886 (1981).
42. K. Takahashi, J. S. Lin, K. Sakai, Neuronal activity of histaminergic tuberomammillary neurons during wake-sleep states in the mouse. *J Neurosci* **26**, 10292–10298 (2006).
43. M. N. Alam, H. Gong, T. Alam, R. Jaganath, D. McGinty, R. Szymusiak, Sleep-waking discharge patterns of neurons recorded in the rat perifornical lateral hypothalamic area. *The Journal of physiology* **538**, 619–631 (2002).
44. M. Steriade, L. Domich, G. Oakson, Reticularis thalami neurons revisited: activity changes during shifts in states of vigilance. *J Neurosci* **6**, 68–81 (1986).
45. C. M. Novak, A. A. Nunez, Daily rhythms in Fos activity in the rat ventrolateral preoptic area and midline thalamic nuclei. *The American journal of physiology* **275**, R1620–1626 (1998).
46. R. Szymusiak, D. McGinty, Sleep-related neuronal discharge in the basal forebrain of cats. *Brain research* **370**, 82–92 (1986).
47. J. A. McNab, S. Jbabdi, S. C. Deoni, G. Douaud, T. E. Behrens, K. L. Miller, High resolution diffusion-weighted imaging in fixed human brain using diffusion-weighted steady state free precession. *NeuroImage* **46**, 775–785 (2009).
48. G. Paxinos, H. Xu-Feng, G. Sengul, C. Watson, in *The Human Nervous System*, J. K. Mai, G. Paxinos, Eds. (Elsevier, Amsterdam, 2011).

49. S. L. Ding, J. J. Royall, S. M. Sunkin, L. Ng, B. A. Facer, P. Lesnar, A. Guillozet–Bongaarts, B. McMurray, A. Szafer, T. A. Dolbeare, A. Stevens, L. Tirrell, T. Benner, S. Caldejon, R. A. Dalley, N. Dee, C. Lau, J. Nyhus, M. Reding, Z. L. Riley, D. Sandman, E. Shen, A. van der Kouwe, A. Varjabedian, M. Wright, L. Zollei, C. Dang, J. A. Knowles, C. Koch, J. W. Phillips, N. Sestan, P. Wohnoutka, H. R. Zielke, J. G. Hohmann, A. R. Jones, A. Bernard, M. J. Hawrylycz, P. R. Hof, B. Fischl, E. S. Lein, Comprehensive cellular–resolution atlas of the adult human brain. *J Comp Neurol* **524**, 3127–3481 (2016).
50. J. Olszewski, D. Baxter, *Cytoarchitecture of the human brainstem*. (Karger, Basel, Switzerland, ed. 2nd, 1982).
51. G. Paxinos, X. Huang, G. Sengul, C. Watson, in *The Human Nervous System*, J. K. Mai, G. Paxinos, Eds. (Elsevier Academic Press, Amsterdam, 2012), pp. 260–327.
52. S. L. Ding, J. J. Royall, S. M. Sunkin, L. Ng, B. A. Facer, P. Lesnar, A. Guillozet–Bongaarts, B. McMurray, A. Szafer, T. A. Dolbeare, A. Stevens, L. Tirrell, T. Benner, S. Caldejon, R. A. Dalley, N. Dee, C. Lau, J. Nyhus, M. Reding, Z. L. Riley, D. Sandman, E. Shen, A. van der Kouwe, A. Varjabedian, M. Write, L. Zollei, C. Dang, J. A. Knowles, C. Koch, J. W. Phillips, N. Sestan, P. Wohnoutka, H. R. Zielke, J. G. Hohmann, A. R. Jones, A. Bernard, M. J. Hawrylycz, P. R. Hof, B. Fischl, E. S. Lein, Comprehensive cellular–resolution atlas of the adult human brain. *J Comp Neurol* **524**, 3127–3481 (2016).
53. R. P. Vertes, G. F. Martin, Autoradiographic analysis of ascending projections from the pontine and mesencephalic reticular formation and the median raphe nucleus in the rat. *J Comp Neurol* **275**, 511–541 (1988).
54. B. L. Edlow, J. A. McNab, T. Witzel, H. C. Kinney, The Structural Connectome of the Human Central Homeostatic Network. *Brain Connect* **6**, 187–200 (2016).
55. J. D. Schmahmann, D. N. Pandya, *Fiber Pathways of the Brain*. (Oxford University Press, New York, 2006).
56. D. C. Van Essen, K. Ugurbil, E. Auerbach, D. Barch, T. E. Behrens, R. Bucholz, A. Chang, L. Chen, M. Corbetta, S. W. Curtiss, S. Della Penna, D. Feinberg, M. F. Glasser, N. Harel, A. C. Heath, L. Larson–Prior, D. Marcus, G. Michalareas, S. Moeller, R. Oostenveld, S. E. Petersen, F. Prior, B. L. Schlaggar, S. M. Smith, A. Z. Snyder, J. Xu, E. Yacoub, W. U.–M. H. Consortium, The Human Connectome Project: a data acquisition perspective. *NeuroImage* **62**, 2222–2231 (2012).
57. J. E. Iglesias, R. Insausti, G. Lerma–Usabiaga, M. Bocchetta, K. Van Leemput, D. N. Greve, A. van der Kouwe, I. Alzheimers Disease Neuroimaging, B. Fischl, C.



- Caballero–Gaudes, P. M. Paz–Alonso, A probabilistic atlas of the human thalamic nuclei combining ex vivo MRI and histology. *NeuroImage* **183**, 314–326 (2018).
58. C. Neudorfer, J. Germann, G. J. B. Elias, R. Gramer, A. Boutet, A. M. Lozano, A high–resolution in vivo magnetic resonance imaging atlas of the human hypothalamic region. *Sci Data* **7**, 305 (2020).
59. C. J. Chu, N. Tanaka, J. Diaz, B. L. Edlow, O. Wu, M. Hamalainen, S. Stufflebeam, S. S. Cash, M. A. Kramer, EEG functional connectivity is partially predicted by underlying white matter connectivity. *NeuroImage*, (2014).
60. A. Horn, D. Ostwald, M. Reisert, F. Blankenburg, The structural–functional connectome and the default mode network of the human brain. *NeuroImage* **102 Pt 1**, 142–151 (2014).
61. L. R. B. Spindler, A. I. Luppi, R. Adapa, M. C. Craig, P. Coppola, A. R. D. Peattie, A. J. Manktelow, P. Finoia, B. J. Sahakian, G. B. Williams, J. Allanson, J. D. Pickard, D. K. Menon, E. A. Stamatakis, Where does it stem from: Dopaminergic brainstem disconnection is common to pharmacological and pathological consciousness perturbation. *Proc Natl Acad Sci U S A*, (2021).
62. M. Morales, E. B. Margolis, Ventral tegmental area: cellular heterogeneity, connectivity and behaviour. *Nat Rev Neurosci* **18**, 73–85 (2017).
63. K. Solt, J. F. Cotten, A. Cimenser, K. F. Wong, J. J. Chemali, E. N. Brown, Methylphenidate actively induces emergence from general anesthesia. *Anesthesiology* **115**, 791–803 (2011).
64. J. D. Kenny, N. E. Taylor, E. N. Brown, K. Solt, Dextroamphetamine (but Not Atomoxetine) Induces Reanimation from General Anesthesia: Implications for the Roles of Dopamine and Norepinephrine in Active Emergence. *PLoS one* **10**, e0131914 (2015).
65. Y. Oishi, Y. Suzuki, K. Takahashi, T. Yonezawa, T. Kanda, Y. Takata, Y. Cherasse, M. Lazarus, Activation of ventral tegmental area dopamine neurons produces wakefulness through dopamine D2–like receptors in mice. *Brain Struct Funct* **222**, 2907–2915 (2017).
66. R. D. Palmiter, Dopamine signaling as a neural correlate of consciousness. *Neuroscience* **198**, 213–220 (2011).
67. B. L. Edlow, Dopaminergic modulation of human consciousness via default mode network connectivity. *Proc Natl Acad Sci U S A* **118**, (2021).
68. M. E. Barra, B. L. Edlow, G. M. Brophy, Pharmacologic Therapies to Promote Recovery of Consciousness. *Semin Neurol* **42**, 335–347 (2022).

69. B. L. Edlow, M. E. Barra, D. W. Zhou, A. S. Foulkes, S. B. Snider, Z. D. Threlkeld, S. Chakravarty, J. E. Kirsch, S. T. Chan, S. L. Meisler, T. P. Bleck, J. J. Fins, J. T. Giacino, L. R. Hochberg, K. Solt, E. N. Brown, Y. G. Bodien, Personalized Connectome Mapping to Guide Targeted Therapy and Promote Recovery of Consciousness in the Intensive Care Unit. *Neurocrit Care* **33**, 364–375 (2020).
70. P. O. Jenkins, S. De Simoni, N. J. Bourke, J. Fleminger, G. Scott, D. J. Towey, W. Svensson, S. Khan, M. C. Patel, R. Greenwood, D. Friedland, A. Hampshire, J. H. Cole, D. J. Sharp, Stratifying drug treatment of cognitive impairments after traumatic brain injury using neuroimaging. *Brain* **142**, 2367–2379 (2019).
71. E. A. Fridman, J. R. Osborne, P. D. Mozley, J. D. Victor, N. D. Schiff, Presynaptic dopamine deficit in minimally conscious state patients following traumatic brain injury. *Brain* **142**, 1887–1893 (2019).
72. G. J. Kirouac, S. Li, G. Mabrouk, GABAergic projection from the ventral tegmental area and substantia nigra to the periaqueductal gray region and the dorsal raphe nucleus. *J Comp Neurol* **469**, 170–184 (2004).
73. S. Spencer, C. B. Saper, T. Joh, D. J. Reis, M. Goldstein, J. D. Raese, Distribution of catecholamine-containing neurons in the normal human hypothalamus. *Brain research* **328**, 73–80 (1985).
74. B. Weissbourd, J. Ren, K. E. DeLoach, C. J. Guenthner, K. Miyamichi, L. Luo, Presynaptic partners of dorsal raphe serotonergic and GABAergic neurons. *Neuron* **83**, 645–662 (2014).
75. E. C. Azmitia, P. J. Gannon, The primate serotonergic system: a review of human and animal studies and a report on *Macaca fascicularis*. *Adv Neurol* **43**, 407–468 (1986).
76. B. E. Jones, L. Friedman, Atlas of catecholamine perikarya, varicosities and pathways in the brainstem of the cat. *J Comp Neurol* **215**, 382–396 (1983).
77. K. Singh, M. G. Garcia-Gomar, S. Cauzzo, J. P. Staab, I. Indovina, M. Bianciardi, Structural connectivity of autonomic, pain, limbic, and sensory brainstem nuclei in living humans based on 7 Tesla and 3 Tesla MRI. *Hum Brain Mapp*, (2022).
78. V. A. Coenen, J. Panksepp, T. A. Hurwitz, H. Urbach, B. Madler, Human medial forebrain bundle (MFB) and anterior thalamic radiation (ATR): imaging of two major subcortical pathways and the dynamic balance of opposite affects in understanding depression. *The Journal of neuropsychiatry and clinical neurosciences* **24**, 223–236 (2012).
79. S. H. Jang, H. G. Kwon, Injury of the Ascending Reticular Activating System in Patients With Fatigue and Hypersomnia Following Mild Traumatic Brain Injury: Two Case Reports. *Medicine* **95**, e2628 (2016).

80. P. N. Alves, C. Foulon, V. Karolis, D. Bzdok, D. S. Margulies, E. Volle, M. Thiebaut de Schotten, An improved neuroanatomical model of the default-mode network reconciles previous neuroimaging and neuropathological findings. *Commun Biol* **2**, 370 (2019).
81. S. B. Snider, Y. G. Bodien, M. Bianciardi, E. N. Brown, O. Wu, B. L. Edlow, Disruption of the ascending arousal network in acute traumatic disorders of consciousness. *Neurology* **93**, e1281–e1287 (2019).
82. S. B. Snider, Y. G. Bodien, A. Frau-Pascual, M. Bianciardi, A. S. Foulkes, B. L. Edlow, Ascending arousal network connectivity during recovery from traumatic coma. *Neuroimage Clin* **28**, 102503 (2020).
83. C. C. Shute, P. R. Lewis, Cholinesterase-Containing Systems of the Brain of the Rat. *Nature* **199**, 1160–1164 (1963).
84. W. J. H. Nauta, H. G. J. M. Kuypers, in *Reticular formation of the brain*, H. H. Jasper, L. D. Proctor, R. S. Knighton, W. C. Noshay, R. T. Costello, Eds. (Little, Brown, and Company, Boston, 1958), pp. 3–30.
85. T. R. Stratford, D. Wirtshafter, Ascending dopaminergic projections from the dorsal raphe nucleus in the rat. *Brain research* **511**, 173–176 (1990).
86. R. D. Oades, G. M. Halliday, Ventral tegmental (A10) system: neurobiology. 1. Anatomy and connectivity. *Brain Res* **434**, 117–165 (1987).
87. C. C. Shute, P. R. Lewis, The ascending cholinergic reticular system: neocortical, olfactory and subcortical projections. *Brain* **90**, 497–520 (1967).
88. L. C. Conrad, C. M. Leonard, D. W. Pfaff, Connections of the median and dorsal raphe nuclei in the rat: an autoradiographic and degeneration study. *J Comp Neurol* **156**, 179–205 (1974).
89. B. E. Jones, T. Z. Yang, The efferent projections from the reticular formation and the locus coeruleus studied by anterograde and retrograde axonal transport in the rat. *J Comp Neurol* **242**, 56–92 (1985).
90. H. G. Lidov, R. Grzanna, M. E. Molliver, The serotonin innervation of the cerebral cortex in the rat—an immunohistochemical analysis. *Neuroscience* **5**, 207–227 (1980).
91. V. A. Coenen, C. R. Honey, T. Hurwitz, A. A. Rahman, J. McMaster, U. Burgel, B. Madler, Medial forebrain bundle stimulation as a pathophysiological mechanism for hypomania in subthalamic nucleus deep brain stimulation for Parkinsons disease. *Neurosurgery* **64**, 1106–1114; discussion 1114–1105 (2009).

92. T. E. Schlaepfer, B. H. Bewernick, S. Kayser, B. Madler, V. A. Coenen, Rapid effects of deep brain stimulation for treatment-resistant major depression. *Biological psychiatry* **73**, 1204–1212 (2013).
93. V. A. Coenen, B. H. Bewernick, S. Kayser, H. Kilian, J. Bostrom, S. Greschus, R. Hurlmann, M. E. Klein, S. Spanier, B. Sajonz, H. Urbach, T. E. Schlaepfer, Superolateral medial forebrain bundle deep brain stimulation in major depression: a gateway trial. *Neuropsychopharmacology : official publication of the American College of Neuropsychopharmacology* **44**, 1224–1232 (2019).
94. S. N. Haber, H. Liu, J. Seidlitz, E. Bullmore, Prefrontal connectomics: from anatomy to human imaging. *Neuropsychopharmacology : official publication of the American College of Neuropsychopharmacology* **47**, 20–40 (2022).
95. F. Bremer, Cerveau isole et physiologie du sommeil. *CR Soc Biol Paris* **118**, (1935).
96. G. Moruzzi, The sleep–waking cycle. *Ergebnisse der Physiologie, biologischen Chemie und experimentellen Pharmakologie* **64**, 1–165 (1972).
97. M. Steriade, E. Constantinescu, V. Apostol, Correlations between alterations of the cortical transaminase activity and EEG patterns of sleep and wakefulness induced by brain–stem transections. *Brain research* **13**, 177–180 (1969).
98. J. Parvizi, A. R. Damasio, Neuroanatomical correlates of brainstem coma. *Brain* **126**, 1524–1536 (2003).
99. B. L. Edlow, R. L. Haynes, E. Takahashi, J. P. Klein, P. Cummings, T. Benner, D. M. Greer, S. M. Greenberg, O. Wu, H. C. Kinney, R. D. Folkerth, Disconnection of the ascending arousal system in traumatic coma. *J Neuropathol Exp Neurol* **72**, 505–523 (2013).
100. W. I. Rosenblum, Immediate, irreversible, posttraumatic coma: a review indicating that bilateral brainstem injury rather than widespread hemispheric damage is essential for its production. *J Neuropathol Exp Neurol* **74**, 198–202 (2015).
101. D. B. Fischer, A. D. Boes, A. Demertzi, H. C. Evrard, S. Laureys, B. L. Edlow, H. Liu, C. B. Saper, A. Pascual–Leone, M. D. Fox, J. C. Geerling, A human brain network derived from coma–causing brainstem lesions. *Neurology*, (2016).
102. M. Bianciardi, S. Izzy, B. R. Rosen, L. L. Wald, B. L. Edlow, Location of Subcortical Microbleeds and Recovery of Consciousness After Severe Traumatic Brain Injury. *Neurology* **97**, e113–e123 (2021).
103. H. A. Baghdoyan, M. L. Rodrigo–Angulo, R. W. McCarley, J. A. Hobson, Site–specific enhancement and suppression of desynchronized sleep signs following cholinergic stimulation of three brainstem regions. *Brain research* **306**, 39–52 (1984).

104. H. B. Wu, M. Stavarache, D. W. Pfaff, L. M. Kow, Arousal of cerebral cortex electroencephalogram consequent to high-frequency stimulation of ventral medullary reticular formation. *Proc Natl Acad Sci USA* **104**, 18292–18296 (2007).
105. B. Ford, C. J. Holmes, L. Mainville, B. E. Jones, GABAergic neurons in the rat pontomesencephalic tegmentum: codistribution with cholinergic and other tegmental neurons projecting to the posterior lateral hypothalamus. *J Comp Neurol* **363**, 177–196 (1995).
106. M. Steriade, D. A. McCormick, T. J. Sejnowski, Thalamocortical oscillations in the sleeping and aroused brain. *Science* **262**, 679–685 (1993).
107. A. Parent, D. Pare, Y. Smith, M. Steriade, Basal forebrain cholinergic and noncholinergic projections to the thalamus and brainstem in cats and monkeys. *J Comp Neurol* **277**, 281–301 (1988).
108. M. E. Bickford, A. E. Gunluk, S. C. Van Horn, S. M. Sherman, GABAergic projection from the basal forebrain to the visual sector of the thalamic reticular nucleus in the cat. *J Comp Neurol* **348**, 481–510 (1994).
109. B. L. Edlow, J. T. Giacino, R. E. Hirschberg, J. Gerrard, O. Wu, L. R. Hochberg, Unexpected recovery of function after severe traumatic brain injury: the limits of early neuroimaging-based outcome prediction. *Neurocrit Care* **19**, 364–375 (2013).
110. S. Izzy, N. L. Mazwi, S. Martinez, C. A. Spencer, J. P. Klein, G. Parikh, M. B. Glenn, S. M. Greenberg, D. M. Greer, O. Wu, B. L. Edlow, Revisiting Grade 3 Diffuse Axonal Injury: Not All Brainstem Microbleeds are Prognostically Equal. *Neurocrit Care* **27**, 199–207 (2017).
111. F. Reinoso-Suarez, I. de Andres, M. Garzon, Functional anatomy of the sleep–wakefulness cycle: wakefulness. *Advances in anatomy, embryology, and cell biology* **208**, 1–128 (2011).
112. G. Buzsaki, R. G. Bickford, D. M. Armstrong, G. Ponomareff, K. S. Chen, R. Ruiz, L. J. Thal, F. H. Gage, Electric activity in the neocortex of freely moving young and aged rats. *Neuroscience* **26**, 735–744 (1988).
113. J. R. Villablanca, Counterpointing the functional role of the forebrain and of the brainstem in the control of the sleep–waking system. *J Sleep Res* **13**, 179–208 (2004).
114. S. Bagnato, C. Boccagni, A. SantAngelo, A. A. Fingelkurts, A. A. Fingelkurts, C. Gagliardo, G. Galardi, Long-lasting coma. *Functional neurology* **29**, 201–205 (2014).
115. B. L. Edlow, L. R. D. Sanz, L. Polizzotto, N. Pouratian, J. D. Rolston, S. B. Snider, A. Thibaut, R. D. Stevens, O. Gosseries, C. Curing Coma, m. its contributing, Therapies

- to Restore Consciousness in Patients with Severe Brain Injuries: A Gap Analysis and Future Directions. *Neurocrit Care* **35**, 68–85 (2021).
116. N. D. Schiff, Recovery of consciousness after severe brain injury: the role of arousal regulation mechanisms and some speculation on the heart–brain interface. *Cleveland Clinic journal of medicine* **77 Suppl 3**, S27–33 (2010).
117. M. Hausser, I. M. Raman, T. Otis, S. L. Smith, A. Nelson, S. du Lac, Y. Loewenstein, S. Mahon, C. Pennartz, I. Cohen, Y. Yarom, The beat goes on: spontaneous firing in mammalian neuronal microcircuits. *J Neurosci* **24**, 9215–9219 (2004).
118. D. D. Potter, S. C. Landis, S. G. Matsumoto, E. J. Furshpan, Synaptic functions in rat sympathetic neurons in microcultures. II. Adrenergic/cholinergic dual status and plasticity. *J Neurosci* **6**, 1080–1098 (1986).
119. G. G. Turrigiano, S. B. Nelson, Homeostatic plasticity in the developing nervous system. *Nat Rev Neurosci* **5**, 97–107 (2004).
120. G. Tononi, O. Sporns, G. M. Edelman, Measures of degeneracy and redundancy in biological networks. *Proc Natl Acad Sci U S A* **96**, 3257–3262 (1999).
121. J. T. Giacino, J. Whyte, E. Bagiella, K. Kalmar, N. Childs, A. Khademi, B. Eifert, D. Long, D. I. Katz, S. Cho, S. A. Yablon, M. Luther, F. M. Hammond, A. Nordenbo, P. Novak, W. Mercer, P. Maurer–Karattup, M. Sherer, Placebo–controlled trial of amantadine for severe traumatic brain injury. *N Engl J Med* **366**, 819–826 (2012).
122. E. A. Fridman, B. Z. Krimchansky, M. Bonetto, T. Galperin, E. R. Gamzu, R. C. Leiguarda, R. Zafonte, Continuous subcutaneous apomorphine for severe disorders of consciousness after traumatic brain injury. *Brain Inj* **24**, 636–641 (2010).
123. J. Whyte, R. Rajan, A. Rosenbaum, D. Katz, K. Kalmar, R. Seel, B. Greenwald, R. Zafonte, D. Demarest, R. Brunner, D. Kaelin, Zolpidem and restoration of consciousness. *Am J Phys Med Rehabil* **93**, 101–113 (2014).
124. M. M. Monti, C. Schnakers, A. S. Korb, A. Bystritsky, P. M. Vespa, Non–Invasive Ultrasonic Thalamic Stimulation in Disorders of Consciousness after Severe Brain Injury: A First–in–Man Report. *Brain Stimul* **9**, 940–941 (2016).
125. A. Thibaut, M. A. Bruno, D. Ledoux, A. Demertzi, S. Laureys, tDCS in patients with disorders of consciousness: sham–controlled randomized double–blind study. *Neurology* **82**, 1112–1118 (2014).
126. C. B. Saper, Staying awake for dinner: hypothalamic integration of sleep, feeding, and circadian rhythms. *Prog Brain Res* **153**, 243–252 (2006).
127. S. Jbabdi, H. Johansen–Berg, Tractography: where do we go from here? *Brain Connect* **1**, 169–183 (2011).

128. D. K. Jones, T. R. Knosche, R. Turner, White matter integrity, fiber count, and other fallacies: the dos and don'ts of diffusion MRI. *NeuroImage* **73**, 239–254 (2013).
129. C. Thomas, F. Q. Ye, M. O. Irfanoglu, P. Modi, K. S. Saleem, D. A. Leopold, C. Pierpaoli, Anatomical accuracy of brain connections derived from diffusion MRI tractography is inherently limited. *Proc Natl Acad Sci U S A* **111**, 16574–16579 (2014).
130. K. H. Maier–Hein, P. F. Neher, J. C. Houde, M. A. Cote, E. Garyfallidis, J. Zhong, M. Chamberland, F. C. Yeh, Y. C. Lin, Q. Ji, W. E. Reddick, J. O. Glass, D. Q. Chen, Y. Feng, C. Gao, Y. Wu, J. Ma, H. Renjie, Q. Li, C. F. Westin, S. Deslauriers–Gauthier, J. O. O. Gonzalez, M. Paquette, S. St–Jean, G. Girard, F. Rheault, J. Sidhu, C. M. W. Tax, F. Guo, H. Y. Mesri, S. David, M. Froeling, A. M. Heemskerk, A. Leemans, A. Bore, B. Pinsard, C. Bedetti, M. Desrosiers, S. Brambati, J. Doyon, A. Sarica, R. Vasta, A. Cerasa, A. Quattrone, J. Yeatman, A. R. Khan, W. Hodges, S. Alexander, D. Romascano, M. Barakovic, A. Auria, O. Esteban, A. Lemkaddem, J. P. Thiran, H. E. Cetingul, B. L. Odry, B. Mailhe, M. S. Nadar, F. Pizzagalli, G. Prasad, J. E. Villalon–Reina, J. Galvis, P. M. Thompson, F. S. Requejo, P. L. Laguna, L. M. Lacerda, R. Barrett, F. DellAcqua, M. Catani, L. Petit, E. Caruyer, A. Daducci, T. B. Dyrby, T. Holland–Letz, C. C. Hilgetag, B. Stieltjes, M. Descoteaux, The challenge of mapping the human connectome based on diffusion tractography. *Nat Commun* **8**, 1349 (2017).
131. G. Grisot, S. N. Haber, A. Yendiki, Diffusion MRI and anatomic tracing in the same brain reveal common failure modes of tractography. *NeuroImage* **239**, 118300 (2021).
132. J. DeFelipe, From the connectome to the synaptome: an epic love story. *Science* **330**, 1198–1201 (2010).
133. K. Chung, K. Deisseroth, CLARITY for mapping the nervous system. *Nat Methods* **10**, 508–513 (2013).
134. H. Wang, J. Zhu, M. Reuter, L. N. Vinke, A. Yendiki, D. A. Boas, B. Fischl, T. Akkin, Cross–validation of serial optical coherence scanning and diffusion tensor imaging: a study on neural fiber maps in human medulla oblongata. *Neuroimage* **100**, 395–404 (2014).
135. M. Steriade, Corticothalamic resonance, states of vigilance and mentation. *Neuroscience* **101**, 243–276 (2000).
136. G. Aston–Jones, J. D. Cohen, Adaptive gain and the role of the locus coeruleus–norepinephrine system in optimal performance. *J Comp Neurol* **493**, 99–110 (2005).

137. M. Boly, M. I. Garrido, O. Gosseries, M. A. Bruno, P. Boveroux, C. Schnakers, M. Massimini, V. Litvak, S. Laureys, K. Friston, Preserved feedforward but impaired top-down processes in the vegetative state. *Science* **332**, 858–862 (2011).
138. J. G. Veening, L. W. Swanson, W. M. Cowan, R. Nieuwenhuys, L. M. Geeraedts, The medial forebrain bundle of the rat. II. An autoradiographic study of the topography of the major descending and ascending components. *J Comp Neurol* **206**, 82–108 (1982).
139. R. Grzanna, M. E. Molliver, in *The reticular formation revisited: specifying function for a nonspecific system*, B. M. Hobson JA, Ed. (Raven Press, New York, 1980), pp. 83–97.
140. P. Zhao, T. Jiang, H. Wang, X. Jia, A. Li, H. Gong, X. Li, Upper brainstem cholinergic neurons project to ascending and descending circuits. *BMC Biol* **21**, 135 (2023).
141. R. W. McCarley, J. A. Hobson, Single neuron activity in cat gigantocellular tegmental field: selectivity of discharge in desynchronized sleep. *Science* **174**, 1250–1252 (1971).
142. A. Nunez, I. de Andres, E. Garcia–Austt, Relationships of nucleus reticularis pontis oralis neuronal discharge with sensory and carbachol evoked hippocampal theta rhythm. *Experimental brain research. Experimentelle Hirnforschung. Experimentation cerebrale* **87**, 303–308 (1991).
143. R. P. Vertes, Selective firing of rat pontine gigantocellular neurons during movement and REM sleep. *Brain research* **128**, 146–152 (1977).
144. D. Kroeger, L. L. Ferrari, G. Petit, C. E. Mahoney, P. M. Fuller, E. Arrigoni, T. E. Scammell, Cholinergic, Glutamatergic, and GABAergic Neurons of the Pedunculopontine Tegmental Nucleus Have Distinct Effects on Sleep/Wake Behavior in Mice. *J Neurosci* **37**, 1352–1366 (2017).
145. J. R. Andrews–Hanna, J. S. Reidler, J. Sepulcre, R. Poulin, R. L. Buckner, Functional–anatomic fractionation of the brains default network. *Neuron* **65**, 550–562 (2010).
146. R. M. Braga, R. L. Buckner, Parallel Interdigitated Distributed Networks within the Individual Estimated by Intrinsic Functional Connectivity. *Neuron* **95**, 457–471 e455 (2017).
147. J. Vytlačil, A. Kayser, A. Miyakawa, M. DeSposito, An approach for identifying brainstem dopaminergic pathways using resting state functional MRI. *PLoS One* **9**, e87109 (2014).
148. F. Beissner, A. Schumann, F. Brunn, D. Eisentrager, K. J. Bar, Advances in functional magnetic resonance imaging of the human brainstem. *NeuroImage* **86**, 91–98 (2014).



149. M. Bianciardi, N. Toschi, C. Eichner, J. R. Polimeni, K. Setsompop, E. N. Brown, M. S. Hamalainen, B. R. Rosen, L. L. Wald, In vivo functional connectome of human brainstem nuclei of the ascending arousal, autonomic, and motor systems by high spatial resolution 7-Tesla fMRI. *MAGMA* **29**, 451–462 (2016).
150. S. Zhang, S. Hu, H. H. Chao, C. S. Li, Resting-State Functional Connectivity of the Locus Coeruleus in Humans: In Comparison with the Ventral Tegmental Area/Substantia Nigra Pars Compacta and the Effects of Age. *Cereb Cortex* **26**, 3413–3427 (2016).
151. J. A. McNab, B. L. Edlow, T. Witzel, S. Y. Huang, H. Bhat, K. Heberlein, T. Feiweier, K. Liu, B. Keil, J. Cohen-Adad, M. D. Tisdall, R. D. Folkerth, H. C. Kinney, L. L. Wald, The Human Connectome Project and beyond: Initial applications of 300mT/m gradients. *NeuroImage* **80**, 234–245 (2013).
152. R. Sclocco, F. Beissner, M. Bianciardi, J. R. Polimeni, V. Napadow, Challenges and opportunities for brainstem neuroimaging with ultrahigh field MRI. *Neuroimage*, (2017).
153. M. Steriade, To burst, or rather, not to burst. *Nat Neurosci* **4**, 671 (2001).
154. S. M. Sagar, F. R. Sharp, T. Curran, Expression of c-fos protein in brain: metabolic mapping at the cellular level. *Science* **240**, 1328–1331 (1988).
155. M. Steriade, R. W. McCarley, *Brain Control of Wakefulness and Sleep*. (Kluwer Academic, New York, NY, ed. 2, 2005).
156. E. G. Jones, *The Thalamus*. (Cambridge University Press, New York, NY, ed. 2, 2007).
157. M. Steriade, D. Biesold, *Brain Cholinergic Systems*. (Oxford University Press, New York, NY, 1990).
158. E. Garcia-Rill, *Waking and the Reticular Activating System in Health and Disease*. (Academic Press, London, 2015).
159. J. Parvizi, A. Damasio, Consciousness and the brainstem. *Cognition* **79**, 135–160 (2001).
160. B. E. Jones, Arousal systems. *Frontiers in bioscience : a journal and virtual library* **8**, s438–451 (2003).
161. C. B. Saper, P. M. Fuller, N. P. Pedersen, J. Lu, T. E. Scammell, Sleep state switching. *Neuron* **68**, 1023–1042 (2010).
162. C. B. Saper, P. M. Fuller, Wake-sleep circuitry: an overview. *Current opinion in neurobiology* **44**, 186–192 (2017).
163. E. Roberts, GABA-related phenomena, models of nervous system function, and seizures. *Ann Neurol* **16 Suppl**, S77–89 (1984).

164. G. Buzsaki, Feed–forward inhibition in the hippocampal formation. *Prog Neurobiol* **22**, 131–153 (1984).
165. N. D. Schiff, Recovery of consciousness after brain injury: a mesocircuit hypothesis. *Trends Neurosci* **33**, 1–9 (2010).
166. E. M. Shapiro, S. Skrtic, K. Sharer, J. M. Hill, C. E. Dunbar, A. P. Koretsky, MRI detection of single particles for cellular imaging. *Proc Natl Acad Sci U S A* **101**, 10901–10906 (2004).
167. J. A. McNab, K. L. Miller, Sensitivity of diffusion weighted steady state free precession to anisotropic diffusion. *Magn Reson Med* **60**, 405–413 (2008).
168. K. L. Miller, J. A. McNab, S. Jbabdi, G. Douaud, Diffusion tractography of post–mortem human brains: optimization and comparison of spin echo and steady–state free precession techniques. *NeuroImage* **59**, 2284–2297 (2012).
169. B. L. Edlow, C. D. Keene, D. Perl, D. Iacono, R. Folkerth, W. Stewart, C. L. MacDonald, J. Augustinack, R. Diaz–Arrastia, C. Estrada, E. Flannery, W. Gordon, T. Grabowski, K. Hansen, J. Hoffman, C. Kroenke, E. Larson, P. Lee, A. Mareyam, J. A. McNab, J. McPhee, A. L. Moreau, A. Renz, K. Richmire, A. Stevens, C. Y. Tang, L. S. Tirrell, E. Trittschuh, A. van der Kouwe, A. Varjabedian, L. L. Wald, O. Wu, A. Yendiki, L. Young, L. Zollei, B. Fischl, P. K. Crane, K. Dams–OConnor, Multimodal Characterization of the Late Effects of TBI (LETBI): A Methodological Overview of the LETBI Project. *J Neurotrauma*, (2018).
170. B. T. Yeo, F. M. Krienen, J. Sepulcre, M. R. Sabuncu, D. Lashkari, M. Hollinshead, J. L. Roffman, J. W. Smoller, L. Zollei, J. R. Polimeni, B. Fischl, H. Liu, R. L. Buckner, The organization of the human cerebral cortex estimated by intrinsic functional connectivity. *J Neurophysiol* **106**, 1125–1165 (2011).
171. A. Schaefer, R. Kong, E. M. Gordon, T. O. Laumann, X. N. Zuo, A. J. Holmes, S. B. Eickhoff, B. T. T. Yeo, Local–Global Parcellation of the Human Cerebral Cortex from Intrinsic Functional Connectivity MRI. *Cereb Cortex* **28**, 3095–3114 (2018).
172. S. C. Deoni, T. M. Peters, B. K. Rutt, High–resolution T1 and T2 mapping of the brain in a clinically acceptable time with DESPOT1 and DESPOT2. *Magn Reson Med* **53**, 237–241 (2005).
173. B. Fischl, D. H. Salat, A. J. van der Kouwe, N. Makris, F. Segonne, B. T. Quinn, A. M. Dale, Sequence–independent segmentation of magnetic resonance images. *NeuroImage* **23 Suppl 1**, S69–84 (2004).
174. D. Sederevicius, D. Vidal–Pineiro, O. Sorensen, K. van Leemput, J. E. Iglesias, A. V. Dalca, D. N. Greve, B. Fischl, A. Bjornerud, K. B. Walhovd, A. M. Fjell, I. Alzheimers Disease Neuroimaging, Reliability and sensitivity of two whole–brain segmentation

- approaches included in FreeSurfer – ASEG and SAMSEG. *NeuroImage* **237**, 118113 (2021).
175. D. N. Greve, B. Fischl, Accurate and robust brain image alignment using boundary–based registration. *NeuroImage* **48**, 63–72 (2009).
176. B. Fischl, M. I. Sereno, R. B. Tootell, A. M. Dale, High–resolution intersubject averaging and a coordinate system for the cortical surface. *Hum Brain Mapp* **8**, 272–284 (1999).
177. T. E. Behrens, M. W. Woolrich, M. Jenkinson, H. Johansen–Berg, R. G. Nunes, S. Clare, P. M. Matthews, J. M. Brady, S. M. Smith, Characterization and propagation of uncertainty in diffusion–weighted MR imaging. *Magn Reson Med* **50**, 1077–1088 (2003).
178. V. F. Newcombe, G. B. Williams, D. Scoffings, J. Cross, T. A. Carpenter, J. D. Pickard, D. K. Menon, Aetiological differences in neuroanatomy of the vegetative state: insights from diffusion tensor imaging and functional implications. *J Neurol Neurosurg Psychiatry* **81**, 552–561 (2010).
179. M. R. Wiegell, D. S. Tuch, H. B. Larsson, V. J. Wedeen, Automatic segmentation of thalamic nuclei from diffusion tensor magnetic resonance imaging. *Neuroimage* **19**, 391–401 (2003).
180. R. Wang, V. J. Wedeen, V. T. Diffusion Toolkt, Version 0.5.2, Athinoula A. Martinos Center for Biomedical Imaging Massachusetts General Hospital, Boston, MA, <http://www.trackvis.org>. (2010).
181. C. P. Hess, P. Mukherjee, E. T. Han, D. Xu, D. B. Vigneron, Q–ball reconstruction of multimodal fiber orientations using the spherical harmonic basis. *Magn Reson Med* **56**, 104–117 (2006).
182. S. Mori, B. J. Crain, V. P. Chacko, P. C. van Zijl, Three–dimensional tracking of axonal projections in the brain by magnetic resonance imaging. *Ann Neurol* **45**, 265–269 (1999).
183. D. S. Tuch, T. G. Reese, M. R. Wiegell, N. Makris, J. W. Belliveau, V. J. Wedeen, High angular resolution diffusion imaging reveals intravoxel white matter fiber heterogeneity. *Magn Reson Med* **48**, 577–582 (2002).
184. J. D. Tournier, F. Calamante, D. G. Gadian, A. Connelly, Direct estimation of the fiber orientation density function from diffusion–weighted MRI data using spherical deconvolution. *NeuroImage* **23**, 1176–1185 (2004).
185. T. E. Behrens, H. J. Berg, S. Jbabdi, M. F. Rushworth, M. W. Woolrich, Probabilistic diffusion tractography with multiple fibre orientations: What can we gain? *NeuroImage* **34**, 144–155 (2007).

186. H. Azadbakht, L. M. Parkes, H. A. Haroon, M. Augath, N. K. Logothetis, A. de Crespigny, H. E. D'Arceuil, G. J. Parker, Validation of High-Resolution Tractography Against In Vivo Tracing in the Macaque Visual Cortex. *Cereb Cortex* **25**, 4299–4309 (2015).
187. J. D. Schmahmann, D. N. Pandya, The cerebrocerebellar system. *Int Rev Neurobiol* **41**, 31–60 (1997).
188. M. F. Glasser, S. N. Sotiropoulos, J. A. Wilson, T. S. Coalson, B. Fischl, J. L. Andersson, J. Xu, S. Jbabdi, M. Webster, J. R. Polimeni, D. C. Van Essen, M. Jenkinson, W. U.-M. H. Consortium, The minimal preprocessing pipelines for the Human Connectome Project. *NeuroImage* **80**, 105–124 (2013).
189. J. Li, R. M. Leahy, Parameter selection for optimized non-local means filtering of task fMRI. *IEEE International Symposium on Biomedical Imaging April 2017*, DOI: 10.1109/ISBI.2017.7950564 (2017).
190. J. Li, S. Choi, A. A. Joshi, J. L. Wisnowski, R. M. Leahy, Temporal non-local means filtering for studies of intrinsic brain connectivity from individual resting fMRI. *Med Image Anal* **61**, 101635 (2020).
191. J. Li, W. H. Curley, B. Guerin, D. D. Dougherty, A. V. Dalca, B. Fischl, A. Horn, B. L. Edlow, Mapping the subcortical connectivity of the human default mode network. *NeuroImage*, 118758 (2021).
192. A. A. Joshi, M. Chong, J. Li, S. Choi, R. M. Leahy, Are you thinking what I'm thinking? Synchronization of resting fMRI time-series across subjects. *NeuroImage* **172**, 740–752 (2018).
193. H. Akrami, A. A. Joshi, J. Li, R. M. Leahy, Group-wise alignment of resting fMRI in space and time. *Proc. SPIE 10949, Medical Imaging 2019: Image Processing*, <https://doi.org/10.1117/1112.2512564> (2019).
194. J. Li, J. L. Wisnowski, A. A. Joshi, R. M. Leahy, Robust brain network identification from multi-subject asynchronous fMRI data. *NeuroImage* **227**, 117615 (2021).
195. J. Li, Y. Liu, J. L. Wisnowski, R. M. Leahy, Identification of overlapping and interacting networks reveals intrinsic spatiotemporal organization of the human brain. *NeuroImage* **270**, 119944 (2023).
196. M. M. Mesulam, C. Geula, M. A. Bothwell, L. B. Hersh, Human reticular formation: cholinergic neurons of the pedunculopontine and laterodorsal tegmental nuclei and some cytochemical comparisons to forebrain cholinergic neurons. *J Comp Neurol* **283**, 611–633 (1989).

197. J. Pearson, L. Brandeis, M. Goldstein, A. C. Cuello, Neurotransmitter related immunocytochemistry of the human central nervous system. *Journal of neural transmission. Supplementum* **18**, 25–31 (1983).
198. J. Pearson, M. Goldstein, K. Markey, L. Brandeis, Human brainstem catecholamine neuronal anatomy as indicated by immunocytochemistry with antibodies to tyrosine hydroxylase. *Neuroscience* **8**, 3–32 (1983).
199. D. M. Morris, K. V. Embleton, G. J. Parker, Probabilistic fibre tracking: differentiation of connections from chance events. *Neuroimage* **42**, 1329–1339 (2008).

**Acknowledgements:** We dedicate this work in memoriam to Marty Samuels, MD, the Miriam Sydney Joseph Distinguished Professor of Neurology at Harvard Medical School and Founding Chair of the Department of Neurology at Brigham and Women’s Hospital. Dr. Samuels mentored generations of neurologists, neuroimagers, and neuropathologists, of which we were fortunate to be a part. Dr. Samuels was an avid and insightful student and teacher of neuroanatomy and neuropathology of human consciousness, from whom we learned much. He was an early supporter of the histologic-radiology correlation studies performed here, for which we are grateful.

We are grateful to the families for the brain donation of their loved ones, and to the individuals who donated their own brains for this study to advance medical science. We also thank Bruce Rosen, Merit Cudkowicz, and Jonathan Rosand for their support of this work. We thank Michelle Siciliano for assistance with processing of human brain specimens and Kathryn Regan at Horus Scientific for assistance with immunostaining. We thank Kimberly Main Knoper for artwork used in the connectograms.

**Funding:** This work was supported by the National Institutes of Health (NIH) Director’s Office (DP2HD101400), NIH National Institute for Neurological Disorders and Stroke (R21NS109627, K23NS094538, U01NS086625, R01NS0525851, R21NS072652, R01NS070963, R01NS083534, UH3NS095554, U24NS10059103, R01NS105820), NIH National Institute for Biomedical Imaging and Bioengineering (P41EB030006, R01EB023281, R01EB006758, R21EB018907, R01EB019956), NIH National Institute of Child Health and Human

Development R01HD102616, R21HD095338), NIH National Institute on Deafness and Other Communication Disorders (R21DC015888), NIH National Institute on Aging (R21AG082082, R01AG064027, R01AG008122, R01AG016495, R01AG070988), NIH National Institute on Mental Health (UM1MH130981, R01MH123195, R01MH121885, RF1MH123195), BRAIN Initiative Cell Census Network (U01MH117023 and UM1MH130981), James S. McDonnell Foundation, American Academy of Neurology/American Brain Foundation, Center for Integration of Medicine and Innovative Technology (Boston, MA), Rappaport Foundation, Tiny Blue Dot Foundation, American SIDS Institute, and Chen Institute MGH Research Scholar Award. Additional support was provided by the NIH Blueprint for Neuroscience Research (U01MH093765), part of the multi-institutional Human Connectome Project. This research was also made possible by the resources provided by National Institutes of Health P41RR014075 and shared instrumentation grants S10RR023401, S10RR019307, and S10RR023043. Much of the computation resources required for this research was performed on computational hardware generously provided by the Massachusetts Life Sciences Center (<https://www.masslifesciences.com/>).

**Author contributions:** B.L.E., R.D.F., B.F., and H.C.K. conceived, designed, and coordinated the study and acquired funding. A.v.d.K. and B.F. developed the ex vivo diffusion MRI protocol for data acquisition. M.O., H.J.F., S.B.S., J.E.I., L.Z., Y.G.B., J.A., D.N.G., B.R.D., C.M., A.S., developed the ex vivo diffusion MRI processing and analysis methods. J.A., R.L.H., R.D.F., and H.C.K. developed the histology and immunostaining protocols. B.L.E., M.O., J.A., R.L.H., R.D.F., and H.C.K., interpreting the histology and immunostaining data. B.L.E. and M.O. manually traced the nodal regions of interest on the ex vivo diffusion MRI datasets, with

anatomic confirmation performed by H.C.K. The statistical plan was developed by E.N.B. J.L. developed the methods for the *in vivo* functional MRI (fMRI) connectivity analysis and processed and analyzed the fMRI data. Connectivity data were interpreted by B.L.E., M.O., H.J.F., J.L., C.M., S.B.S., J.E.I., L.Z., J.A., Y.G.B., R.L.H., D.N.G., J.T.G., C.D., E.N.B., R.D.F., B.F., H.C.K. B.L.E. and H.C.K. drafted the manuscript. All authors provided critical commentary and revisions and reviewed the final manuscript.

**Competing interests:** BF has a financial interest in CorticoMetrics, a company whose medical pursuits focus on brain imaging and measurement technologies. BF's interests were reviewed and are managed by Massachusetts General Hospital and Mass General Brigham HealthCare in accordance with their conflict-of-interest policies.

**Data and materials availability:**

All *ex vivo* diffusion MRI data, along with the node regions of interest used for the connectivity analyses, are available at (<https://openneuro.org/datasets/ds004640/versions/1.0.1>). All histology and immunostain data are available at (<https://histopath.nmr.mgh.harvard.edu>). Version 2.0 of the Harvard Ascending Arousal Network Atlas is available at Dryad Data Repository (doi:10.5061/dryad.zw3r228d2; download link:

<https://datadryad.org/stash/share/aJ713eXY12ND56bzOBejVG2jmOFCD2CKxdSJsYWEHkw>).

The minimally preprocessed *in vivo* fMRI data are available at <https://db.humanconnectome.org>, and our processed fMRI data are available at

<https://openneuro.org/datasets/ds003716/versions/1.0.0>. All code used to process the *ex vivo*

MRI data are available at [https://github.com/ComaRecoveryLab/Network-based\\_Autopsy](https://github.com/ComaRecoveryLab/Network-based_Autopsy), and



all code used to process the *in vivo* fMRI data are available at

[https://github.com/ComaRecoveryLab/Subcortical\\_DMN\\_Functional\\_Connectivity](https://github.com/ComaRecoveryLab/Subcortical_DMN_Functional_Connectivity).